OBSERVED INTERACTIONS OF THERMAL ENERGY HELIUM AND ARGON ATOMS WITH VAPOR-DEPOSITED SINGLE-CRYSTAL SILVER SURFACES

G.A. Pjura, Jr.
S.S. Fisher

OBSERVED INTERACTIONS OF THERMAL-ENERGY HELIUM AND ARGON ATOMS WITH VAPOR-DEPOSITED, SINGLE-CRYSTAL SILVER SURFACES

by

G.A. Pjura, Jr.

and

S.S. Fisher

Technical Report

under

NASA Grant NGR 47-005-046

Department of Aerospace Engineering and Engineering Physics

RESEARCH LABORATORIES FOR THE ENGINEERING SCIENCES

SCHOOL OF ENGINEERING AND APPLIED SCIENCE

UNIVERSITY OF VIRGINIA

Charlottesville, Virginia

Report No. AEEP-4038-112-69U

September, 1969

FOREWARD

This report is the thesis of Mr. Pjura submitted in partial satisfaction of the requirements for the degree, Master of Engineering Physics, at the University of Virginia. The investigation described herein was carried out under the sponsorship of the National Aeronautics and Space Administration, through Grant NGR 47-005-046, and under the direction of the undersigned, a principal investigator with that grant. Other principal investigators with this grant are Professors A.R. Kuhlthau and J.E. Scott, Jr. Funds made available through the University of Virginia's NASA Institutional Grant NsG-682 were used for construction of much of the basic laboratory apparatus.

Sam S. Fisher
Assistant Professor
Aerospace Engineering

ABSTRACT

Thermal energy, nozzle-type atomic beams of helium and of argon are scattered from a vapor-deposited, single-crystal silver target whose (111) crystal plane is oriented parallel to the scattering surface. The intensity, mean speed, and spread in speeds about the mean of the scattered atoms are measured by means of a time-of-flight detection system. These measurements are conducted in the principal scattering plane (plane of incidence) as well as in selected planes transverse to the principal plane. The effects of variations of the angle of incidence, target temperature, and surface smoothness on the scattering process are explored. Finally, results are compared with those of other investigators in order to evaluate the extent to which nominally identical target surfaces can be reproduced from laboratory to laboratory.

ACKNOWLEDGMENTS

The author wishes to express his gratitude to Professor S. S. Fisher for giving freely of his time, advice, and assistance whenever needed; to Dr. M. N. Bishara for patiently conveying to the author whatever knowledge of laboratory techniques he presently possesses; to Messrs. J. R. Bledsoe and E. W. McClurken for their enlightening criticism and generous assistance in the preparation of the final draft of this thesis; to Mr. F. E. Wawner for performing the diffraction and microscopic analysis of the silver film subsequent to its removal from vacuum and for providing instructive commentary thereupon; and to Mr. W. F. Bailey for rendering valuable assistance at various times during the course of this work. In addition, the author is indebted to NASA and the University of Virginia's Research Laboratories for the Engineering Sciences for their financial support. Finally, a special note of appreciation is due all those members of the Department of Aerospace Engineering and Engineering Physics not directly involved in this project who have generously made their knowledge available to the author at various times during his studies here.

TABLE OF CONTENTS

LIST OF FIGURES

LIST OF TABLES

LIST OF SYMBOLS

c	thermal speed, $v - \langle v \rangle$
$\hat{f}$	fiducial direction unit vector, Fig. (3.3.2)
$g(v)$	differential intensity distribution, Eq. (A1.1)
$\hat{i}$	incident beam unit vector, Fig. (3.3.2)
I	intensity (atoms/steradian-second)
k	Boltzmann gas constant
K	calibration constant, Eq. (A1.5)
K_1	parameter, Eq. (A1.16)
L	length of flightpath
M_g	mass of gas atom
n_{od}	density at the detector of an unchopped beam, Eq. (A1.18)
$\hat{r}$	detector unit vector, Fig. (3.3.2)
R	TOF resolution, $\Delta t/t_{so}$, p. 34
S'	free constant, Eq. (A1.10)
S	thermal spread, Eq. (5.1.1.7)
$S_d(t)$	TOF detector signal, Section 3.2, Eq. (A1.9)
$S_d^o(t)$	TOF detector signal (ideal), Eq. (A1.5)
$S_d(t_m)$	maximum TOF detector signal, Fig. (3.4.1)
SF	shape factor, Eq. (5.1.3.1)
SNR	signal to noise ratio
t	time
t_1, t_m, t_2	specific times of flight, Fig. (3.4.1)

t_o	free constant, Eq. (A1.11)
t_{so}	halfwidth of shutter function, Eq. (A1.5)
T	temperature
TOF	time of flight
U_m	measured signal height at the detector
U_o	ideal signal height at the detector
v	speed
X_{a1}	distance between the target and the first aperture, Fig. (3.1.3)
X_{a2}	distance between the target and the entrance aperture, Fig. (3.1.3)
X_c	distance between the target and the chopper, Fig. (3.1.3)
X_d	distance between the target and the detector plane, Fig. (3.1.3)
α	azimuth rotation angle of target, Fig. (3.3.1)
δ	angle from incident beam to detector
Θ	vertical rotation angle of target, Fig. (3.3.1)
Θ_i	atomic beam incidence angle, Fig. (3.3.2)
Θ_r	in-plane scattering angle, Fig. (3.3.2)
τ	tilt rotation angle of target, Fig. (3.3.1)
ϕ_r	transverse plane scattering angle, Fig. (3.3.2)
ΔS	speed spread, Eq. (5.1.1.7)
Δt	halfwidth of detector signal
$\Delta \Theta_r$	angular halfwidth of scattered lobe, Section 5.1.3

Subscripts

g	gas
i	incident
m	maximum
n	normal
o	nozzle stagnation condition
r	reflected
s	surface or denotes full thermal accommodation to the surface; see Eq. (5.1.1.2-4)

Brackets

$\langle\ \rangle$	mean value
[ ]	normalized to diffuse-scattering, fully accommodated value; see Eq. (5.1.1.5-7)
( )	crystallographic plane normal to enclosed direction
[[ ]]	set of equivalent crystallographic directions

CHAPTER 1

INTRODUCTION

Over the course of the past several years, the increasing availability of improved vacuum systems, the development of nearly monoenergetic molecular beams, and the advent of a host of electronic signal processing aids have spurred a resurgence of experimental investigations into the basic nature of gas-surface interactions. Refinements in the experimentalist's ability to control the incident gas beam (in terms of energy, angular divergence and spread in speeds) and to monitor the scattered flux (in terms of the same parameters) have, in general, surpassed his ability to describe with certainty the in-situ (under-vacuum) condition of the scattering surface.

A variety of techniques are available to deal with the uncertainties associated with adequately describing the crystallographic condition, roughness, and extent of contamination of the scattering surface. Use of crystals that are carefully grown, then cut and polished, or cleaved, along a desired orientation can assure that the crystal structure of the solid near the surface is known and that the surface topography is within some appropriate measure of being microscopically flat. In addition, glove-box

or in-situ preparation of surfaces can be employed to control the degree of surface contamination. These methods are complicated, however, and require considerable special equipment. Moreover, for many solids, sophisticated surface preparation techniques are virtually impossible to apply within a glove-box or within a vacuum chamber of the type generally available. Even if such care could be taken, the ultimate vacuum attainable in the present apparatus is such that adsorption of the background gases in the test chamber could contaminate the surface in a period of several minutes, thus masking the details of whatever surface structure may have been obtained initially.

In an effort to improve upon this state-of-the-art in the study of scattering from single crystal surfaces of rare metals, Saltsburg and Smith [1], [2], [3] pioneered the technique of epitaxially growing single-crystal thin films in vacuum by means of vapor deposition on heated, monocrystalline substrates. This technique has since been successfully employed by other researchers [4], [5] in the study of gas scattering from metallic surfaces. Its acceptance and popularity, in fact, motivated the present attempt to adapt this technique to the facilities available in the University of Virginia's Gas-Surface Laboratory. The readily available data obtained in previous studies would then provide at least partial

checks for the experiments to be carried out.

To provide the reader with suitable sources for acquiring a familiarity with the full range of research in the field of gas-surface interactions and with the techniques commonly employed, reference is made to the reviews of Smith and Saltsburg [6], Hurlbut [7], and Stickney [8]. From among the various types of beam generators, flux monitoring systems and target surfaces considered therein, the following combination is selected here. First, an aerodynamic atomic beam source is employed. Aerodynamic beams [9], operating in the low thermal energy range, offer the advantageous combination of narrow beam energy distribution and high beam fluxes ($\sim 10^{18}$-10^{19} particles/ster.-sec.). Second, time-of-flight methods are used to monitor the speed distributions of the scattered atoms. The time-of-flight method [10], [11] is versatile enough to be readily applied to various gases over a range of energies and is particularly well suited for adaptation to the specialized electronic processing techniques necessary to improve the marginal signal-to-noise ratios encountered in the detection of these scattered beams. Finally, the (111) surface of a monocrystalline silver target grown by vacuum vapor-deposition on a muscovite mica substrate is employed. The (111) silver surface is chosen because of its established stability in vacuum [3] and because of the

availability of a wider range of comparative data for this surface than for other possible candidates.

The experimental results recorded here are the product of a sequence of studies performed on one target surface, only, over a period of some 300 hours following deposition, during which the target was maintained continually under vacuum. Guided by the well-documented results of Saltsburg and Smith [3] with similar silver surfaces, the present experiments were devised initially to investigate the possible presence of diffraction in the scattering of noble gases from silver crystals. Secondly, they would provide velocity distribution data for the scattered beams. It was reasoned that the use of nearly monoenergetic incident beams and the ability to monitor the speed distributions of the scattered atoms would significantly enhance the probability of observing diffraction, if it occurred. For the present, no effects attributable to diffraction can be reported as a result of this effort. Their absence from the data, of course, in no way excludes the possibility of the presence of diffraction in the interaction. The results of the study are, nevertheless, of interest. The velocity data are a useful supplement to the knowledge available concerning the Ar - Ag (111) interaction pair. In addition, the results confirm, in most respects, those data previously published concerning this pair, with slight inconsistencies

likely attributable to small differences in the experimental approaches.

The remaining chapters organize the discussion of the experiments performed according to the following scheme. The process involved in growing a single crystal target surface as well as the design and construction of the deposition apparatus comprise the substance of Chapter 2. Chapter 3 concerns itself with describing the various subsystems involved in performing the actual scattering experiments and evaluating their results. It also presents the coordinate system in which the scattering data are plotted. A brief outline of the complete experimental sequence is contained in Chapter 4 followed by the actual presentation and discussion of the data obtained in Chapter 5. Finally, Chapter 6 offers selected comparisons with the data of other experimenters, a summary of the results, and some concluding remarks.

CHAPTER 2

THE TARGET SURFACE

2.1 Surface Requirements

The growing popularity of epitaxially-grown target surfaces and their selection for use in the present experiments results from their ability to satisfy a number of specific requirements common to many gas-surface investigations. For example, the experimenter can select from a variety of surface materials and crystallographic orientations for study in the same apparatus by simply selecting the appropriate substrate. By careful inspection of the chosen substrate to insure a minimum of steps and lattice imperfections, he can grow crystallographically well-defined films whose surfaces contain significantly fewer defects than are generally found on the surfaces of solid crystals prepared by mechanical techniques. Further, surface contamination in principle can be selectively controlled by varying the metal deposition rate relative to the rate of adsorption of background constituents from the test chamber. Even the surface topography can be selectively altered by varying the substrate temperature during deposition.

A final, and very real, consideration in favor of this technique is its economy; epitaxial metal films can be grown for a small fraction of the cost (in both time and equipment) required to grow a monocrystalline solid and suitably prepare its surface.

2.2 Epitaxy

The term "epitaxy" (or "epitaxial growth") is most often used to describe the oriented crystallization of a substance on a foreign substrate. The application of this process considered here concerns the growth of such crystals in vacuum by means of vapor deposition. Crystals obtained in this manner have been studied extensively by crystallographers [12], [13], [14], [15] and are consequently well documented with regard both to their degree of perfection and to the techniques available for controlling their growth.

The process of epitaxial growth by vapor deposition in a vacuum is dependent upon four main factors:

1) nature of the substrate,

2) temperature of the substrate,

3) deposition rate, and

4) residual gas pressure during deposition.

The discussion by Brenner [16] conveniently points out

the implications of each of these and is outlined below.

Suitable substrates must be monocrystalline and have a minimum of defects. Cleavage faces of sodium chloride and of mica are among those most often used. These faces inevitably contain cleavage steps, so care must be taken to obtain substrates on which such steps are relatively few in number and at most only a few monolayers in height; this insures that these steps will not be widely reproduced in the epitaxially grown film. In addition, in order to minimize parallel misfit, the substrate surface must have lattice parameters compatible with those of the required orientation of the film. For the present experiment, the (001) cleavage plane of muscovite mica provides a satisfactory and widely used substrate for the growth of (111) silver.

The substrate temperature affects a) the critical size and formation rate of crystal nuclei in the deposited film, b) the mobility of the adsorbed atoms, and c) the annealing of defects in the condensed film. Temperatures that are too low inhibit the surface mobility of adsorbates and discourage the lateral growth rate of nuclei. This generates a large number of small nuclei that tend to be randomly oriented and, consequently, films grown at too low a temperature tend to be polycrystalline. Raising the temperature increases surface mobility, resulting in the growth of fewer, larger nuclei and an attendant decrease

in the density of closure defects. Excessive substrate temperatures, on the other hand, result in three-dimensional crystal growth and a highly irregular (even though monocrystalline) surface. For the present experiment, the appropriate substrate temperature for the growth of (111) silver on mica, as noted by Pashley [12], lies in the range from 250° C to 300° C.

While precise data on the relationship between deposition rate and epitaxy are not available, the general observation is that higher deposition rates yield less perfect crystals. Similarly unavailable are details of the interrelations between residual gas pressure/composition and the structure of the deposited films, except for the anticipated observation that lowering the background pressure diminishes the contamination of the resultant crystal. As an example of acceptable limits on these factors, Smith and Saltsburg [1], operating with gold deposition rates of 10^{16} atoms/cm.^{2}-sec. in a typical oil-pumped vacuum system at background pressures near 10^{-7} torr, estimate, on the basis of simple kinetic concepts, a minimum ratio of gold to imbedded background gas molecules of approximately 100 for their films.

A fortuitous and helpful aside is provided by Jaeger [14] who has found that the presence of water vapor as a dominant background gas constituent and/or adsorbate on the substrate does not alter the quality of films

deposited at 300° C in the range 10^{-5} - 10^{-7} torr. He further notes that the defect concentration in such films is generally lower than that in films deposited on vacuum cleaved mica in ultra high vacuum at 300° C. The depositions performed here took place in the 10^{-7} torr range using vacuum-cleaved mica. Unavoidably, water vapor was a dominant constituent of the background atmosphere within the deposition chamber.

2.3 Deposition Apparatus and Procedure

In the design, construction, and operation of an evaporation source for silver deposition (or deposition of other metals) careful consideration must be given to a variety of factors. First, the purity of the melt obviously must be assured by careful handling as well as by thorough outgassing of the evaporator crucibles prior to use. Second, these crucibles must be of sufficient capacity not only to allow deposition rates of $\sim 10^{16}$ atoms/cm.^{2}-sec. for upwards of an hour, but also to contain sufficient reserves to guarantee the temperature stability of the melt during this time. Third, in order to insure reliability and efficiency, heating elements capable of the high power output required for prolonged periods are needed; these should also be adequately shielded to insure

optimum heating efficiency while simultaneously protecting any heat-sensitive system components in the vicinity of the evaporator. A final requirement for the system discussed here was that it must conform to some rather stringent space limitations imposed by the existing molecular beam apparatus. One common evaporator design, that used by Saltsburg and Smith [1], consists of winding a helix of tungsten heating wire around an alumina crucible and then potting the assembly with alumina cement. For the present experiments, there evolved from a variety of approaches the conceptually similar evaporator design whose basic elements appear in Figure 2.3.1. The heating element in this design consists of a series of parallel strips of 0.005-in. tantalum foil, 0.075-in. wide by 0.95-in. long bridged at alternate ends to form a continuous conductor. This element was cut from a rectangular sheet of the metal, then wrapped (as shown) around an 0.75-in. O.D. by 1-in. long cylindrical crucible of recrystallized alumina (Coors AD - 99). The crucible and encircling element were subsequently pressure-fitted into a steatite cap (DU-CO Ceramics, Saxonburg, Pa.) and the entire assembly set within a hollow cylinder of the same type of alumina used for the crucible. Tantalum was selected in view of its relatively high ductility which served to eliminate the problem of heater elements snapping as a result of repeated thermal expansion and contraction,

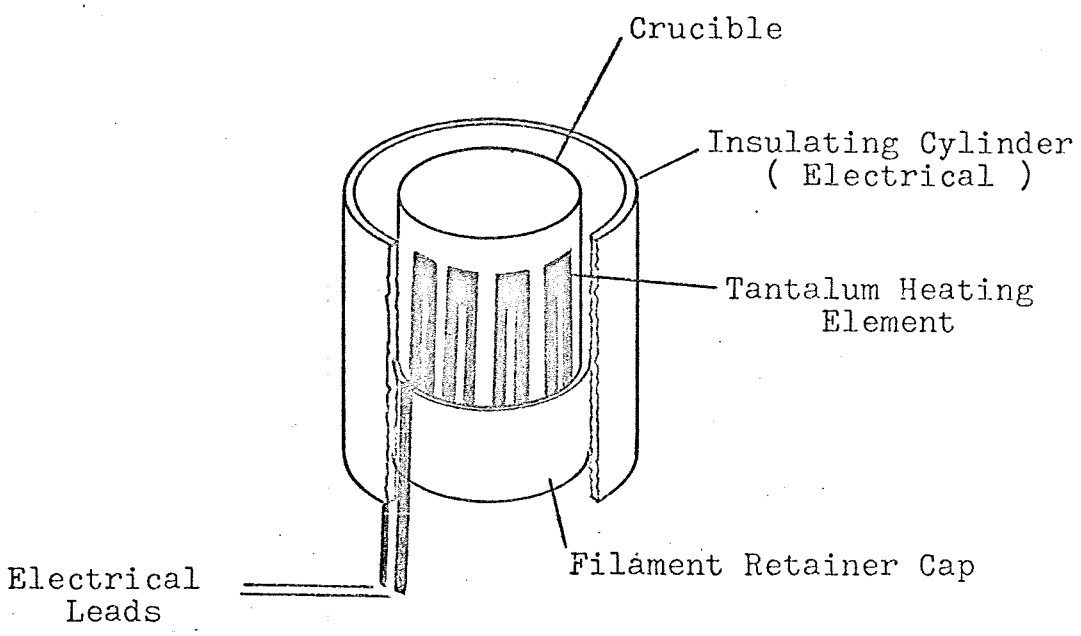

Figure 2.3.1 Basic Evaporator Components

a problem frequently encountered with the tungsten heater configurations tested. The present design also allows ready repair and/or replacement of a defective element without sacrifice of the associated crucible.

Two units of the type described were mounted on a rotatable support, similar in function to the cylinder of a revolver; this support was in turn suspended beneath a stationary stainless steel shielding disc upon which was mounted a collimating tube (the revolver barrel, by analogy). Either crucible could thus be rotated into alignment with the collimator (and hence into a position for vapor deposition) or else the pair of crucibles could be retained in a neutral position such that the collimator was closed to both cylinders simultaneously. The entire evaporator assembly was suspended from the target holder (See Section 3.3) as shown in Figure 2.3.2. Motion of the crucibles was effected by means of a rotatable mechanical feed-through.

The crucibles were located approximately 8 cm. away from the target face during deposition, while the collimator (a stainless steel cylinder approximately 2 cm. diameter by 2.7 cm. long) sat at a nearest distance of 3.5 cm. from the target center and at an inclination of 77° from the horizontal plane. It should be noted that the target face could be tilted toward the collimator sufficiently to reduce the angle of incidence (as measured from the target

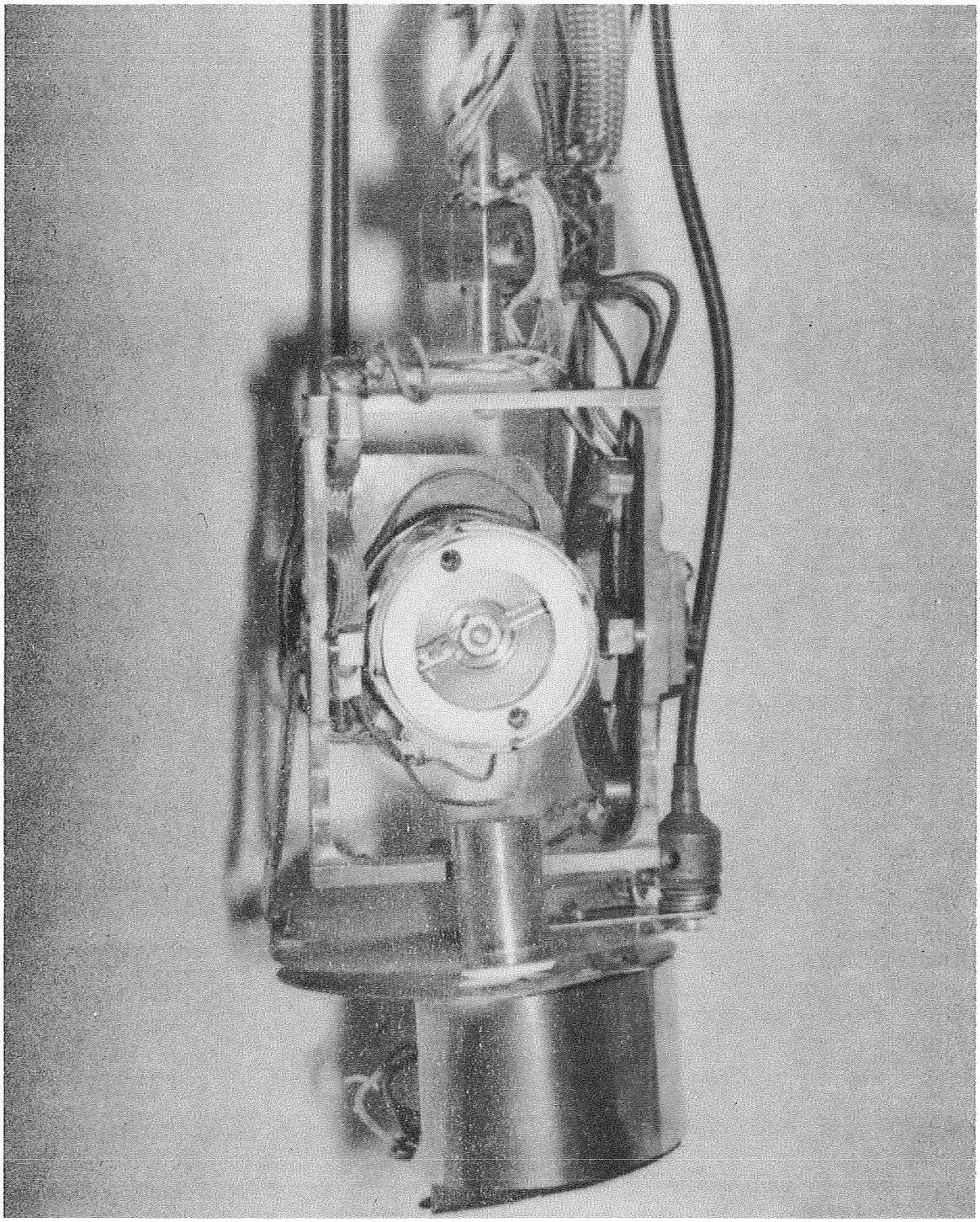

Figure 2.3.2 Target Holder with Evaporator Assembly

normal) to about 40° so as to more evenly distribute the silver over the target face.

Other structural components of the evaporator assembly were fabricated from stainless steel to insure durability and minimize contamination from oxides. The crucibles were surrounded with double radiation shields of 0.005-in. stainless steel foil.

To clean the evaporator system, it was necessary to bake the empty crucibles at approximately full power (i.e. at about 1200°C) for more than an hour in order to thoroughly degas the crucible material. As a matter of procedure, monitoring of the test chamber pressure was the most practical method of determining when outgassing had been satisfactorily completed.

The required power input for a given crucible may be determined by measuring crucible temperatures with an optical pyrometer or thermocouple during deposition, or simply by experimenting with a number of fixed inputs (and therefore fixed deposition rates) until the most suitable is found. This latter technique was adopted here because it provided the required power input most directly, namely, in terms of the quality of the film deposited at that rate.

High purity alumina crucibles, suitably outgassed, minimized the introduction of contaminants into the melt. To insure the purity of the melt itself, 99.99% pure silver

wire was coiled so as to fit inside the crucibles, then etched in a 1:1 HNO_3- water solution and rinsed in distilled water before insertion. Human contact with the degassed crucibles and etched silver was avoided.

This system, with the attendant procedures described, satisfied the requirements of the present study. The provision of two identical crucibles insured against filament burn-out terminating an entire set of experiments. Furthermore, this configuration provides the means of performing future studies using two different metals (e.g. the growth of gold crystals on silver substrates).

CHAPTER 3

EXPERIMENTAL DETAILS

3.1 Molecular Beam System

The atomic beam system in which these experiments were performed has been described in detail by its developers [17], [18], [19] and consequently the presentation to follow will be limited to those details necessary to familiarize the reader conceptually with the system's basic components and their respective functions. A complete explanation of the generation of the atomic beams is relegated to the references cited above as is coverage of the technical intricacies of the electronics employed to monitor the scattered beams.

Figure 3.1.1 reveals schematically the relative positioning of the three basic component systems within the vacuum chamber —— the collimated atomic beam source, the target specimen, and the movable time-of-flight detector assembly. Visualization of the beam scattering geometry will be simplified for the reader by first considering the case in which the incident atomic beam and target normal both lie in the horizontal plane of motion

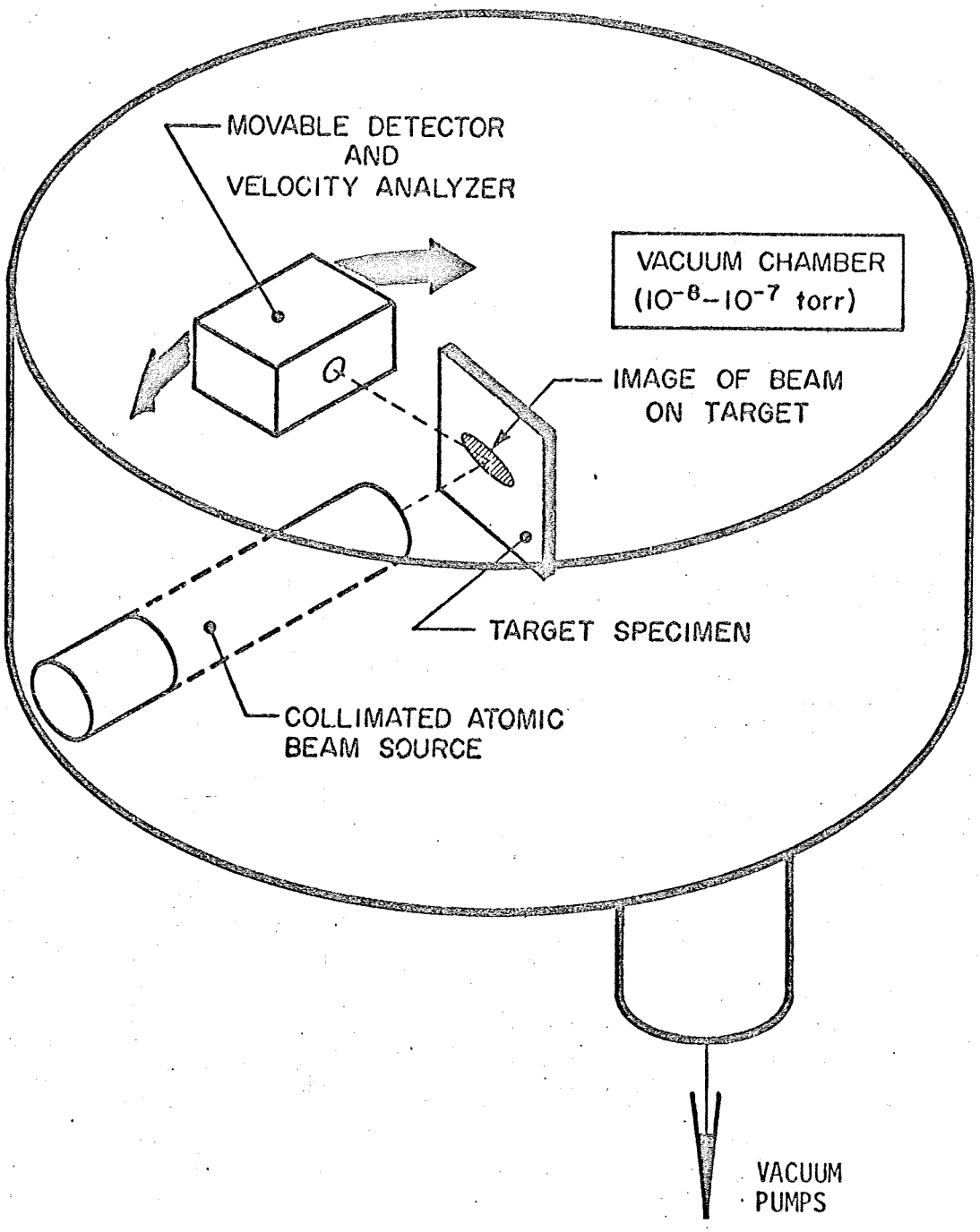

Figure 3.1.1 Schematic Drawing of the Apparatus

of the detector. Viewed along the vertical axis of symmetry of the cylindrical test chamber, the essential components of the three basic subsystems mentioned above appear as shown in Figure 3.1.2.

The beam gas expands from a high pressure source through a miniature converging nozzle into the first chamber of a three-stage, differentially pumped vacuum tank. The core of this freely expanding jet is successively defined by the skimmer and collimator as it passes, respectively, into the second (collimating) and third (test) chambers. The resultant beam, incident upon the target at an angle θ_i (measured from the target normal), has an angular divergence such that 90% of the atoms are within $\pm 3^\circ$ of the nominal direction of incidence and a speed divergence such that 90% have speeds within $\pm$ 7% of the mean speed.

The detector can be positioned at any desired scattering angle, θ_r (likewise measured from the target normal), in the horizontal detector-sweep plane defined by the physical structure of the test chamber [$40^\circ < (\theta_i + \theta_r) < 190^\circ$]. Flux scattered from the target toward the detector passes, in succession, through a pair of apertures —— one located just behind the chopper disc, the other located as close as possible to the detector active zone. The first of these excludes from entrance

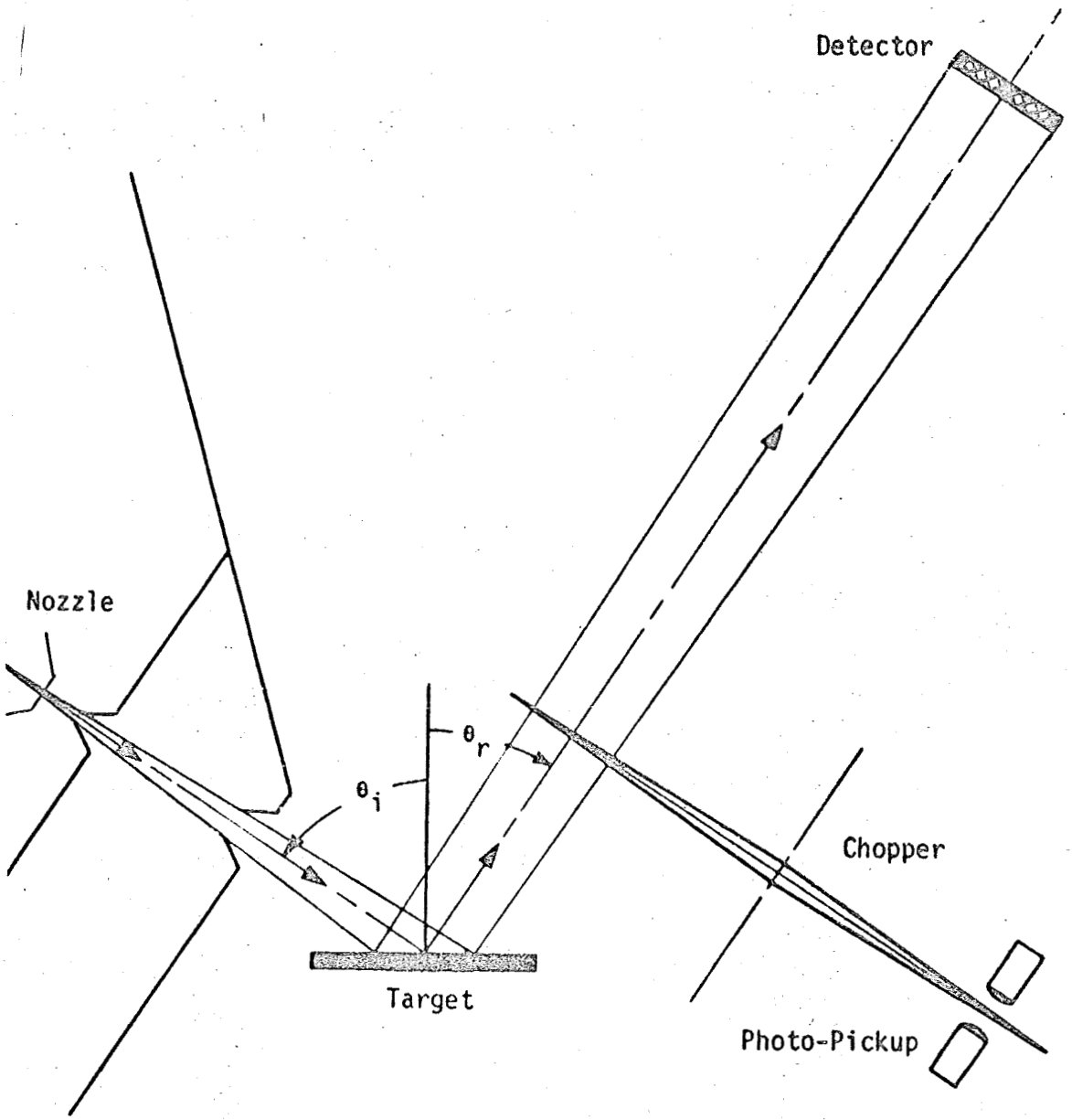

Figure 3.1.2 Basic Geometry of the In - Plane Scattering and Detecting System

into the detector effectively all unwanted modulated particles emanating, for example, from structural members of the target holder; the second defines the solid angle of flux admitted into the detector active zone and is positioned to obtain the desired angular resolution with a minimum attendant loss of beam intensity. The relative locations of the components described above, along with the more important dimensions associated with their layout, appear in Figure 3.1.3 and are tabulated in the accompanying Table 3.1.1. In the configuration established for the present experiment, the previously employed chopper-detector separation of $\approx$ 25 cm. [17], [20] was doubled to 50 cm. (the maximum allowed by the dimensions of the existing test chamber) in order to improve both angular resolution and obtainable speed resolution. With a detector aperture designed to just expose the full area of the detector active zone, the system possessed an angular resolution of $\pm 2^{o}$ or better (resolution being poorest in the vicinity of the normal for large incident angles).

3.2 The Time-of-Flight Detection System

The speed distribution of the flux scattered into

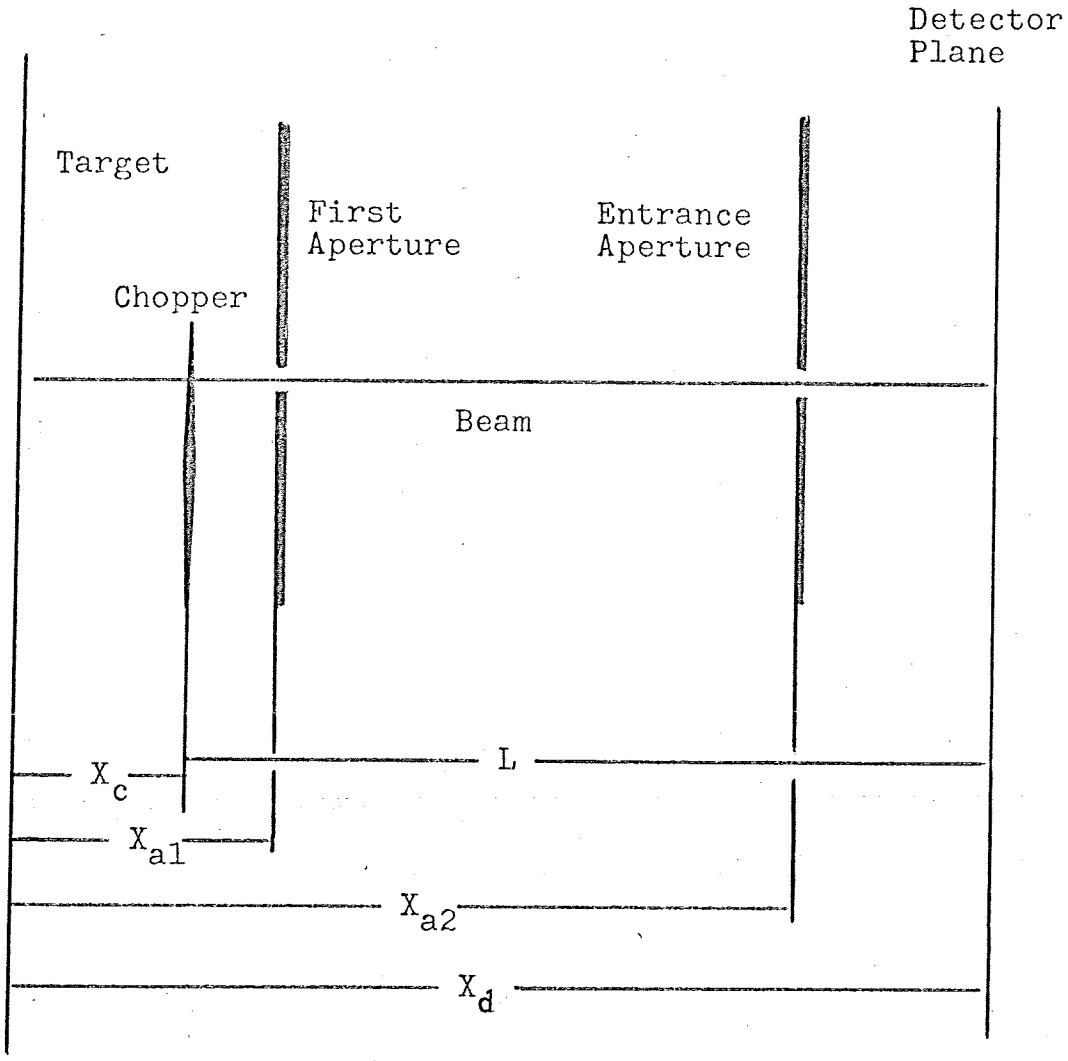

Figure 3.1.3 Basic Distances of the Scattering System

Table 3.1.1

Basic System Dimensions as Employed in the Present Experiments

L	50.0 cm.
X_c	5.6 cm.
X_{a1}	6.75 cm.
X_{a2}	47.9 cm.
X_d	55.6 cm.
First Aperture	2 cm. x 0.32 cm.
Entrance Aperture	1.7 cm. x 1.3 cm.
Detector Plane	1.8 cm. x 1.6 cm.

NB: Areas are presented in terms of "width x height".

the detector at any position is determined by means of a time-of-flight method, a detailed analysis of which has been presented in a previous reference [19]. The following outline freely employs idealizing simplifications in order to facilitate comprehension of the basic functions of the system and its various components.

That portion of the incident atomic beam scattered at the target surface in the direction of the detector impinges upon a rotating chopper disc (Figure 3.1.2) constructed with four radial slots spaced symmetrically about its periphery at 90° intervals. As each of these slots passes across the flightpath to the detector, a small packet of beam atoms is allowed to pass through the disc and to proceed toward the detector. One may speak, then, of a chopper which "gates" the molecular beam. Simultaneously, that slot diametrically opposite the "gate" slot exposes a photosensitive field-effect transistor to a light source and registers the start time for each packet. Just beyond the chopper, each beam packet displays a "shutter function" density distribution [19] along the flightpath. As the packet proceeds toward the detector, then, this density distribution continually disperses itself due to the differing velocities of the molecules it contains.

At the detector active zone, a fraction of these molecules proportional to the instantaneous local density

is ionized by an electron sheet approximately 1 mm. thick in the direction of travel. The ions formed are almost immediately gathered in at an ion collector thereby generating a current proportional to the instantaneous density within the detector as a function of time. This current is, in turn, passed across a load resistor to produce a potential difference. The potential difference is then suitably amplified, electronically mixed with the timing signal from the photocell, and finally processed through a multichannel signal-averaging device to yield a distribution of detector signal voltage, $S_d(t)$, superimposed upon the timing signal intensity peak. Here $S_d(t)$ is proportional to the beam density at the detector and t is effectively the time-of-flight of the detected molecules over the flightpath L. The signal $S_d(t)$, after averaging over some 80,000 "gated" cycles in order to reduce the net noise, is stored in the signal averager until it can be read out at a slow rate into a standard X-Y plotter.

The recorded $S_d(t)$ information can be converted into a differential intensity versus molecular speed distribution from which such useful averages as the net scattered intensity, mean speed and rms spread in speeds can be readily computed as appropriately weighted integrals over this distribution. If the time-of-flight density distributions are well resolved, the intermediate

conversion is unnecessary. The integrations may be carried out in equivalent forms using time-of-flight distributions directly.

3.3 Target Holder and Related Coordinate Systems

The foregoing discussion has been predicated upon the restriction that the incident beam, the target normal, and the detector are coplanar. Clearly it is desirable to achieve the freedom of monitoring the flux at an arbitrary set of scattering angles relative to the target face. To realize this end, a gimballed target-mount, that shown in Figure 3.3.1, is employed. This mount was designed by Bishara [20] for previous research and adapted to accept the vapor deposition apparatus previously described in Section 2.3.

Details concerning the design and function of this mount appear in the reference just cited. It is sufficient here to note that the target is provided six degrees of freedom: three in translation and three in rotation. The former allow for precise location of the target face with respect to the incident beam and detector flightpath; the latter serve to obtain the desired orientation of the target with respect to these reference directions. The

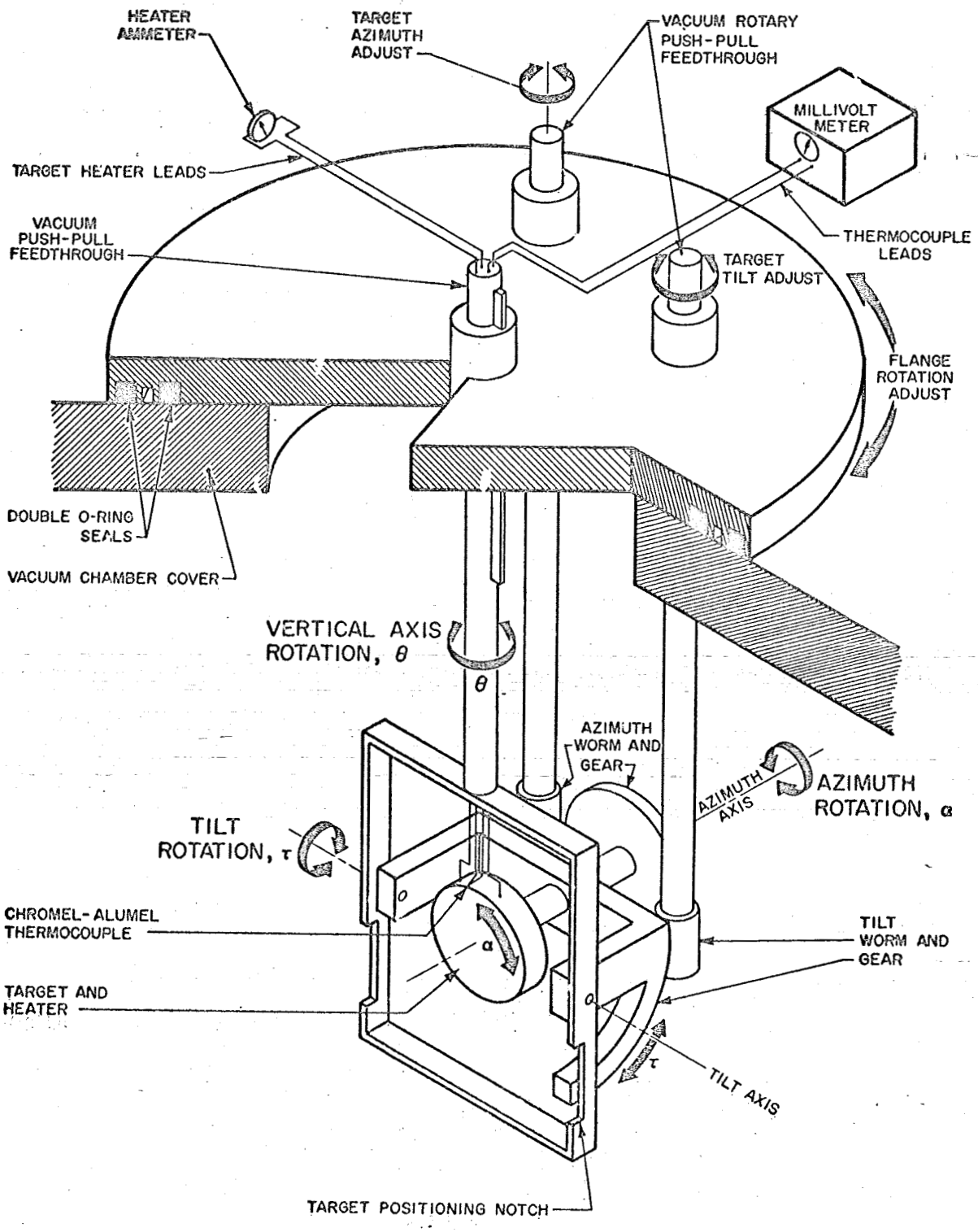

Figure 3.3.1 Target and Target Mount

three rotations are:

1. a vertical rotation, θ, which rotates the target about the detector sweep axis;
2. a tilt rotation, τ, which rotates the target about a horizontal axis perpendicular to the target normal;
3. an azimuthal rotation, α, which rotates the target about its normal.

The incident beam is fixed and physical limitations on the detector apparatus require that the detector line of sight always lie in a fixed horizontal plane. Thus, the function of this gimballed target-holder in any given scattering experiment is to rotate the target about an axis coincident with the incident beam so as to effectively place the detector in a position outside the plane of incidence while maintaining the same orientation of the incident beam relative to the target face. For any given target orientation, then, the detector may be swept through a set of positions in its horizontal plane in order to obtain a partial mapping of the scattered beam. A sequence of such detector sweeps for selected rotations of the target about the incident beam thus allows as complete a mapping of the scattered beam as the

experimenter desires.

The three rotational angles listed above (θ, τ, α) are not natural angles for the desired target rotation. Consequently, a complicated set of transforms must be solved, first to obtain the desired rotation sequence of the target about the incident beam in terms of (θ, τ, α), then, for any fixed target orientation in the sequence, to interpret the detector sweep positions in the horizontal plane in terms of a set of target-fixed coordinates. Such transforms have been developed for previous experiments by Bishara [20] and the necessary relationships have been computed and tabulated in the laboratory. A discussion of these transforms is presented in Reference [20].

Figure 3.3.2 shows the target-fixed coordinate system to be used in presenting the data. Immediate attention is given to the two distinct planes and two related axes clearly evident in this figure. The principal plane (generally referred to in the literature as the plane of incidence) is that plane defined by the incident beam vector $\hat{i}$ and the centered target normal $\hat{n}$; its intersection with the target face is, accordingly, termed the principal axis. The axis lying in the target face perpendicular to the principal axis and joining it at its intersection with $\hat{n}$ is called the transverse axis, and the plane sweeping upward from it through some scattering

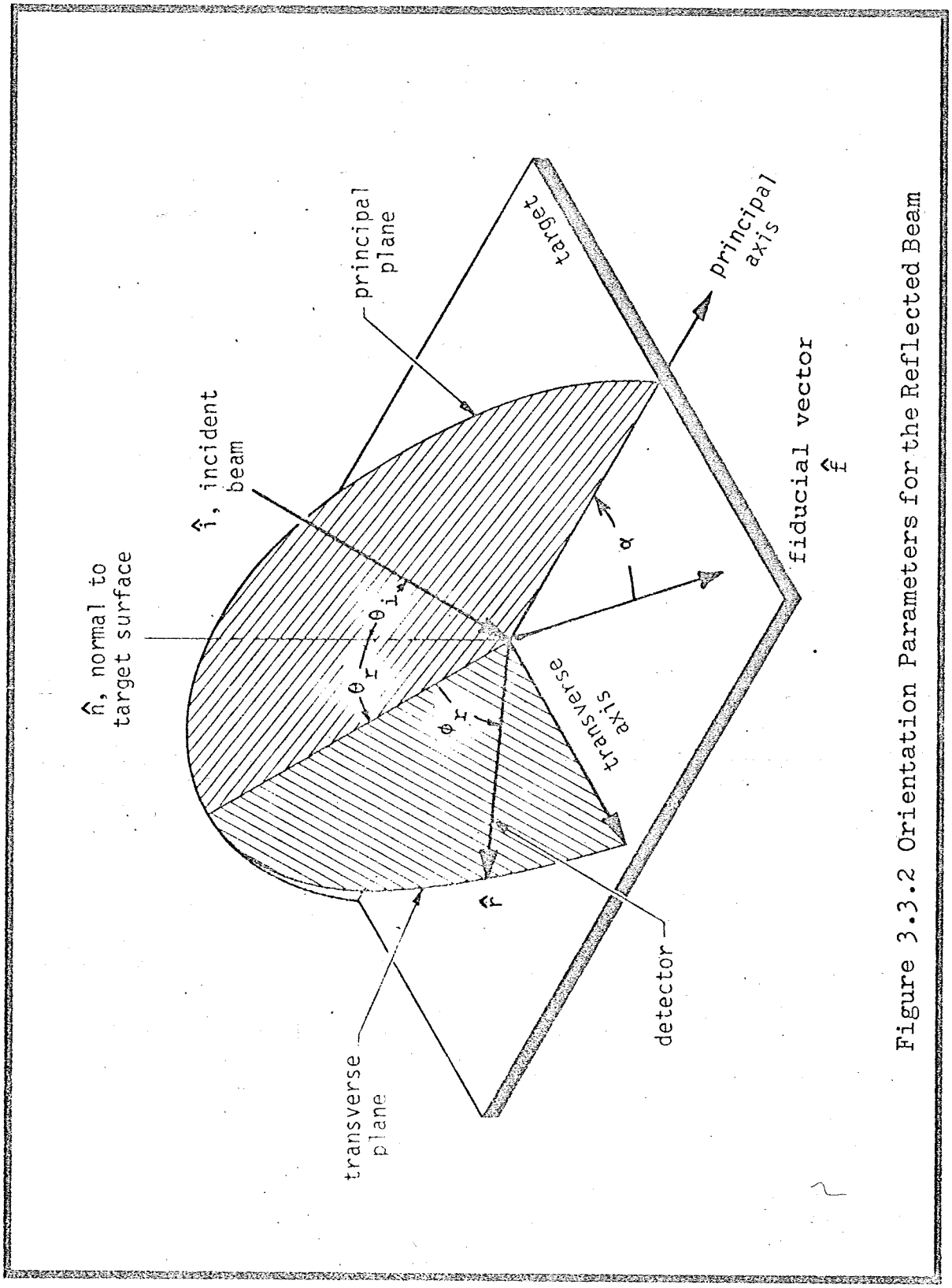

Figure 3.3.2 Orientation Parameters for the Reflected Beam

vector, $\hat{r}$, is, by analogy, called a transverse plane.

The incident beam vector, $\hat{i}$, is defined by the angles θ_i and α , where θ_i is the polar angle (measured in the principal plane as shown) and α is an azimuthal angle measured to the principal axis from a fiducial direction vector, $\hat{f}$ (defined relative to the target's crystallography). Similarly, a given scattering direction, $\hat{r}$, is described in terms of two angles, θ_r and ϕ_r, where θ_r is measured in the principal plane and ϕ_r is measured in the transverse plane as shown in the figure. At times, θ_r is referred to as the "in-plane" scattering angle and ϕ_r as the "out-of-plane" scattering angle. Not shown in this figure is a detector location angle, δ , measured between $\hat{r}$ and negative $\hat{i}$; this angle will be employed in later discussions.

The choice of these angles is primarily for the ease with which they lend themselves to the description of lobular scattering patterns; these angles and the notation used here are commonly employed by investigators in this discipline.

3.4 Data Processing

The treatment of the TOF method in Section 3.2

outlined the process whereby a graph of the distribution of signal intensity vs. time-of-flight is generated at each observed scattering direction. Figure 3.4.1 depicts a representative distribution of this type and defines the principal parameters associated with it. These are the signal maximum, $S_d(t_m)$, occurring at time t_m, and the two times, t_1 and t_2, where the signal half-maximum occurs.

The three basic moments of the speed distribution employed in previous studies originating in this laboratory are:

1) Intensity, I_r (atoms/sec.-steradian)
2) Mean speed, $\langle v_r \rangle$, and
3) Mean square thermal speed,
$\langle c_r^2 \rangle = \langle v_r^2 \rangle - \langle v_r \rangle^2$.

The method by which these parameters are determined from the recorded data has been presented in detail in earlier reports from this laboratory [17], [19], [20]. A summary of that method, along with some pertinent details concerning modifications employed in processing the data contained herein, is to be found in Appendix I. Briefly, this method is based upon a curve-fitting technique which enables these three moments to be evaluated to within reasonable accuracy on the basis of three

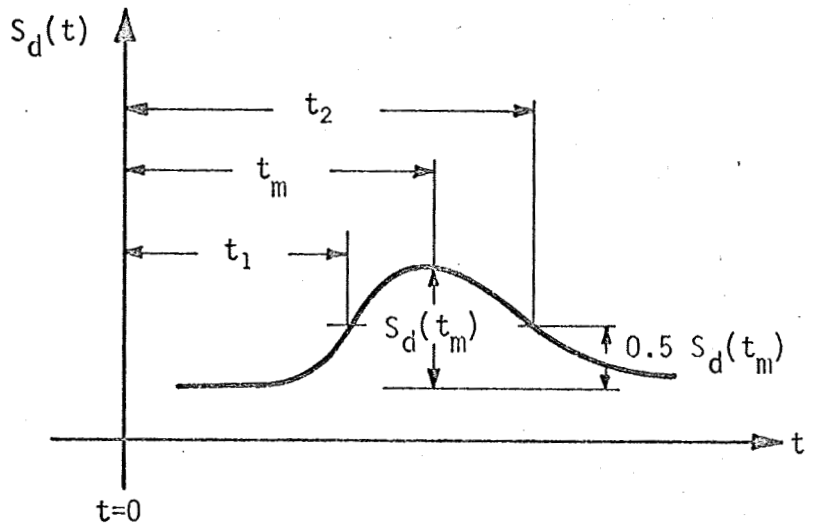

Figure 3.4.1 Typical TOF Signal

representative measurements, t_1, t_2, and $S_d(t_m)$, made from the recorded distributions. When the time-of-flight measurement resolution, R, is high, where $R = \Delta t/t_{so}$, $\Delta t = t_2 - t_1$, and t_{so} is the time-halfwidth of the initial "shutter-function" pulse as it leaves the chopper, it is possible to fit a model function to the time-of-flight trace with reasonable accuracy by matching this model function to the trace at times t_1 and t_2 and at the maximum amplitude, $S_d(t_m)$, thus determining three free constants in the model function. Further analysis based upon this fit yields polynomial fits for $\langle v_r \rangle$, $\langle v_r^2 \rangle$, and $\langle c_r^2 \rangle$ as functions of the two parameters, L/t_2 and t_2/t_1, where L is the length of the flightpath. The intensity of the flux passing through the detector is computed from a similar approximate relationship derived on the basis of the model function.

In the above, the data were assumed to be highly resolved from a TOF standpoint, i.e., to be taken under conditions such that, say, $R \geq 5$. Unfortunately, due to the physical limitations of the system it was often impossible to obtain such resolution and, consequently, corrections to the data had to be introduced. These corrections, somewhat approximate, were based upon the work of Hagena and Varma [19]. They also are discussed in Appendix I.

It should be mentioned that additional, higher order moments of the speed distribution can, in principle, be computed in an analagous manner. The choice of the three listed above is predicated primarily upon their ready interpretability and upon the adaptability of their approximate determination to curve-fit techniques. Higher moments are less readily interpreted and would be of questionable accuracy as determined by the present medium resolution curve-fitting techniques.

3.5 Error Analysis

Uncertainties in the measurements arise from three sources:

a) Mechanical or geometrical imperfections,
b) Electronic calibration and/or stability problems,
c) Uncertainties involved in the process of reducing raw data.

These error sources have been tabulated by a previous experimenter [20] and reference will be made to his results in enumerating the degrees of uncertainty inherent in this equipment. His estimates must be modified, at least in

part, due to subsequent changes in the apparatus.

3.5.1 Mechanical Systems

Calibrations performed by the designer [20] and confirmed herein indicate that the target-holder angles, Θ and τ, can each be set to within $\pm 1^{\circ}$, while the azimuthal angle, α, is limited to $\pm 2.5^{\circ}$ of its nominal value. Calibration of the detector sweep angle, δ, indicates that it too can be set to within $\pm 1^{\circ}$. Based upon these measurements, the computed angles Θ_r, ϕ_r, and Θ_i can generally be attributed accuracies comparable to those for τ, Θ, and δ. (Note, though, the discussion of α-axis wobble below.) To insure these accuracies, care is taken to always approach angular settings from the same direction so as to minimize backlash-induced error. This is especially necessary with the motorized detector sweep mechanism since it employs a flexible coupling in its drive shaft.

The above cited tolerances are predicated upon locating the center of the target face so that it coincides with the (built-in) intersection of the beam centerline and the vertical axis of rotation of the detector support table. This location was accomplished by projecting a

laser beam along predetermined alignment paths and was accurate within 1 mm.

By taking advantage of the high reflectivity of the target surface, the laser was also employed to observe the wobble of the target surface with variation of the azimuthal angle, α (spinning the target about its normal). Sweeping through a range of 180° in α while observing the near normally reflected laser beam indicated that the wobble was no more than $\pm 1^{\circ}$.

This wobble was not due to any random motion of the α -axis in a loose mounting channel, but rather to a deviation of the target normal by approximately 1° from coincidence with the α -axis. This conclusion evolved from the ability to repeat any reading within about 0.2°. Thus, experiments performed at similar α -settings suffer this lesser uncertainty with respect to the orientation of the target normal relative to the α -axis.

3.5.2 Electronic Systems

Tests performed by the system's designers [18], [20] have determined that the net frequency response of the detector with its signal amplification, averaging, and recording train falls well within the requirements for

their studies. For the present experimental sequence, wherein the flightpath length L has been doubled, thus doubling all time scales as well, high frequency response of the electronics is even less of a problem and the error due to limited low frequency response of the electronics surely remains small compared to the scatter in the recorded data.

Johnson noise in the preamplifier "load" resistor is the primary source of the high frequency fluctuation in the detector signal. In previous work, the signal-to-noise ratio (SNR) in the recorded time-of-flight (TOF) detector signals, after averaging, ranged from 20 to 200. Here, with L doubled and the signal level thus reduced by approximately a factor of four due to beam spreading, SNR is accordingly reduced to a minimum of about 5 for the least intense argon beams. Nevertheless, highly reflecting beams of helium still display SNR $\approx$ 100. Such finite noise in the recorded signal will show up as scatter in the results to be presented. Variation in beam intensity and drift in the electronics are rated here at about $\pm$ 1% each, based upon the repeatability of data points from hour to hour.

Thermocouple measurements made at the target display two distinct types of error. The first of these comprises random errors associated with imperfect thermal contact,

instabilities in the voltage metering system, variations in the "room-temperature" reference point, and the lack of precision of the simple linear conversion used to obtain "^{o}K" temperature readings from thermocouple emfs. The second comprises systematic errors resulting primarily from the location of the thermocouple between the substrate and radiant heat source (causing elevated temperature readings) and secondarily from changes in line resistance due to heat flow along the thermocouple wire. When the surface temperature is being measured near equilibrium, the random error is valued at $\pm 10^{o}$K and the systematic elevation above surface temperature at 10^{o}K . During heating the random error climbs to $\pm 15^{o}$K and systematic elevation to 50^{o}K . When the surface is monitored during cooling, the random error is set at $\pm 15^{o}$K and the systematic elevation at 15^{o}K . These estimates all represent upper limits on errors present in the data.

3.5.3 Data Reduction

Errors in the data reduction process arise primarily from two sources: the degree of precision lost in determining the three quantities t_1, t_2, and $S_d(t_m)$ from the recorded TOF traces (see Figure 3.4.1), and the degree of

precision sacrificed to tractability in the curve-fit determinations of the desired beam properties. Measurement errors in determining the time, t=0, from the photocell signal are placed here at ± 4.0 to 8.0 milliseconds and additional errors in measuring t_2 and t_1 from that reference contribute an uncertainty of ± 8.0 to 12.0 milliseconds more. Errors in measuring $S_d(t_m)$ are inversely proportional to the values of SNR reported earlier; that is, these errors range from ± 1% of $S_d(t_m)$ for the strongest signals from scattered helium beams to as much as ± 20% for many of the argon signals.

Computational errors introduced through use of the curve-fit method are best discussed in terms of their effect upon the individual quantities calculated. Systematic errors in the normalized intensity, $[I_r]$ (see Section 5.1.1 for definitions of this and the other normalized parameters and normalizing factors to be mentioned), are estimated as follows: for argon, systematic errors due to use of this curve-fit technique are less than ± 10%; for helium, these errors are less than ± 5%. Such systematic errors are generally on the same order of magnitude as the scatter in the data.

Values of the normalized mean speed of the scattered atoms, $[v_r]$, are systematically low due to curve-fit effects. For helium, $[v_r]$ is 4% to 7% low while for argon, $[v_r]$

is 3% to 4% low. These estimates for argon are based upon comparisons between curve-fitted and integrated values of $[v_r]$ calculated by Bishara [20]. For helium they reflect the extent to which $[v_r]$ evaluated at the specular fails to equal $[v_i]$. In view of the large intensity peaks associated with these data, specularly directed helium scattering is surely the result of effectively "single" atom-surface collisions which, because of the disparity between the atomic masses of helium and silver, should be essentially elastic, i.e. involve virtually no change in helium speed.

Finally, the exact magnitude of the spread in speeds, $[\Delta S_r]$, is not critical since, in the present study, this term serves primarily as an indicator of the nature of the interaction; the systematic error introduced into $[\Delta S_r]$ by curve fitting is estimated nominally at $\pm 10\%$.

For each of the three curve-fitted parameters, the scattered intensity, I_r; mean speed, $\langle v_r \rangle$; and speed spread, $\langle \Delta S_r \rangle$, there is an analagous quantity attributable to a perfectly diffuse, perfectly Maxwellian scattering process which serves as a normalizing factor in generating the plotted parameters $[I_r]$, $[v_r]$, and $[\Delta S_r]$. (Again refer to Section 5.1.1 for definitions.) These normalizing factors are, respectively: I_s, $\langle v_s \rangle$, and $\langle \Delta S_s \rangle$.

The last of the three is simply a number; the second is proportional to $(T_S)^{\frac{1}{2}}$ and may be attributed error limits based upon the discussion of T_S in the previous section. The analysis of errors in I_S is more involved. I_S is defined as the scattered intensity measured at the normal for a diffusely scattering surface. In practice, its value is determined from the most nearly diffuse data obtained for each beam gas during the course of an experimental series. Since the detector signals involved are only of moderate strength, the error in I_S for helium is evaluated at $\pm 10\%$, that for argon at about $\pm 20\%$. Fortunately, I_S has a single value for each gas throughout the experiments performed and hence does not diminish the accuracy of comparisons between selected data sets. For convenience, the principal sources of error in the plotted moments are presented in Table 3.5.3.1 along with the magnitudes of the errors induced.

Table 3.5.3.1

Principal Sources and Magnitudes of Errors

Error Source	Magnitude of Error in: $[I_r]$	$[v_r]$	$[\Delta S_r]$
1. Curve-fit (systematic):			
Argon	±10%	- 3-4%	±10%
Helium	± 5%	- 4-7%	±10%
2. Normalization (systematic):			
Argon	±20%	- 3-6%	____
Helium	±10%	- 3-6%	____
3. Random:			
Argon	±20%	±4%	± 7%
Helium	± 5%	±4%	±10%

Note: The error magnitudes cited above are upper limits.

CHAPTER 4

PROCEDURE

The brief treatment to follow is intended to present the general sequencing of the experiments from which derive the data to be discussed in the following chapter. Since these experiments were as much an exercise in developing techniques and defining the operational limits of the apparatus as they were a result of a rigorously followed, predetermined sequence, their course reflects a considerable flexibility intended to enable the pursuit of interesting directions as these were encountered.

Once the crucibles had been prepared and filled in the manner described in Section 2.2, a 1-in. diameter disc was cut from a selected sheet of muscovite mica[1] and mounted in the target holder so as to physically contact a chromel-alumel thermocouple sandwiched between it and the notched quartz disc used for its support. (See Figure 4.1.) Adjustments were then made to align the surface with the center of the τ-axis and to establish the point at which $\tau = 0$. A strip of "Magic" transparent tape was pressed onto the mica; the target face was then tilted up and the

[1]Obtained from: Mica Products Co., 2330 Beverly Blvd., Los Angeles, California, 90057.

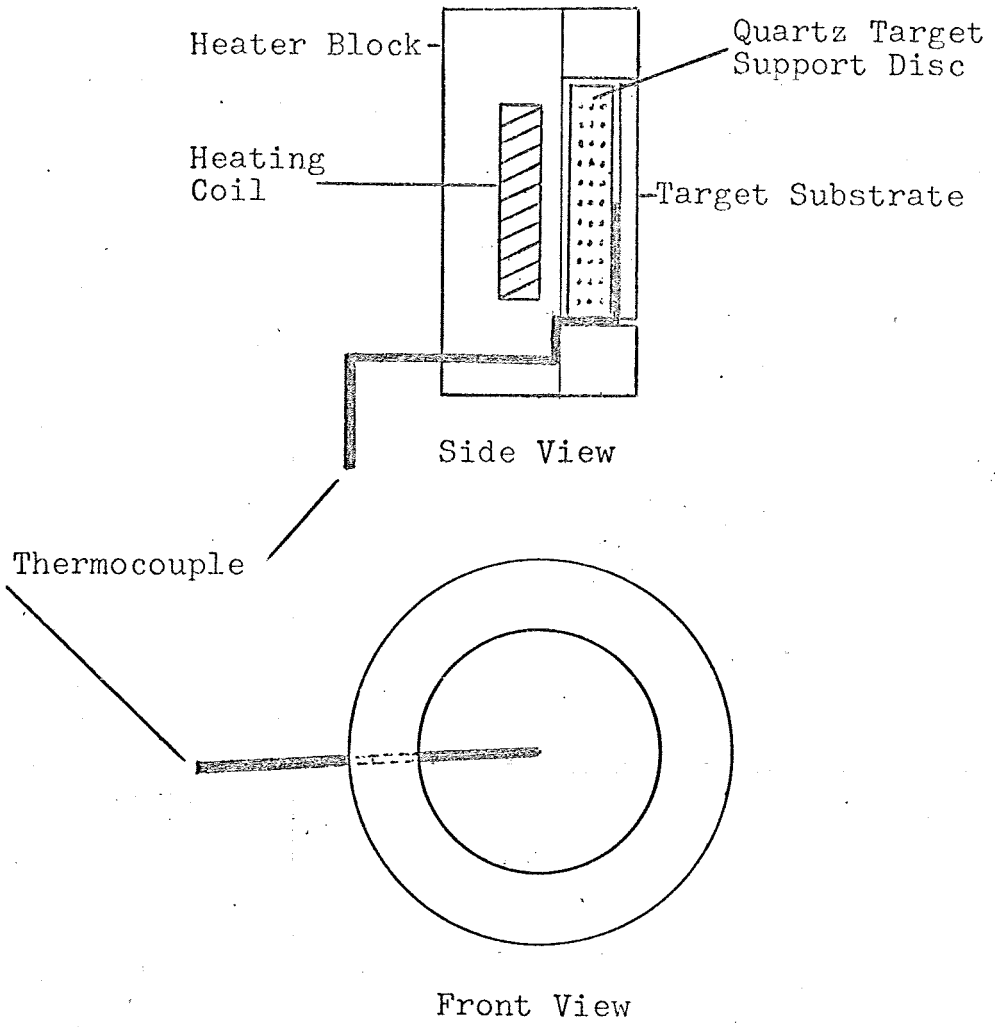

Figure 4.1 Schematic View of Target Mounting Block Showing Thermocouple Placement

other end of the tape was fixed to a retractable arm. Subsequently, the target-evaporator unit was installed in the vacuum system and overnight pump down to 10^{-7} torr commenced.

On the following day the mica substrate was "cleaved" by simply retracting the arm to which the tape had been attached thus peeling off the tape which, in turn, carried with it a thin sheet of mica. The "clean" substrate was then tilted toward the collimator mouth as both the target and the "active" crucible were simultaneously heated. During this time the "active" crucible was out of alignment with the collimator to avoid desorption of contaminants onto the substrate. Once the substrate thermocouple reading had stabilized at 600°K and the crucible had been raised to the power level previously determined to give the desired deposition rate, the crucible was rotated into alignment with the collimator and deposition commenced. After about 15 min. of deposition, the crucible was rotated out of line and cooled. At this time the alignment of the target holder was checked with a laser in the manner previously discussed (Section 3.5.1) and necessary adjustments performed.

The helium beam selected for initial exploration of the surface was then admitted into the test chamber and the beam intensity was maximized by adjusting the source pressure and nozzle-skimmer separation to their respective

optima as determined by direct observation of the incident beam. The target could be temporarily translated out of the beam path for direct beam observations. With the target so displaced, the detector was swept in its horizontal plane across the incident beam to establish the angular position of greatest intensity; this position was designated as the detector-angle reference condition, $\delta = 180^{\circ}$. Thereafter, a series of incident beam TOF distributions were recorded as a function of chopper speed for both a forward and a reversed motor rotation in order to establish the exact location of the time, $t = 0$, for the TOF traces. (This last procedure was repeated for strong reflected beams as well.) These preliminaries were completed at about 2 hrs. of elapsed experimental time. (All experimental times considered are measured from the cessation of deposition.)

With the surface temperature maintained at $600^{\circ}K$, the set of scattering studies recorded in Section 5.2.1 was performed. This sequence was completed after about 30 hrs. of elapsed time. The target was then cooled slowly to $300^{\circ}K$ and exposed at this temperature for five days to a background pressure of $\sim 10^{-2}$ torr. At the end of this period the test chamber was again pumped to the 10^{-7} torr range and the experiments detailed in Section 5.2.2 commenced. At 192 hrs. of elapsed time an attempt was made to deposit a fresh film while simulta-

neously scattering helium. During deposition a dull, elliptical blotch (later found to be polycrystalline) appeared on the target face. (See Figure 4.2.) To determine the effects of this surface aberration on overall scattering behavior, exploratory α-sweeps and principal-plane sweeps were performed for comparison with data previously recorded. These results are discussed in Section 5.2.2.

The surface was next exposed to an argon beam whose intensity had been optimized in the manner previously described. The sequence of experiments performed and their results appear in Section 5.3.

At 296 hrs. elapsed time, the helium beam was reintroduced and data taken at $T_S \approx 700^{\circ}K$. (See Section 5.2.2.) Following this, an attempt was made to determine dominant adsorbates by cooling the target to $300^{\circ}K$, then flashing it to $\sim 800^{\circ}K$ while facing a continuously operating mass spectrometer. The results of this effort are to be found in Section 5.5.

The rapid heating during the desorption study roughened the target surface. The effects of this roughening on helium scattering were explored in a terminal sequence of experiments whose results appear in Section 5.2.3.

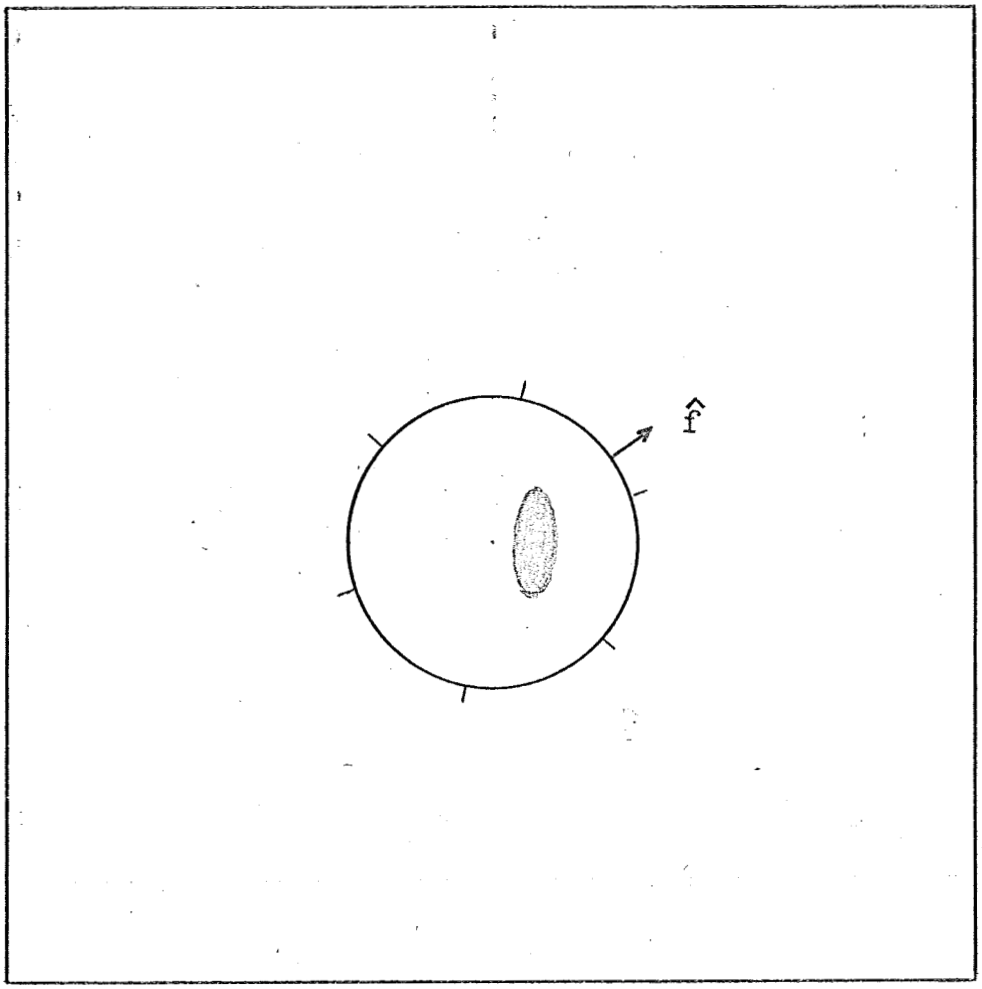

Figure 4.2 Drawing of the Target Face Showing the Polycrystalline Blotch, the Fiducial Direction, $\hat{f}$, and the [[111]] Surface Lattice Directions.

CHAPTER 5

DATA

5.1 Preliminary Considerations

5.1.1 Parameters Plotted

It is instructive to comment on the nature and significance of the quantities to be plotted in this chapter and to discuss, in a general way, the implications of their behavior. Recall that in Section 3.4 the extraction of four moments from the experimental speed distributions was discussed. These moments were:

1. the intensity, I_r;
2. the mean speed, $\langle v_r \rangle$;
3. the mean square speed, $\langle v_r^2 \rangle$;
4. the mean square thermal speed, $\langle c_r^2 \rangle$.

A subset of these moments used for their normalization is that for the case of perfectly diffuse scattering with full thermal accommodation. This subset is defined as follows in terms of the measurable parameters of the

experimental system:

1. $I_s = I_r$ at the target normal for such a diffusely scattering target. (5.1.1.1)

2. $\langle v_s \rangle = (9\ \pi kT_s/8M_g)^{\frac{1}{2}}$ (5.1.1.2)

3. $\langle v_s^2 \rangle = (4kT_s/M_g)$ (5.1.1.3)

4. $\langle c_s^2 \rangle = [(32 - 9\ \pi)\ kT_s/8M_g]$ (5.1.1.4)

where T_s = surface temperature,
M_g = mass of incident gas molecule, and
k = Boltzmann gas constant.

Effecting the suggested normalization generates the following three quantities which will be used in describing the measured properties of the scattered beams:

$$[I_r] = I_r/I_s \qquad (5.1.1.5)$$

$$[v_r] = \langle v_r \rangle / \langle v_s \rangle \qquad (5.1.1.6)$$

$$[\Delta S_r] = (S_r/S_s)^{\frac{1}{2}} \qquad (5.1.1.7)$$

where $S = \langle c^2 \rangle / \langle v^2 \rangle$.

The first two of these normalized moments are of obvious significance. The third is a measure of the spread in speeds of the scattered flux, henceforth referred to as the "speed spread." As defined, it is the rms variance of the speed distribution about its true mean divided by the rms value, $\langle v^2 \rangle^{\frac{1}{2}}$, and then normalized to unity for a Maxwellian speed distribution. Note that in previous investigations published by this laboratory, [20], [21], [22], the quantity S_r / S_s has been called the "spread" or "thermal spread." Thus, the present usage represents a change in nomenclature, an improved usage it might be added, since S_r/S_s is not in fact (as alluded to in the above references) proportional to the spread in energies of the reflected molecules. However, $[\Delta S_r]$ is roughly proportional to the spread in speeds about the mean. In considering these quantities it should be noted that S_s is simply a number $(32 - 9\pi)/32$ and hence, independent of T_s. (This is not true of $\langle v_s \rangle$, for example.)

5.1.2 Speed Distributions

It is reasonable to expect that a knowledge of the complete velocity distribution of a molecular beam both

before and after interaction with a surface should prove useful in deducing the nature of that interaction. By selecting experimental situations such that the energy transferred either to or from a gas atom is predominantly in its translational modes, it is possible to employ the mean speed, $[v_r]$, and spread in speeds, $[\Delta S_r]$, of the scattered gas to yield information concerning the extent of energy exchange and the physical mechanism by which it is effected. The difference between $[v_i]$ and $[v_r]$ serves to indicate the direction of energy transfer (to or from the gas) while the difference between $[\Delta S_i]$ and $[\Delta S_r]$ provides a measure of the randomizing effect of the interaction as a whole.

In terms of specific limits, it is anticipated that $[v_r]$ will have values nominally between $[v_i]$ and $[v_s]$ (unity), depending upon the extent of energy transfer. For the majority of experiments treated here, conditions are such that $[v_i] < [v_s] \equiv 1$ and, consequently, $[v_r]$ is generally less than unity. Similarly, the spread of the incident beam, $[\Delta S_i]$, for both argon and helium is less than 0.1, as compared to that of a Maxwellian beam for which, of course, $[\Delta S_s] \equiv 1$. Thus, it is not surprising that the data consistently exhibits $[\Delta S_r] < 1$. The value $[\Delta S_r] = 0.4$, for example, implies that the speed distribution has a relative width (say the halfwidth divided by

the mean speed) that is approximately 0.4 times the equivalent relative width for a Maxwellian speed distribution.

As a concluding point, the quantity $[\Delta S_r]$ may be viewed as an index of the "speed-coherence" of the scattering process where a fully "speed-coherent" scattering process is defined here as one for which $[\Delta S_r] = [\Delta S_i]$.

5.1.3 Intensity Distributions

Some conceptual appreciation of the significance of the various intensity distributions studied can be gained by considering the two limiting patterns between which most real gas scattering intensity distributions fall. The first of these, called a perfectly diffuse pattern (see Figure 5.1.1a), is characterized by a cosine distribution of intensity with respect to angle from the target normal. This pattern commonly occurs when an incident beam comes to full thermal equilibrium with the surface, via adsorption, and is then reemitted. It can occur, however, even in the limit of elastic collisions with the surface, if the surface is suitably rough. The other limiting pattern, called specular, is that for

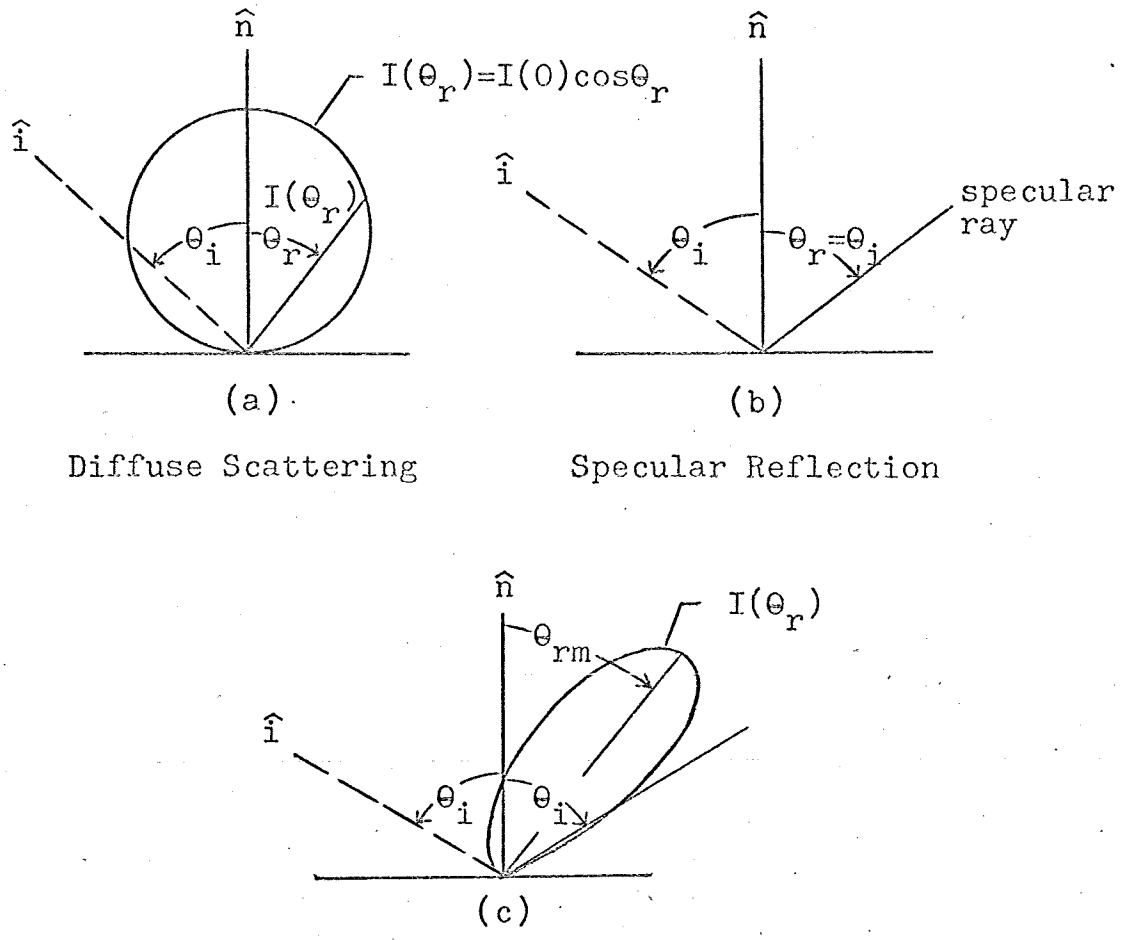

Figure 5.1.1 Basic Intensity Distribution Patterns for Scattering in the Principal Plane

optical-like reflection of the incident molecules from the nominal surface plane (see Figure 5.1.1b). Almost by necessity, specular scattering is accompanied by elastic collisions with the surface.

Many actual scattering distributions tend to be lobular, as with near-specular scattering, yet with maxima occurring not necessarily at the specular angle, $\theta_r = \theta_i$ (see Figure 5.1.1c). Indeed, lest $\theta_r = \theta_i$ be taken as a limit of the lobe's position, it should be noted that, depending upon the relative natures and energies of the scattering surface and incident beam, it is possible for the lobe maximum to occur at either $\theta_{rm} > \theta_i$ ("supraspecular" scattering) or $\theta_{rm} < \theta_i$ ("subspecular" scattering). For the present experiments, however, where $T_o \leq T_s$, θ_i will, in fact, provide such an upper bound on θ_{rm}, i.e., $0 \leq \theta_{rm} \leq \theta_i$. Indeed, the ratio of incident-molecule to surface-atom energy is the predominant factor in determining the position of the lobe here.

As it was instructive to discuss speed spreads in conjunction with mean speeds when considering energy transfer, so is it also enlightening to augment the discussion of intensity maxima with a measure of the angular range within which a specified portion of the lobular flux is contained. For the present study, the angular width of the scattered lobe in the principal

plane at the point of half-maximum intensity is selected as the desirable measure. Call this width $\Delta\theta_r$. The ratio of the maximum normalized intensity, $[I_{rm}]$, to the quantity, $\Delta\theta_r$ (degrees)/120°, will be defined as the Shape Factor, SF, of the measured intensity distribution, i.e.

$$SF = \frac{[I_{rm}]}{\Delta\theta_r/120^\circ} \qquad (5.1.3.1)$$

The factor 120° yields the convenient result, when used in conjunction with the previously chosen normalization of intensities to their maximum value for perfectly diffuse scattering, that SF = 1 in this limit. Analagously, SF would have the same value as its counterpart for the incident beam in the case of perfectly specular scattering.

The term "angular coherence" will be applied to the description of the intensity distributions of the scattered beams in a manner comparable to the application of speed-coherence to their speed distributions. Scattering will be termed "angle-coherent" if the SF for the reflected lobe is the same as that for the incident beam. For incident helium beams, $SF \approx 3 \times 10^4$. There will be no application of the SF criterion to argon data due to the fact that the large component of intensity at the surface

normal effectively assures that SF is always near unity for the argon beams.

In the present data , the dependence of SF upon surface roughness, alluded to previously in the discussion of sources of diffuse scattering, provides an interesting indicator of surface condition during the course of the experiment. Indeed, the surface was found to have experienced three distinct phases of surface roughness as determined by observed values of SF. Since SF is highly dependent upon the incident angle and noticeably dependent upon the surface temperature, these phases are defined relative to the fixed conditions $\theta_i = 70^o$, $T_S = 600^oK$. The phases are:

Phase I: This phase extended through the first thirty hours after initial deposition and is characterized here by SF $\geq$ 210. A comparison of Figure 5.2.1 with the analagous data recorded by Saltsburg and Smith [3] reveals that the SF for their beams during deposition exceeds 210 by several times, i.e. that scattering during and just after deposition is several times more angle-coherent than that ever observed here. Romney [5] has further demonstrated that the maximum scattered intensity of helium nozzle beams at $T_o = 300^oK$ on (111) silver ($\theta_i = 50^o$, $T_S \approx 600^o$) diminishes by a factor of three or

more during the first several hours immediately after deposition. The rate of decay is noticeably diminished after about the first three hours. Taking all of these results into account, it is concluded that SF for Phase I ranges over an extensive set of values bounded with a lower limit of ~ 210.

Phase II: This phase pertains to the same surface after 5 days of "vacuum-aging" at $T_S = 300^{\circ}K$ at a pressure near 10^{-2} torr. Over a period of observation of 130 hours, SF remained at approximately 160, indicating excellent stability. Further, the fact that SF was not altered by the aforementioned attempt at redeposition which resulted in the growth of a polycrystalline region indicates that this region did not significantly affect the overall scattering.

Phase III: Upon completion of all planned experiments, an attempt was made to desorb and record surface contaminants via rapid surface heating. This rapid heating of the surface to $\sim 800^{\circ}K$ resulted in thermal roughening of the surface such that all subsequent data displayed SF < 30. Such data will be said to pertain to a Phase III surface.

5.1.4 Data Format

The data will be presented in the form of individual plots of the properties $[I_r]$, $[v_r]$, and $[\Delta S_r]$ versus one or another of the independent experimental parameters θ_r, ϕ_r, τ, α, or T_s. Corresponding plots of $[I_r]$, $[v_r]$, and $[\Delta S_r]$ for the same scattered beam will be grouped under a common figure number and, where practical, common scales will be employed from figure to figure to facilitate comparison.

In any given figure, the pertinent parameters for the interaction data will be displayed in the following common array:

Figure Number	Gas	Source Temp.(^oK) / Surface	Surface Temp.(^oK)	Phase
θ_i (deg)	θ_r (deg)	τ(deg) α (deg)	SF	Elapsed time (hr)

For example, for Figure 5.2.1 the array reads:

Figure 5.2.1 Helium (300)/Ag (600) I

θ_i	θ_r	τ	α	SF	ET
50		0	0	50	2.1 - 6.0

An empty position in the array indicates that the associated

parameter is either a variable or else is irrelevant to the data at hand.

5.2 Helium Data

For convenience the helium data presented are divided into three sections, one for each phase that the surface experienced. For all of the data recorded, the incident beam is at room temperature, i.e. $T_o \approx 300^oK$.

5.2.1 Phase I Data

The initial data recorded were intended to explore the scattered flux in the principal plane and in selected transverse planes under the representative conditions: $\theta_i = 50^o$, $T_s = 600^oK$, $T_o = 300^oK$. These conditions were selected primarily due to the availability of similarly constrained data in the work of Saltsburg and Smith [3], [23] and of Bishara [20]. The distributions of $[I_r]$, $[v_r]$, and $[\Delta S_r]$ were studied as functions of the angles θ_r and ϕ_r, in their respective planes, and also as functions of τ and α.

To begin the presentation of the data, Figure 5.2.1

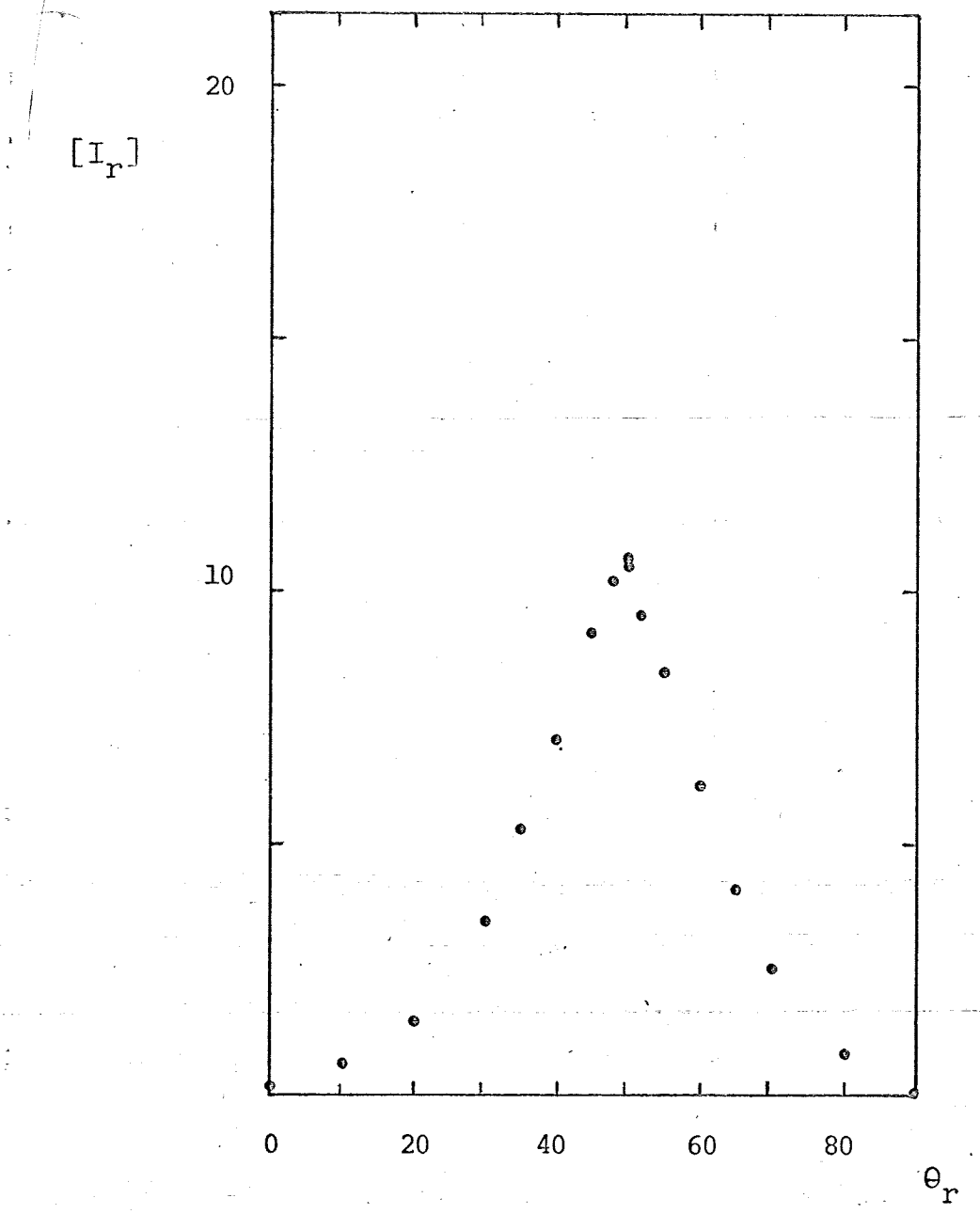

Figure 5.2.1 Helium(300)/Ag(600) I

θ_i	θ_r	τ	α	SF	ET
50		0	0	50	2.1-6.0

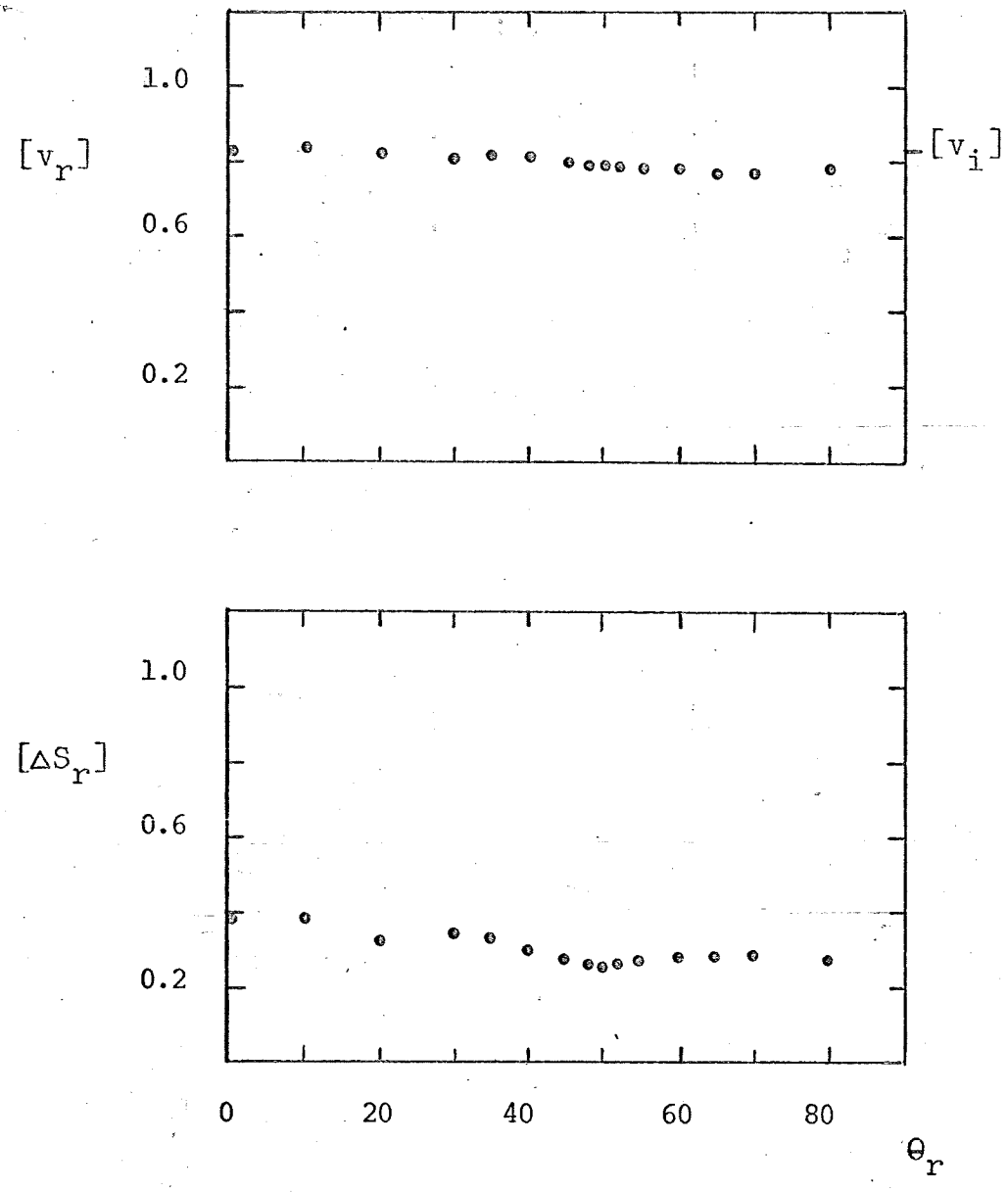

Figure 5.2.1

displays the distributions of the intensity, mean speed, and speed spread in the principal plane. Figure 5.2.2 displays the analagous data for the three representative transverse planes for which $\theta_r = 40^\circ$, 50°, and 60°, respectively. Together, the data in these two figures constitute a reasonably complete three-dimensional mapping of the quasi-specular intensity lobe exhibited in this case.

Inspection of these figures reveals that the scattered intensity is strongly oriented toward the specular in the principal plane and toward the principal plane in each of the transverse planes shown. A cross-section of the scattered lobe normal to the direction $\theta_r = \theta_i$ taken at the point of half-maximum intensity is found to be roughly elliptical, having its major axis in the principal plane and a length ratio between that axis and the transversely oriented minor axis of approximately 1.3:1. As noted in Figure 5.2.1, SF $\approx$ 50 for this beam.

Comparison of the principal plane intensity distribution obtained here with those shown in Figure 2 of Saltsburg and Smith [3] indicates that the behavior of the present surface is somewhere between those of the "fresh" and "vacuum aged" targets discussed in that reference (the aging process therein described consisting

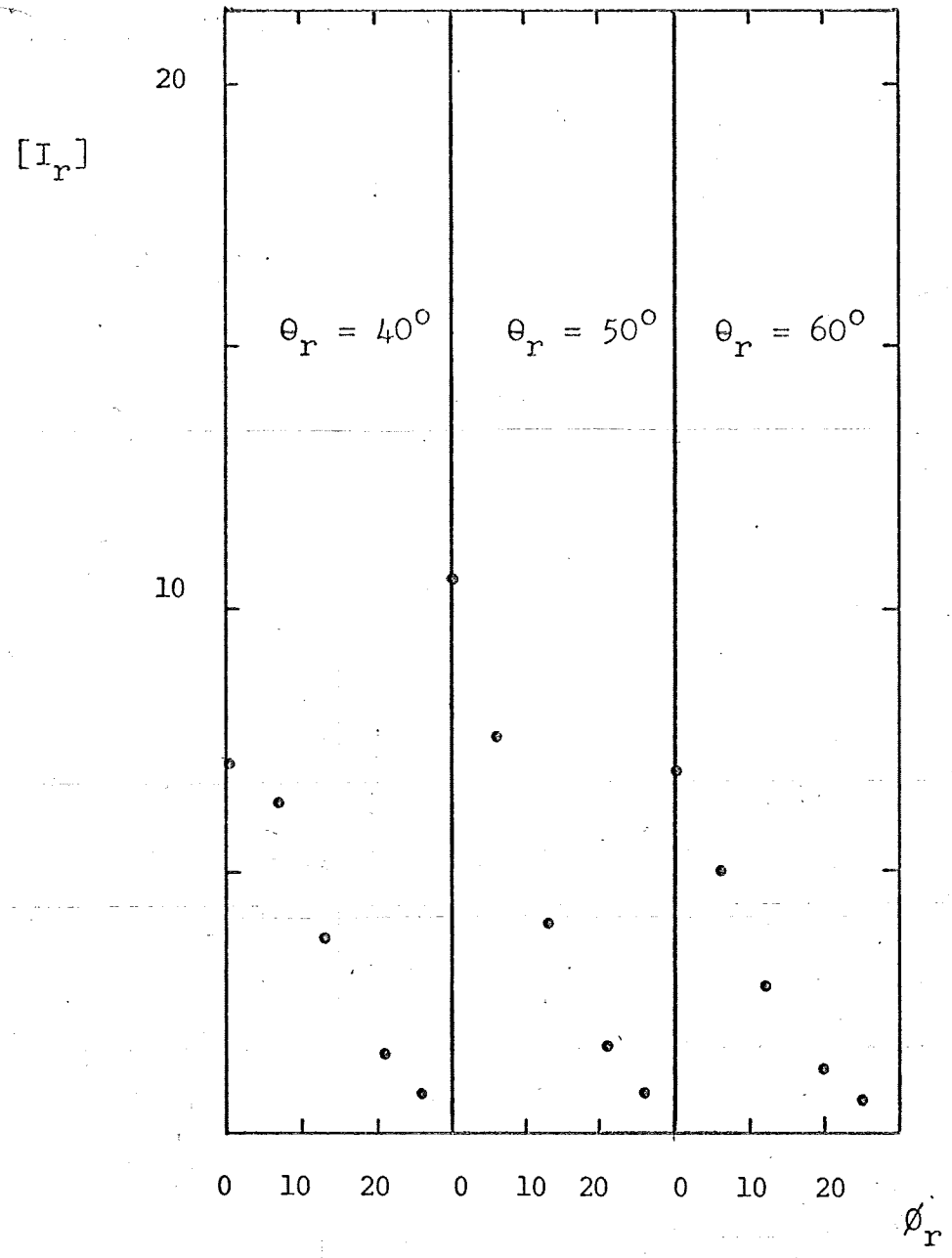

Figure 5.2.2 Helium(300)/Ag(600) I

θ_i	θ_r	τ	α	SF	ET
50					8.0-9.2

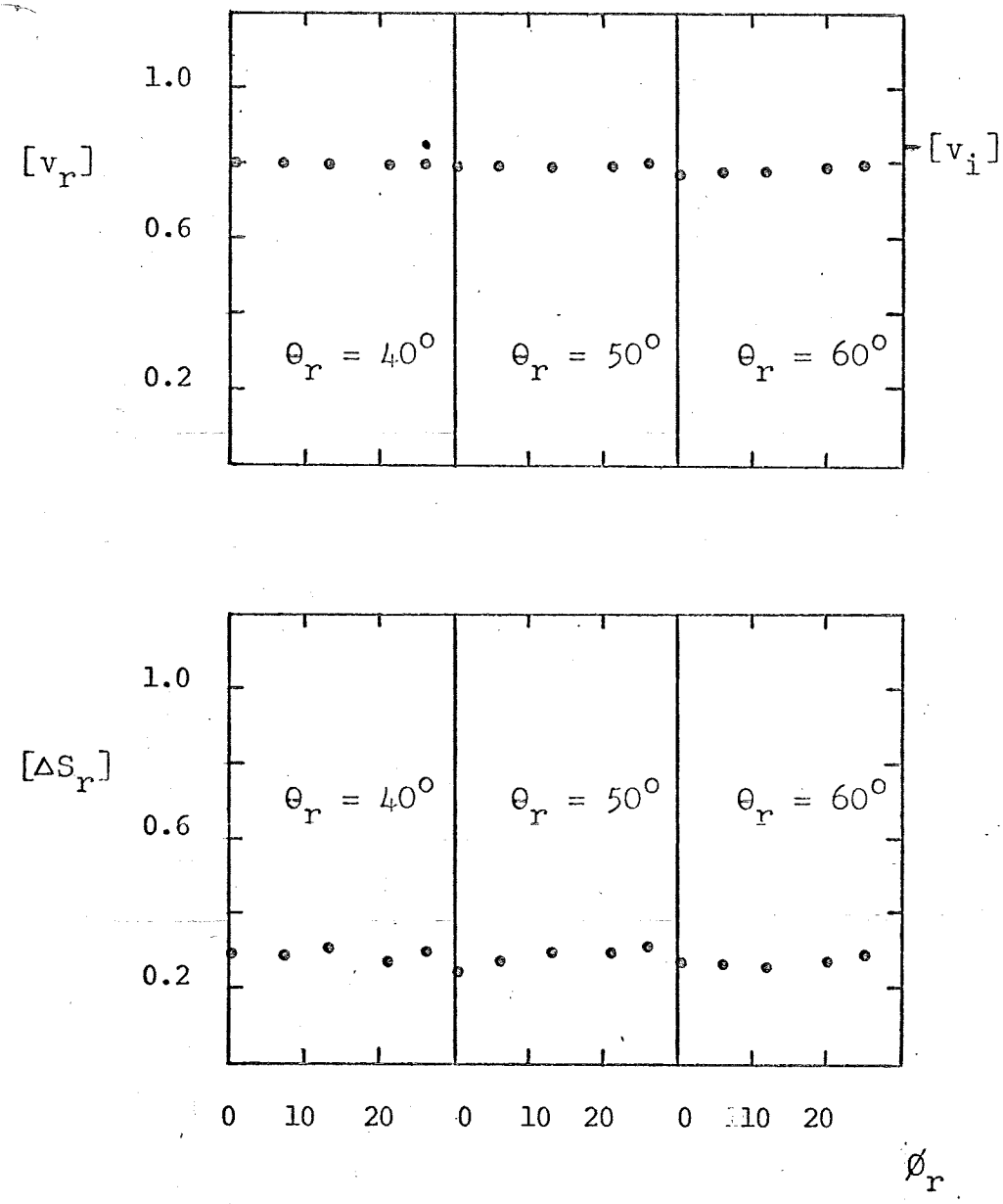
1.0
0.6
0.2
$[v_r]$
$[v_i]$
$\theta_r = 40^o$
$\theta_r = 50^o$
$\theta_r = 60^o$
$[\Delta S_r]$
0 10 20 0 10 20 0 10 20
ϕ_r

Figure 5.2.2

of 15 hr. at $T_s \approx 300^{\circ}K$ in a vacuum of 100 μ followed by 5 hr. at $560^{\circ}K$ in a vacuum of 5×10^{-7} torr). While some three hours of aging at $600^{\circ}K$ in a vacuum of 5×10^{-7} torr preceded the data in Figures 5.2.1 and 5.2.2, it is believed that the relatively broadened peaks of the present data can be more accurately attributed to the fact that the target crystal was grown near the upper temperature limit for epitaxy and consequently experienced a higher degree of three-dimensional crystal growth at the surface. Note that the speed spread data in the second part of Figure 5.2.1 displays a slight minimum at $\theta_r = \theta_i$ in both the principal and related transverse ($\theta_r = 50^{\circ}$) planes. This behavior proves consistent throughout the remaining data for helium on heated silver and indicates that the collisions tend to be more "speed-coherent" for those gas atoms scattered in the specular direction than for those scattered in other directions, particularly those scattered at angles $\theta_r < \theta_i$. Note also that $0.25 \leq [\Delta S_r] \leq 0.4$ for the data in these figures. Such values of $[\Delta S_r]$ are typical of the surface in its Phase I condition.

To complement the information contained in the spread data relative to speed-coherency in the interactions, the data on mean speeds yield information concerning the magnitude and direction of energy and momentum exchange.

The points labeled $[v_i]$, located on the right hand side of each of the mean speed plots such as shown in the second part of Figure 5.2.1, indicate the appropriate normalized values of the mean speeds of the incident atoms for each case.

The data generally display a tendency toward increasing mean speed for $\theta_r < \theta_i$ in the principal plane and little angular dependence in each of the studied transverse planes.

The actual values plotted, it should be remembered, are systematically low by from 4% to 7% (as mentioned in the treatment of errors). This systematic error explains why $[v_r] < [v_i]$ at $\theta_r = \theta_i$ instead of $[v_r] \approx [v_i]$ as one would expect.

The stability of $[I_r]$, $[v_r]$, and $[\Delta S_r]$ with respect to variation of the azimuthal angle, α , is displayed in Figure 5.2.3. The α -study detailed therein was undertaken to determine the extent to which the surface crystal's lattice orientation relative to the incident direction, $\hat{i}$, might affect the three scattering distributions of interest, especially that for $[I_r]$. Were diffraction effects observable, they would have appeared as cyclic variations in $[I_r]$ as a function of α (most probably at 60° intervals). As the figure indicates, however, all three plotted parameters are virtually independent of α within the degree

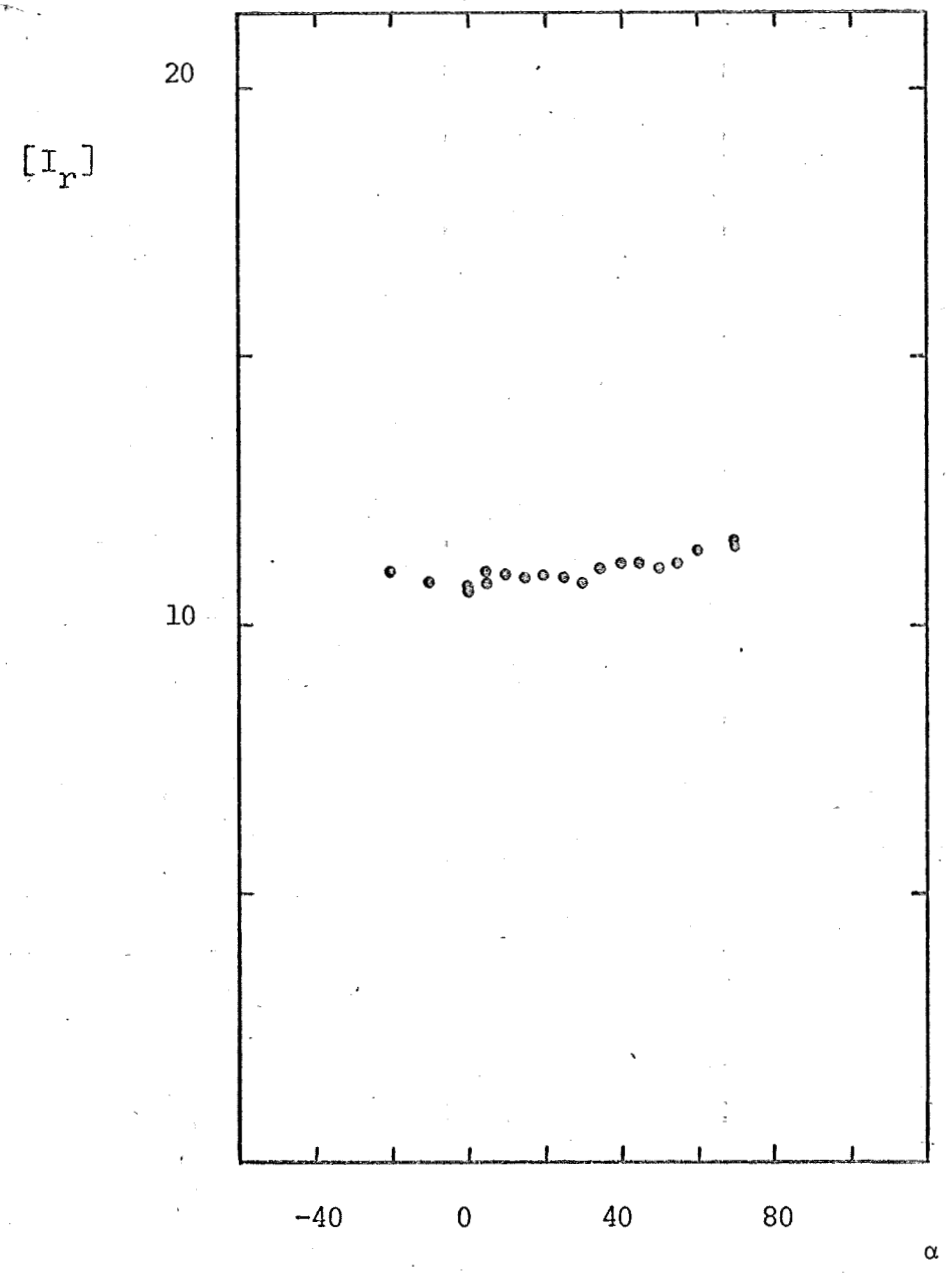

Figure 5.2.3 Helium(300)/Ag(600) I

θ_i	θ_r	τ	α	SF	ET
50	50	0			6.9-8.0

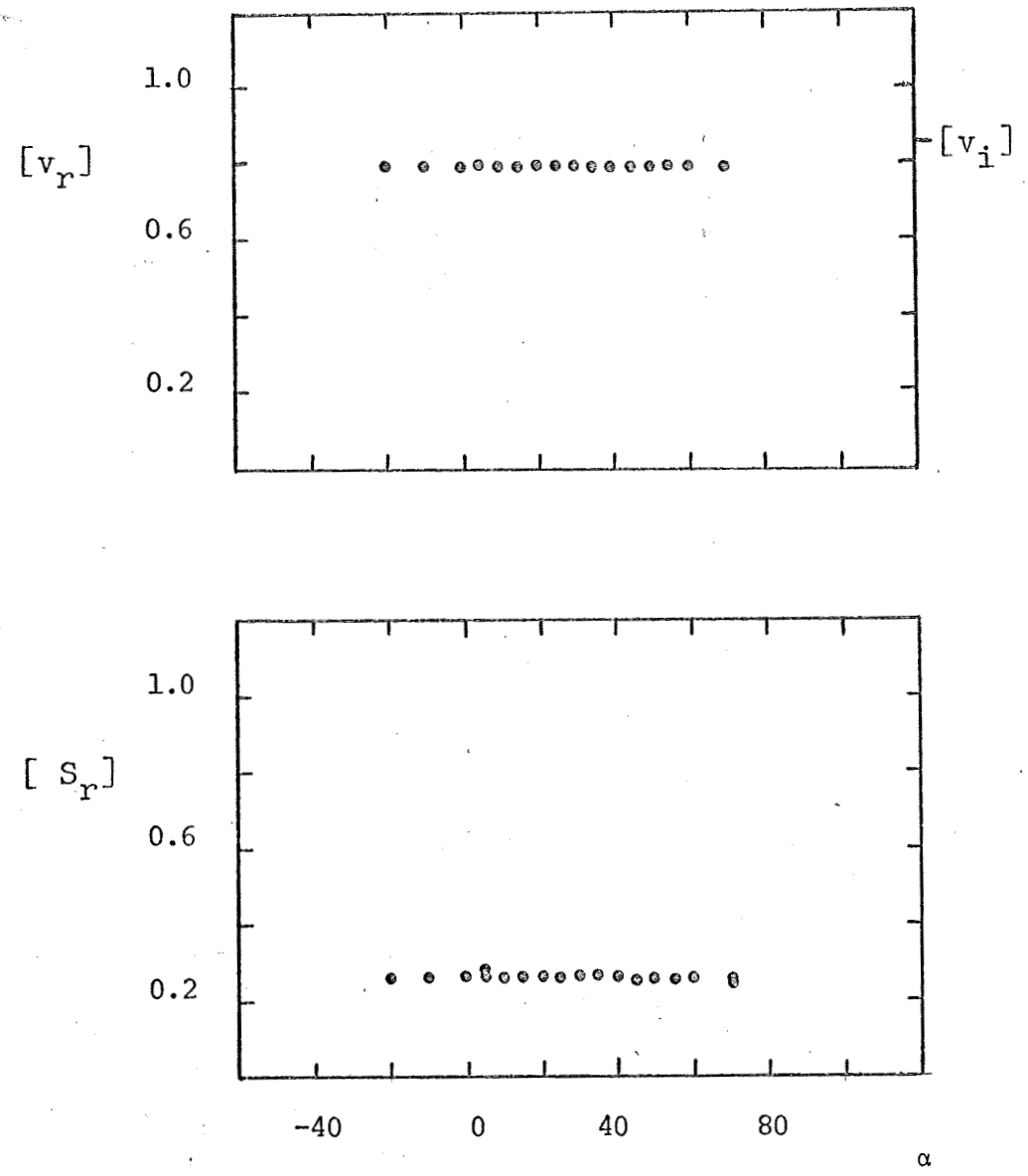

Figure 5.2.3

of accuracy of the experiment. The wobble in the α-axis is as likely a cause of the variations of $[I_r]$ with α as any in view of their order of magnitude and irregularity. This effect was discussed in Section 3.5.1.

The above demonstrated independence of the scattering upon crystal lattice orientation (i.e. of α) implies that symmetry should exist in the three plotted parameters with respect to variation of the target tilt angle, τ, about the principal plane. This symmetry is clearly displayed in Figure 5.2.4 where $\Theta_r \approx \Theta_i \approx 50^\circ$. ($\Theta_r$ and Θ_i, as strictly defined, vary slightly when τ is changed without appropriate compensation of other orientation parameters.) Little significant dependence of either $[v_r]$ or $[\Delta S_r]$ on τ is observed here. Such variation of $[\Delta S_r]$ with τ as is observed falls within the uncertainty of the data.

During the course of the experiment, studies were made to determine the effect of varying the resolution of the time-of-flight measurement system upon the data; the efficacy of the mathematical corrections for low resolution built into the data-reduction program was of particular interest. Figures 5.2.5 and 5.2.6, the former taken at greater resolution, display a gratifying independence of the helium data upon this resolution. (Low resolution is not a problem with argon.)

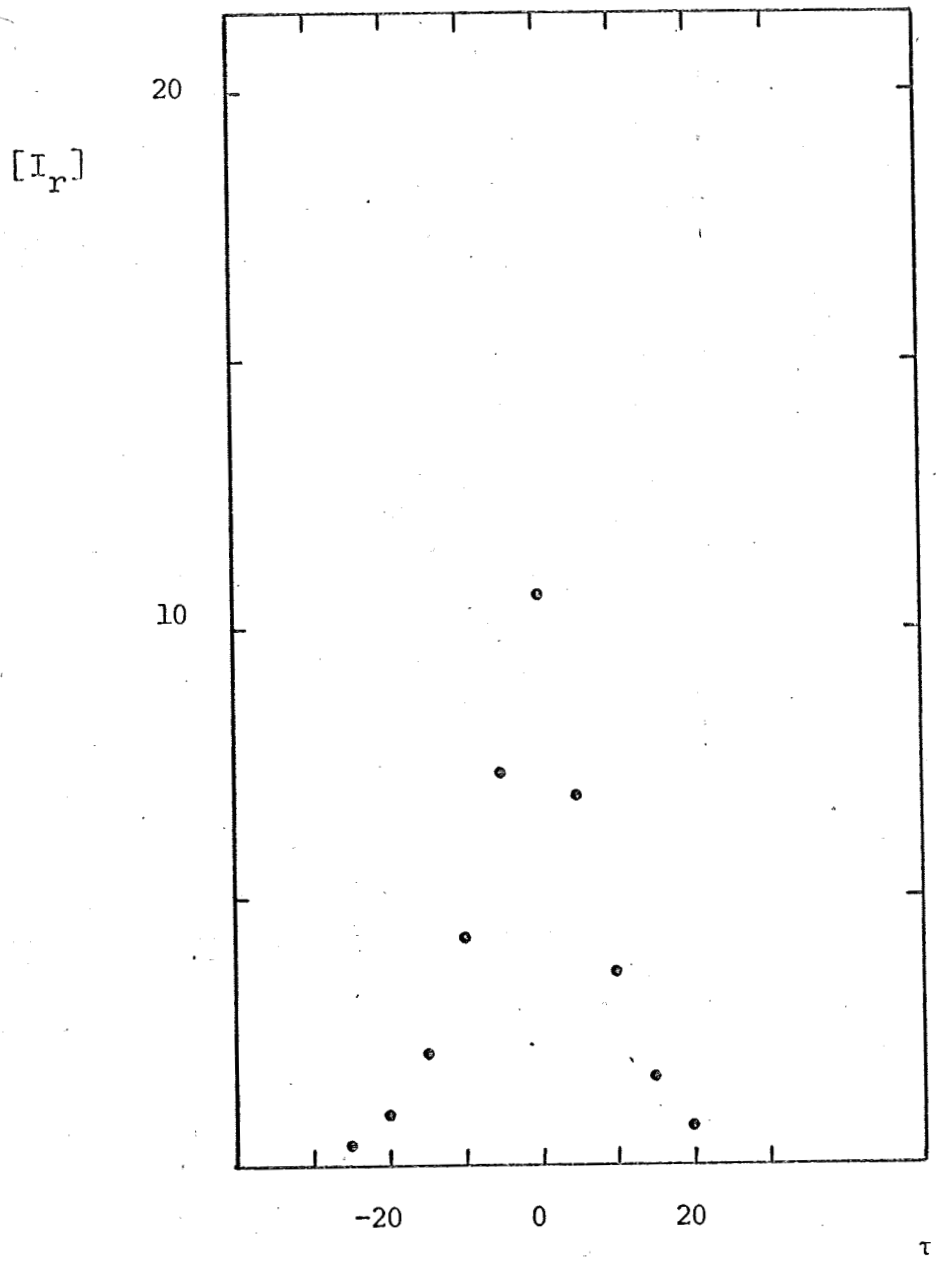

Figure 5.2.4. Helium(300)/Ag(600) I

θ_i	θ_r	τ	α	SF	ET
50			0		6.0-6.9

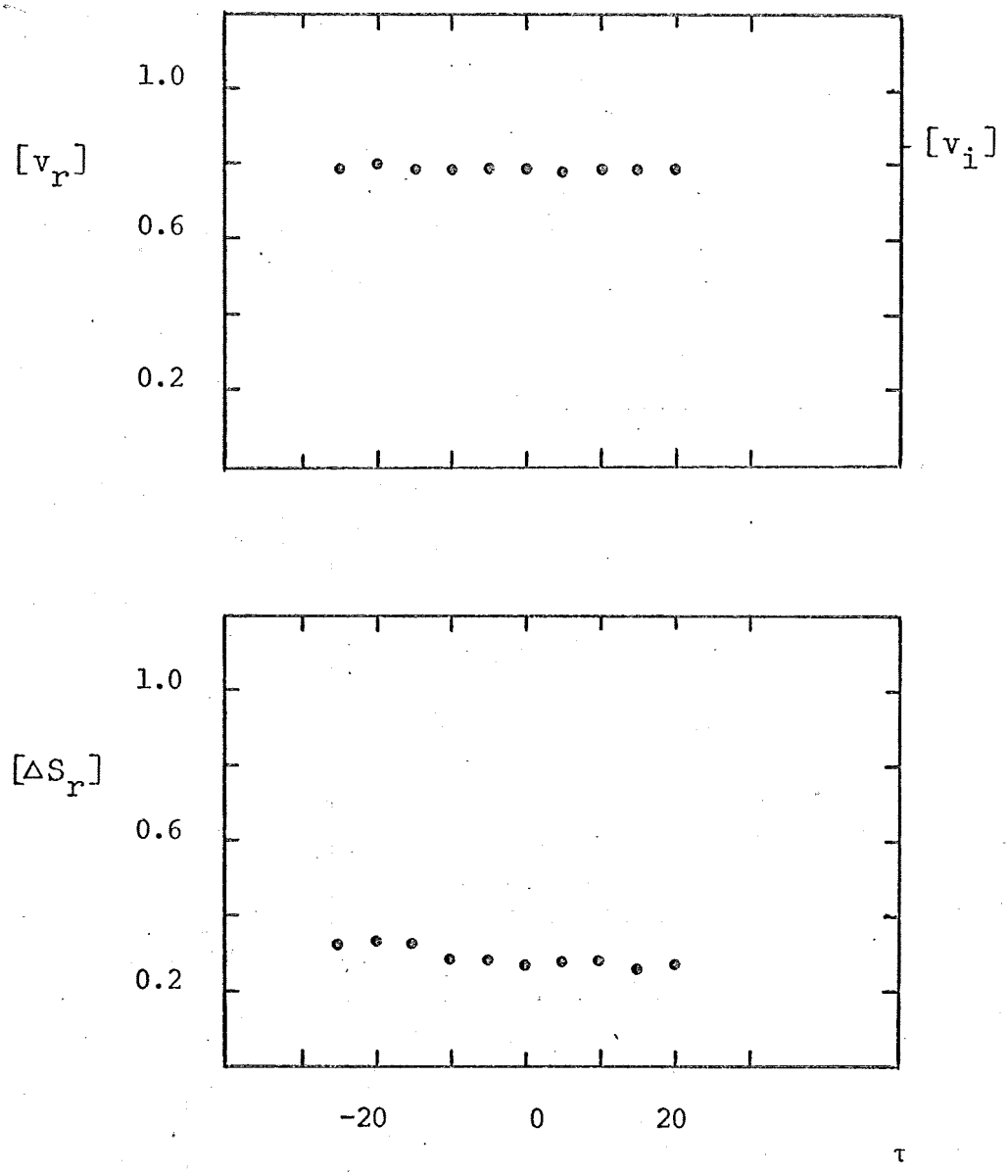

Figure 5.2.4

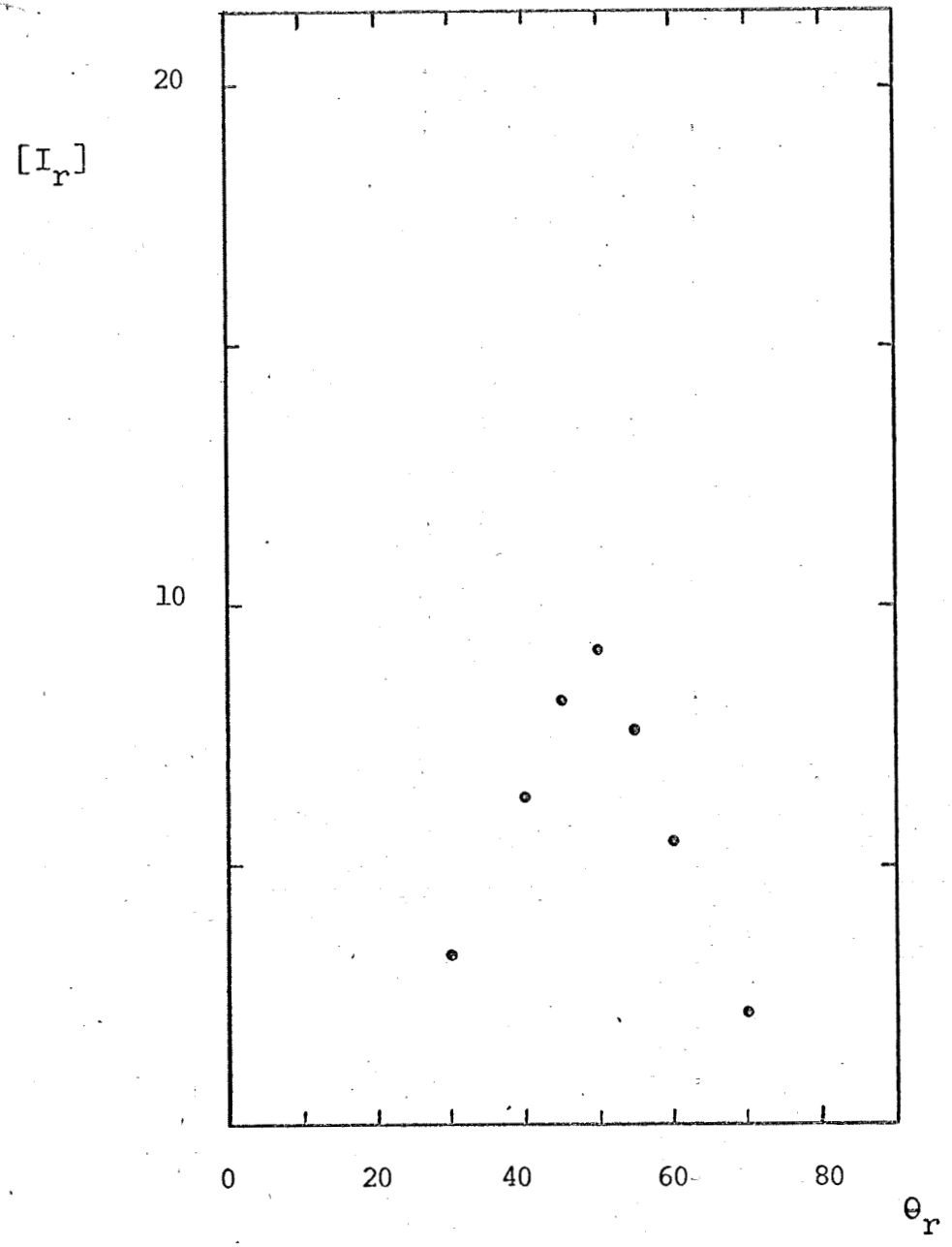

Figure 5.2.5 Helium(300)/Ag(600) I

Θ_i	Θ_r	τ	α	SF	ET
50		0	0	40	27.0-27.5

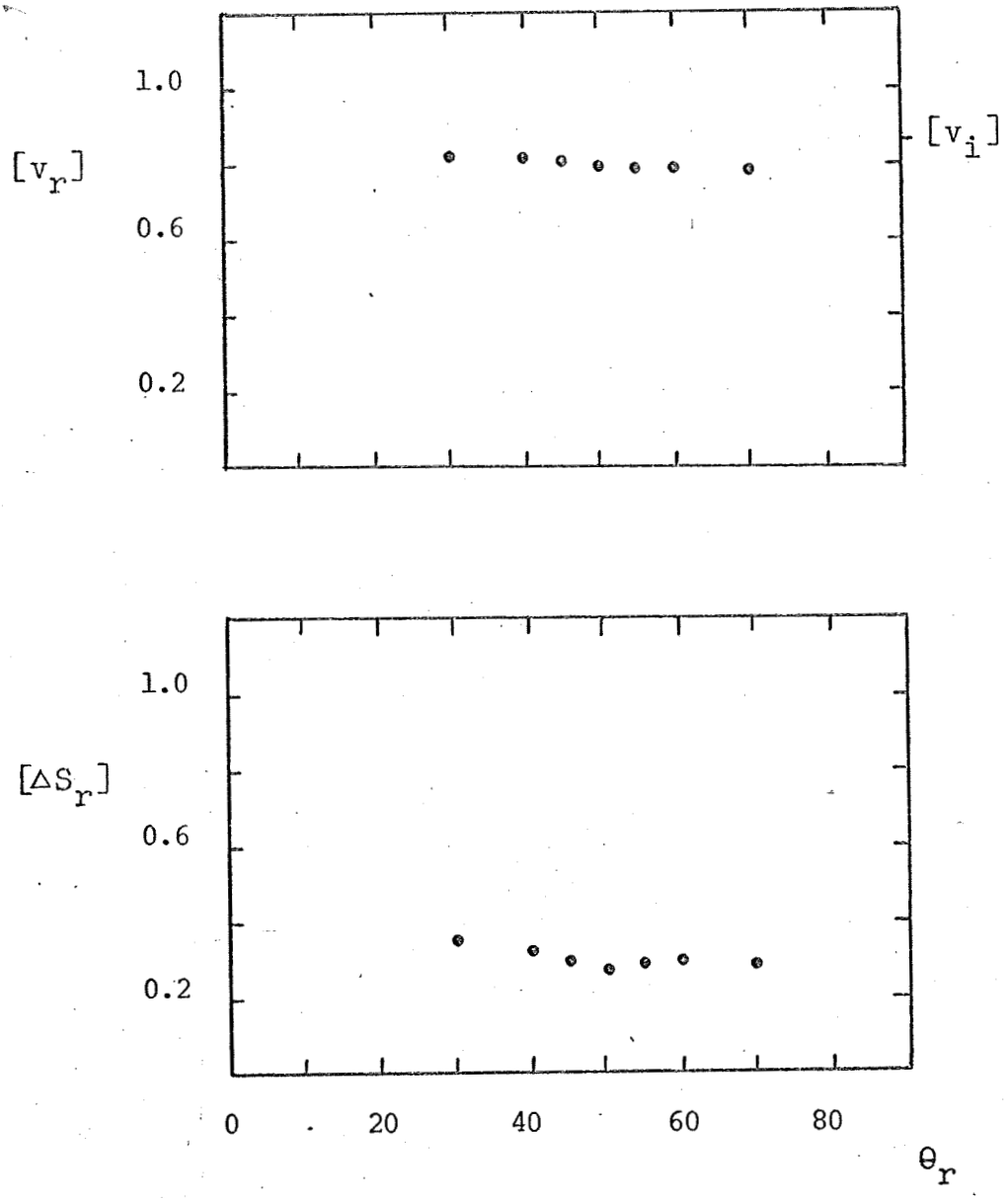

Figure 5.2.5

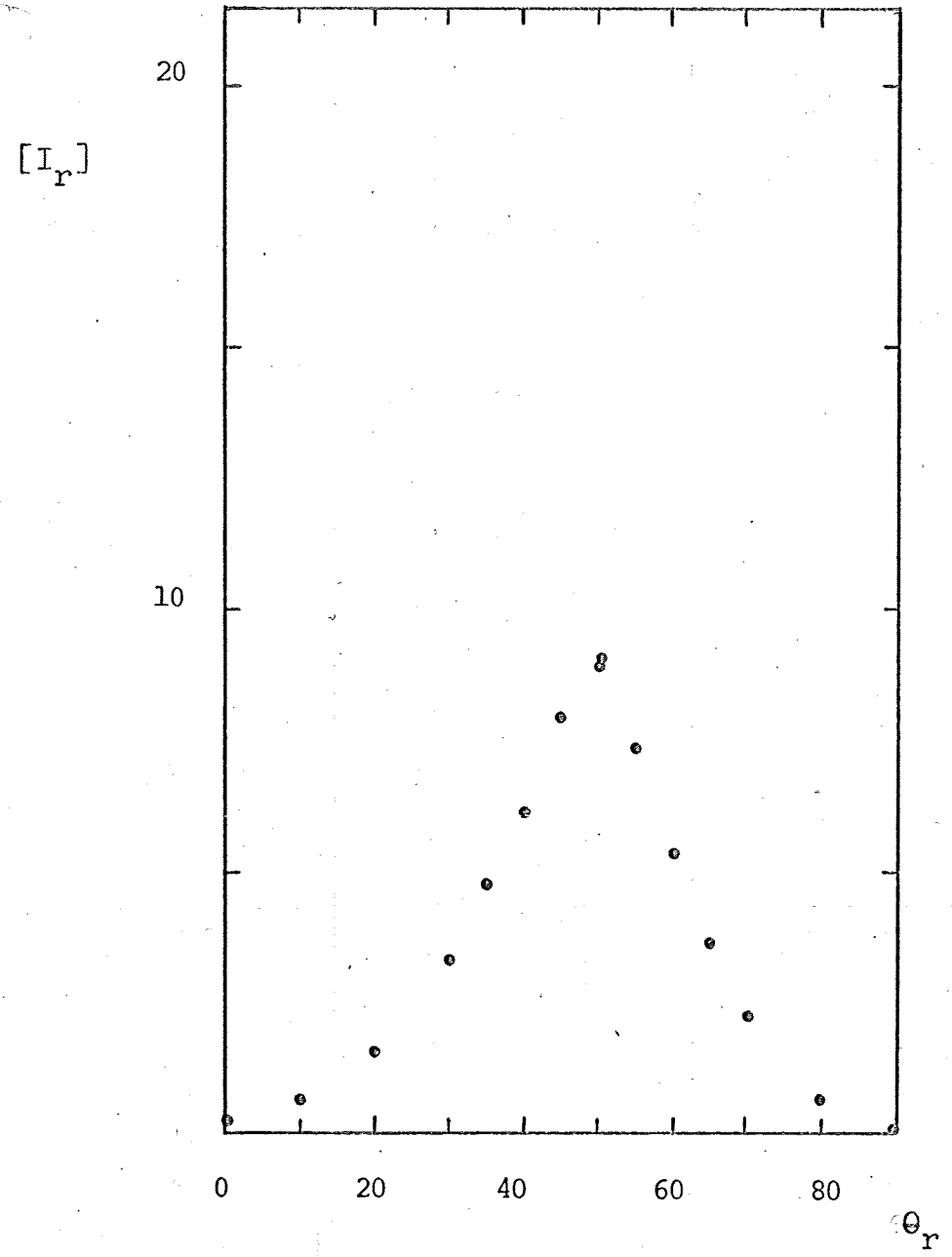

Figure 5.2.6 Helium(300)/Ag(600) I

Θ_i	Θ_r	τ	α	SF	ET
50		0	0	40	24.0-27.0

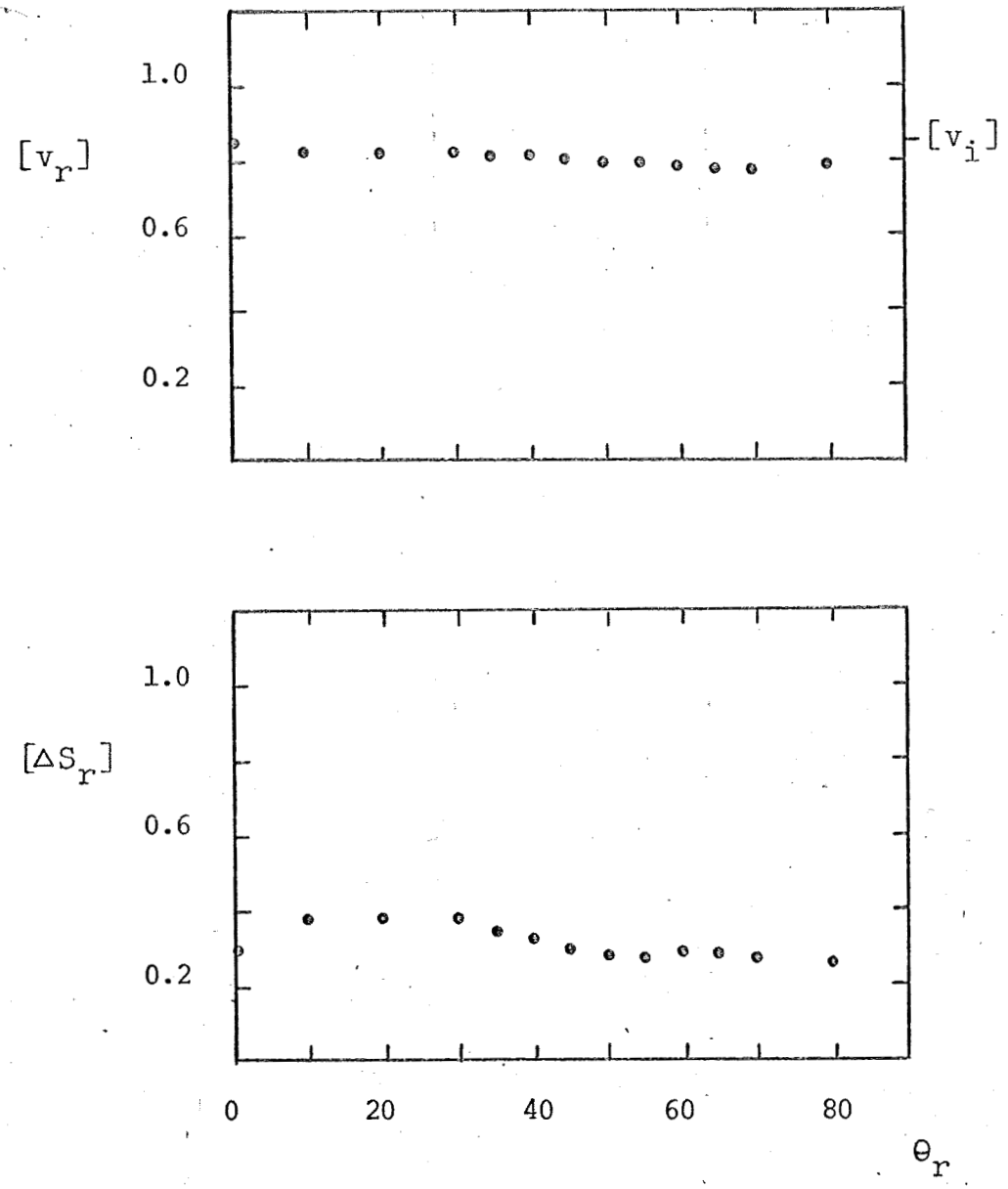

Figure 5.2.6

Figures 5.2.6 - 5.2.8 show the effect of varying the incident angle on scattering in the principal plane. It is observed in these figures that in general the intensity at the specular angle increases with increasing θ_i through the range $30^\circ \leq \theta_i \leq 70^\circ$ while the speed-spread decreases with increasing θ_i and the mean speed displays apparent independence of changes in θ_i. The trends displayed in Figures 5.2.6 through 5.2.8 for $[I_r]$, $[v_r]$, and $[\Delta S_r]$ as functions of θ_r, save for the change in the location of the specular angle, are essentially the same as those described in the discussion of Figure 5.2.1. It is noteworthy, however, that as θ_i increases, the variations of $[I_r]$ and $[\Delta S_r]$ with changes in θ_r become more pronounced. Further, there is a strong dependence of SF upon the angle of incidence as is apparent in the tabulation below:

θ_i	SF
30°	25
50°	40
70°	210

Considered together, the trends outlined above indicate both increased speed-coherence and increased angle-coherence as θ_i approaches glancing incidence.

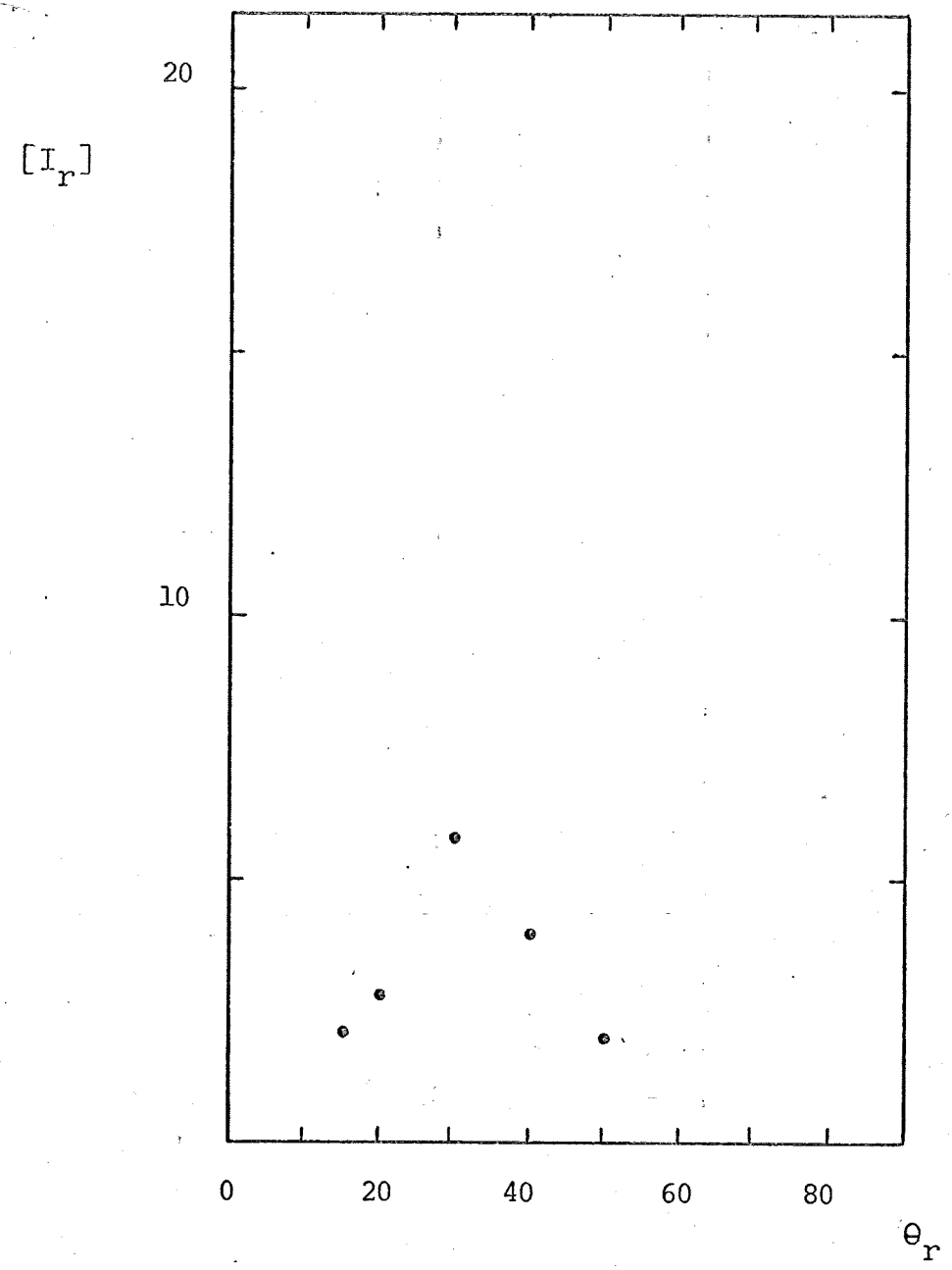

Figure 5.2.7 Helium(300)/Ag(600) I

θ_i	θ_r	τ	α	SF	ET
30		0	0	25	27.5-28.0

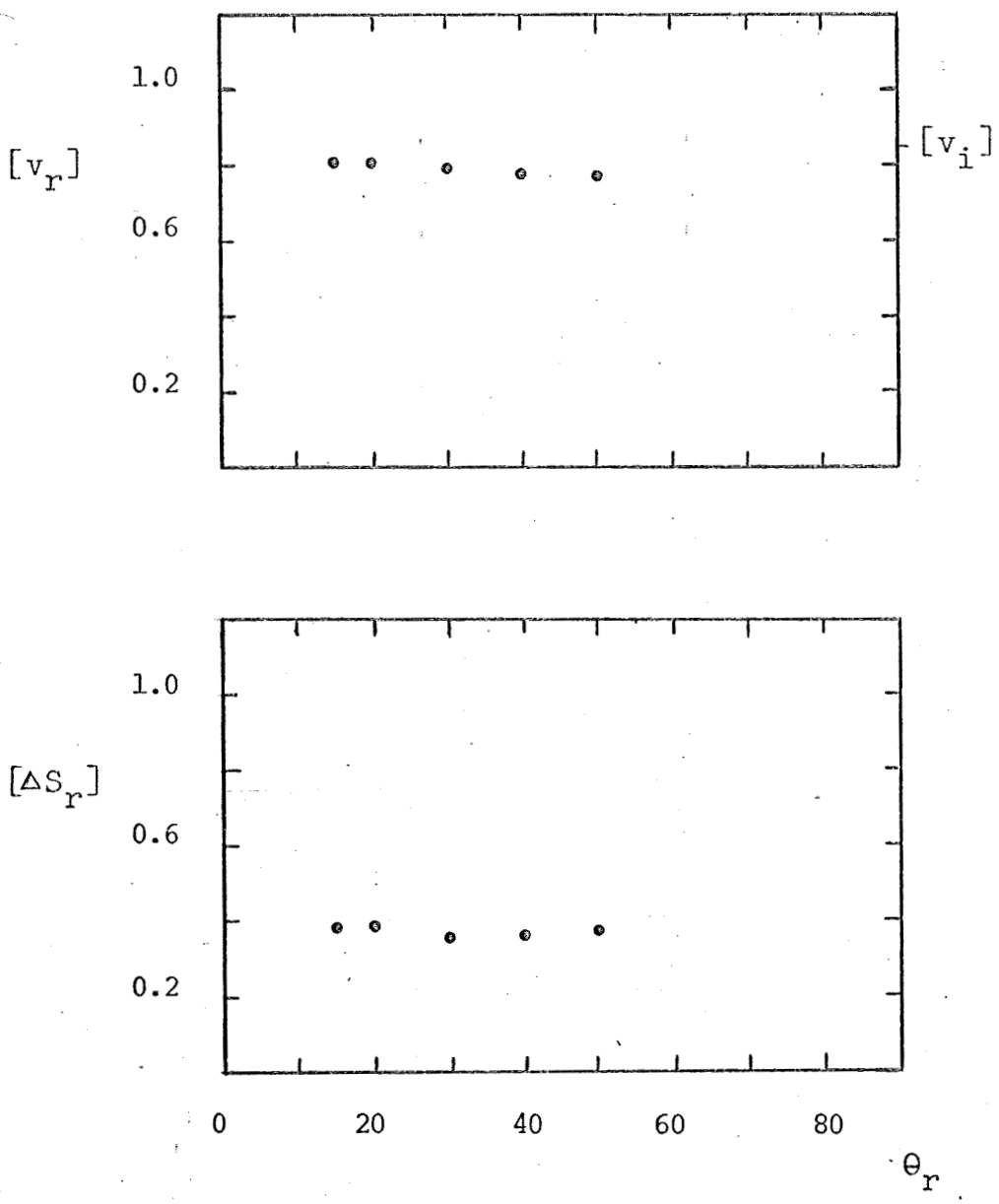

Figure 5.2.7

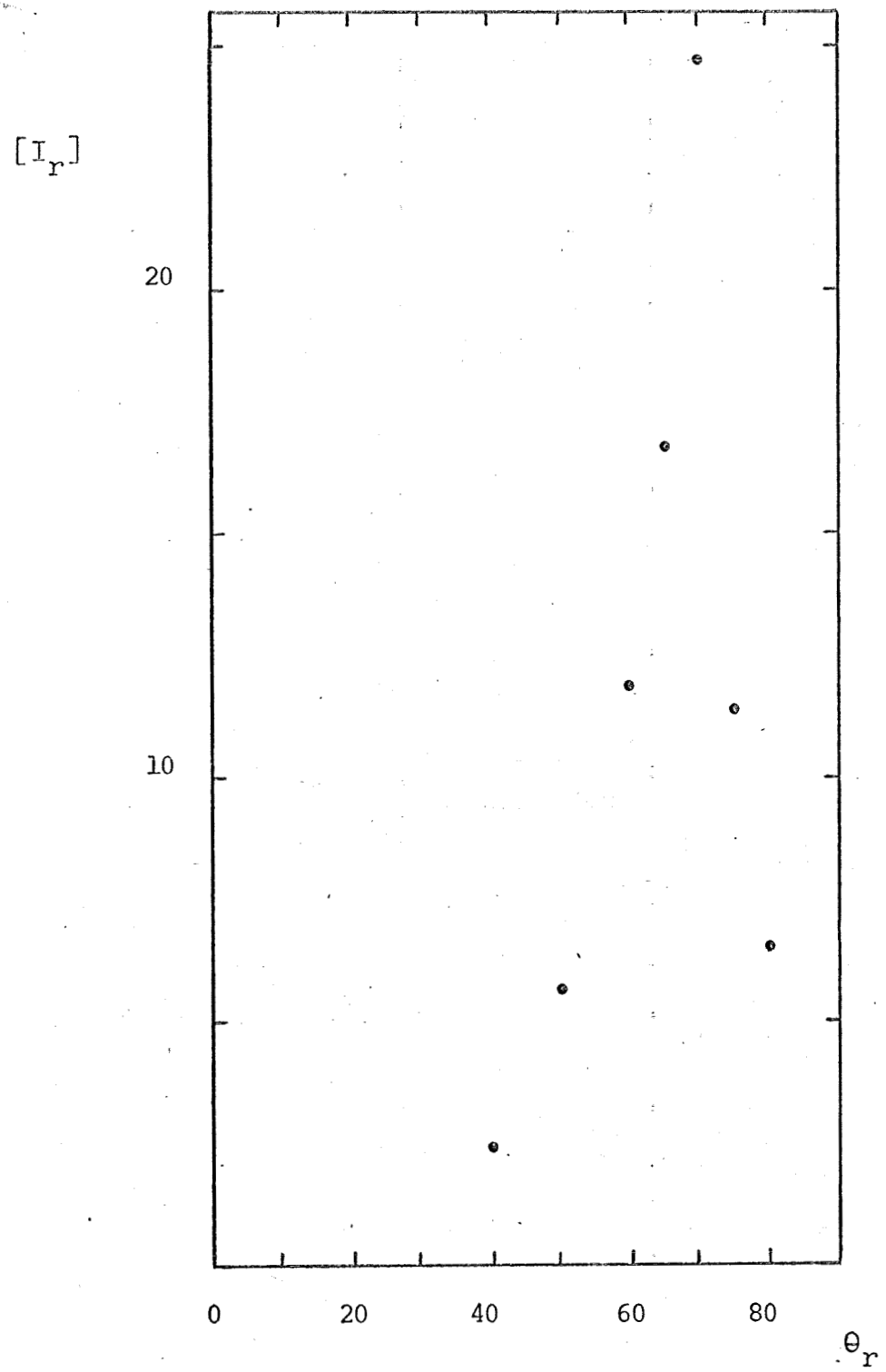

Figure 5.2.8 Helium(300)/Ag(600) I

θ_i	θ_r	τ	α	SF	ET
70		0	0	210	28.0-28.5

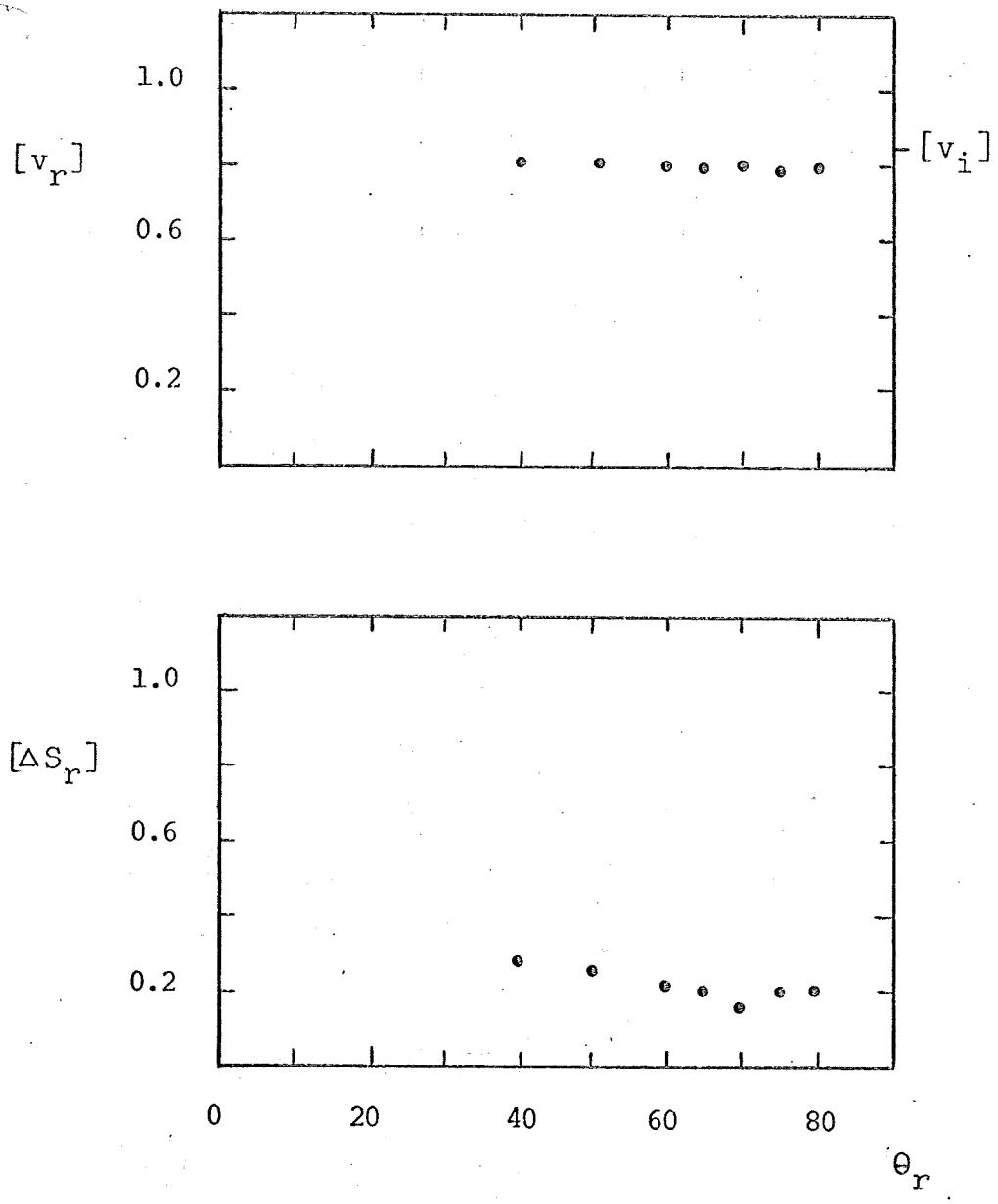

Figure 5.2.8

A further inquiry into the behavior of $[I_r]$, $[v_r]$, and $[\Delta S_r]$ at the specular over a wider range of incident angles was next pursued and the results obtained appear in Figure 5.2.9. The trends described above were faithfully reproduced in this study with the exception that $[I_{rm}]$ appeared to reverse its trend of increasing with θ_i in the range $70^\circ \leq \theta_i \leq 80^\circ$. This reversal, in all probability, is simply an indication that an important fraction of the incident beam does not strike the 1"-diameter target for $\theta_i > 70^\circ$.

5.2.2 Phase II Data

The effects of varying the surface temperature upon the behavior of the scattered flux and the time-dependence of these effects were also of interest. Figures 5.2.10 - 5.2.13 present data relevant to these effects for the case of the surface in its Phase II condition. These data were recorded in the principal plane for $\theta_i = 70^\circ$. The setting of α varies from figure to figure due to attempts at observing possible diffraction effects in principal plane data recorded at α -settings determined, on the basis of previous α -sweeps, as possibly effecting the proper alignment of surface crystallography and detector

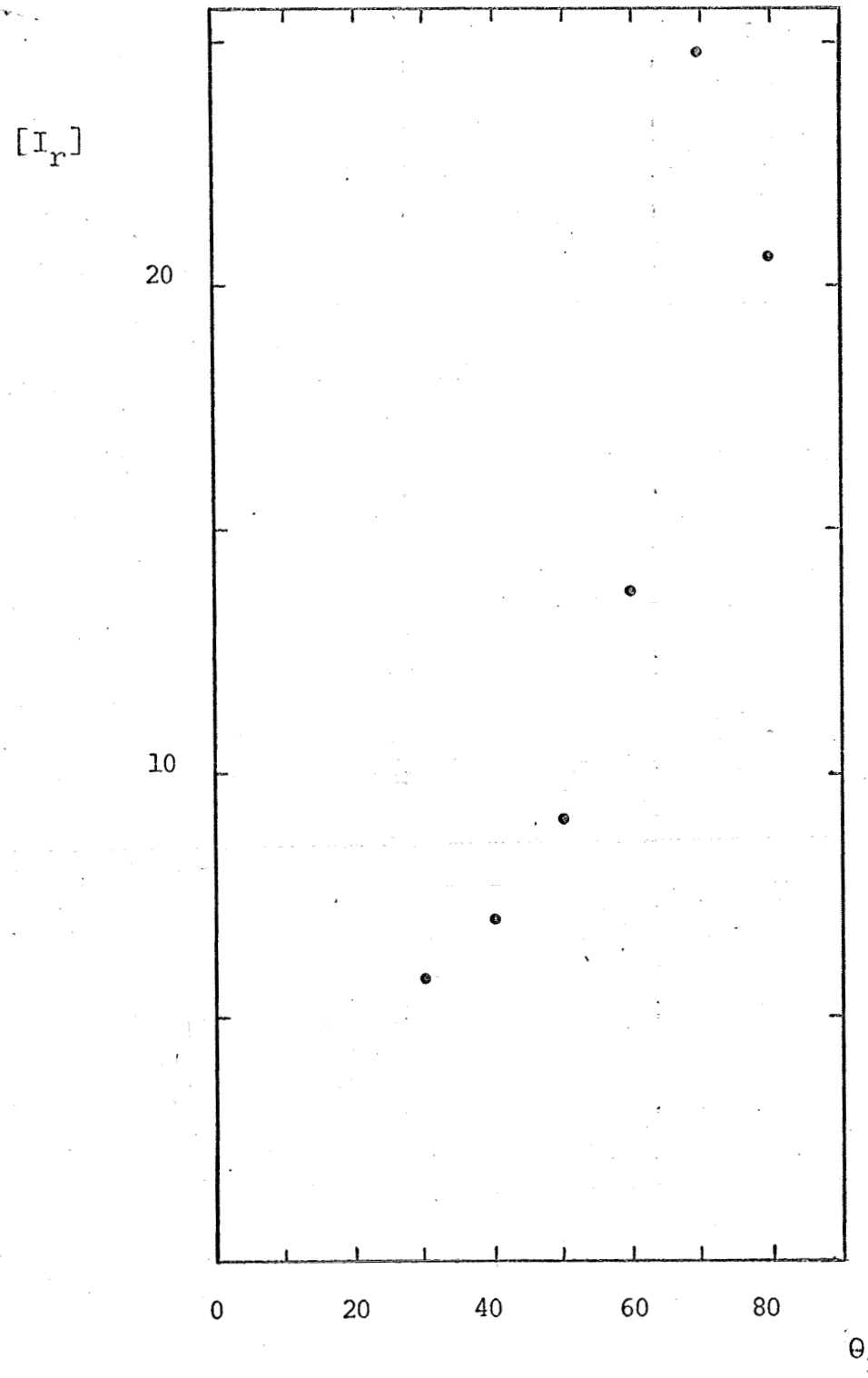

Figure 5.2.9 Helium(300)/Ag(600) I

θ_i	θ_r	τ	α	SF	ET
		0	0		24.0-28.8

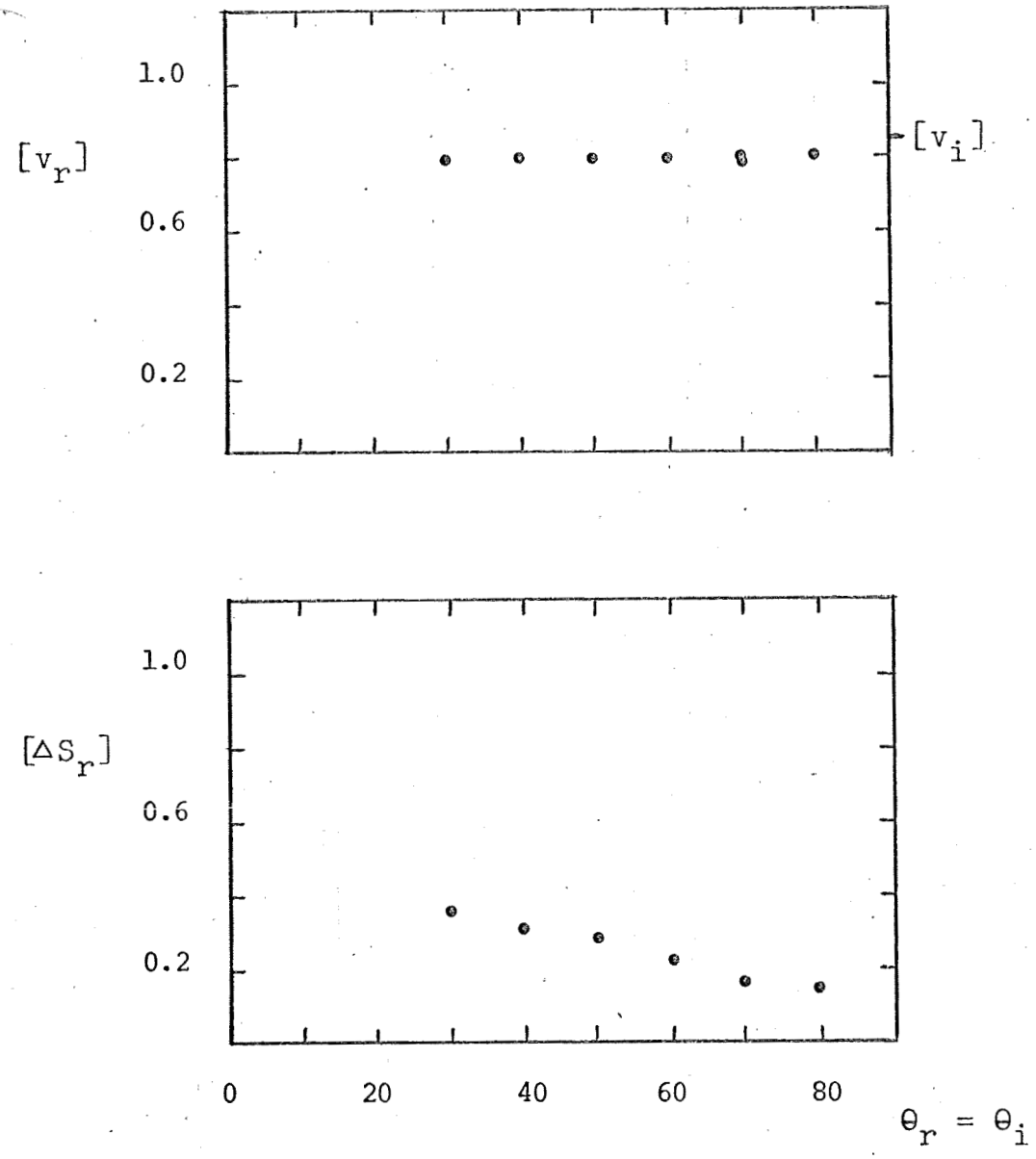

Figure 5.2.9

sweep plane. Since diffraction was not observed in the present study, the value of α is irrelevant to the discussion at hand.

That the flux distribution for this Phase II surface at $T_S = 300^{\circ}K$ was dominantly diffuse is evidenced by Figure 5.2.10. The intensity is as great at the normal as anywhere else in the principal plane and the speed-spread, quite uncharacteristically, has no minimum at the specular. This behavior strongly suggests that the scattering surface in this case is dominated by adsorbates from the background of the system. Even so, and most importantly, the facts a) that all values of $[\Delta S_r]$ are still small compared to unity, and b) that all values of $[v_r]$, even with their systematic deficiency, are greater than unity, are conclusive evidence that the interaction <u>is not</u> one primarily characterized by adsorption-reemission of the helium atoms.

Raising the surface temperature to $600^{\circ}K$ (see Figure 5.2.11) served to confirm the conclusion that surface adsorbates were dominating the interaction at $T_S = 300^{\circ}K$. Presumably due to the desorption of the majority of the physisorbed contaminants at this higher temperature, a distinctly quasi-specular lobe returns to the intensity distribution and both the mean velocity and the speed spread resume the values that they displayed

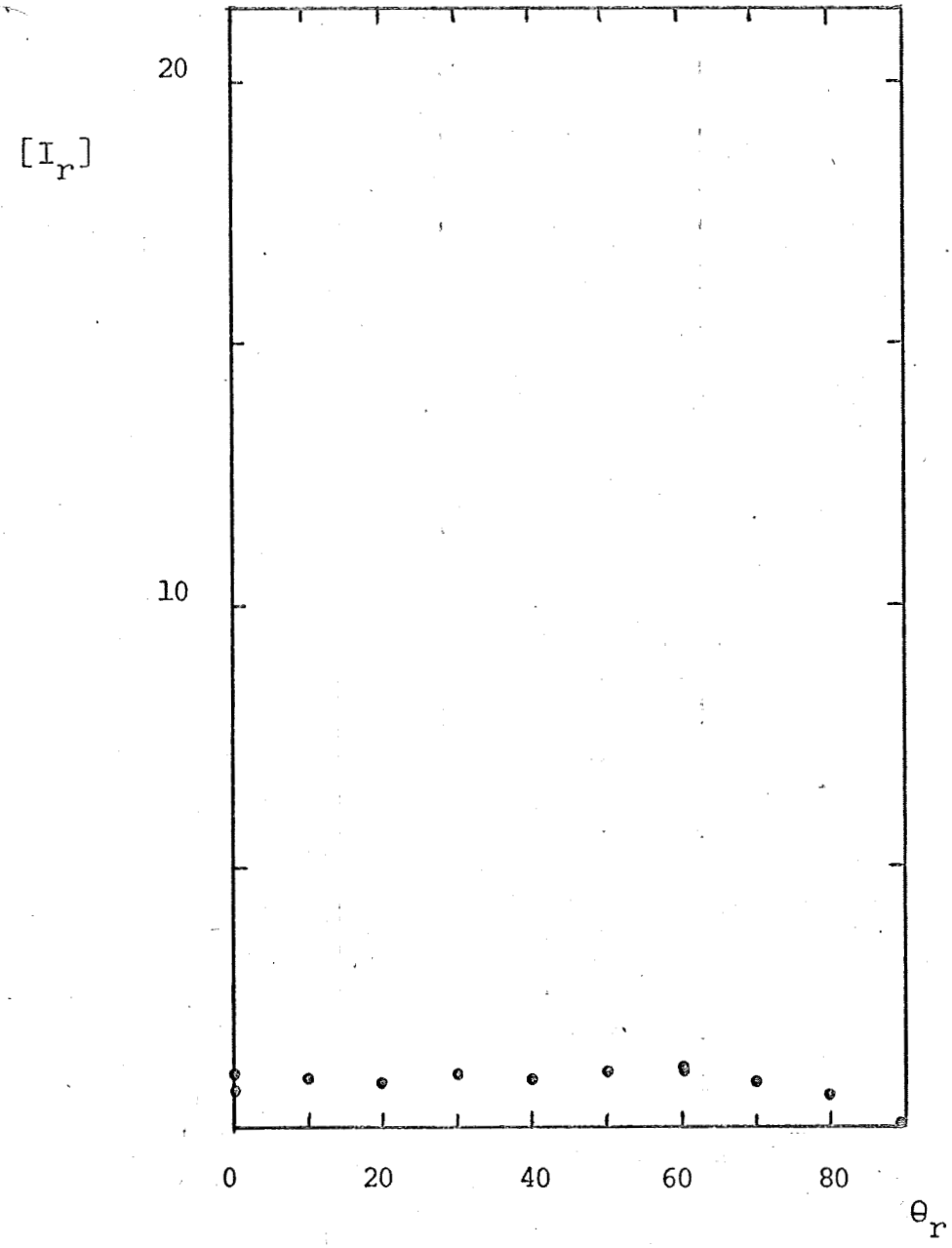

Figure 5.2.10 Helium(300)/Ag(300) II

θ_i	θ_r	τ	α	SF	ET
70		0	0		165.8-166.8

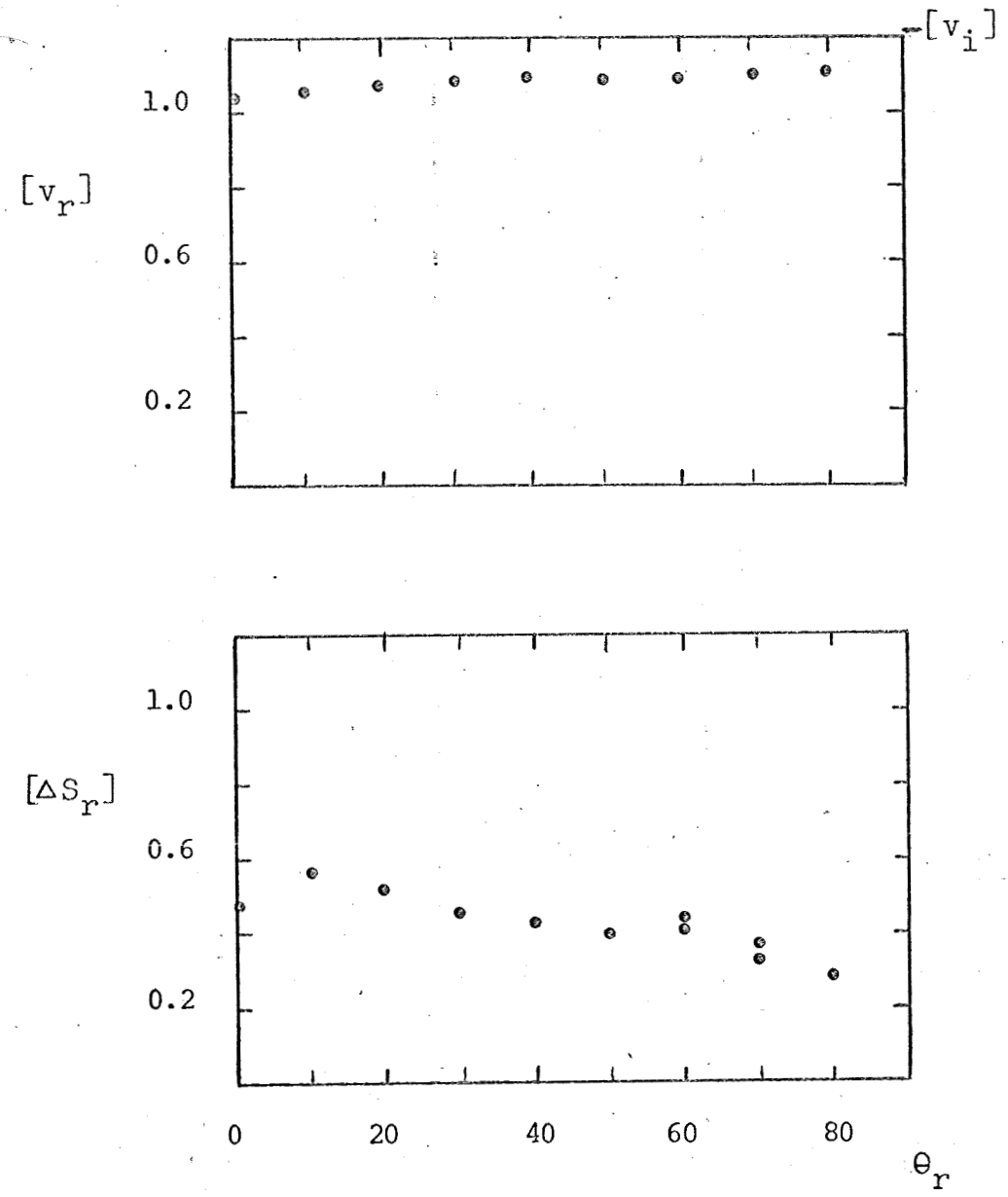

Figure 5.2.10

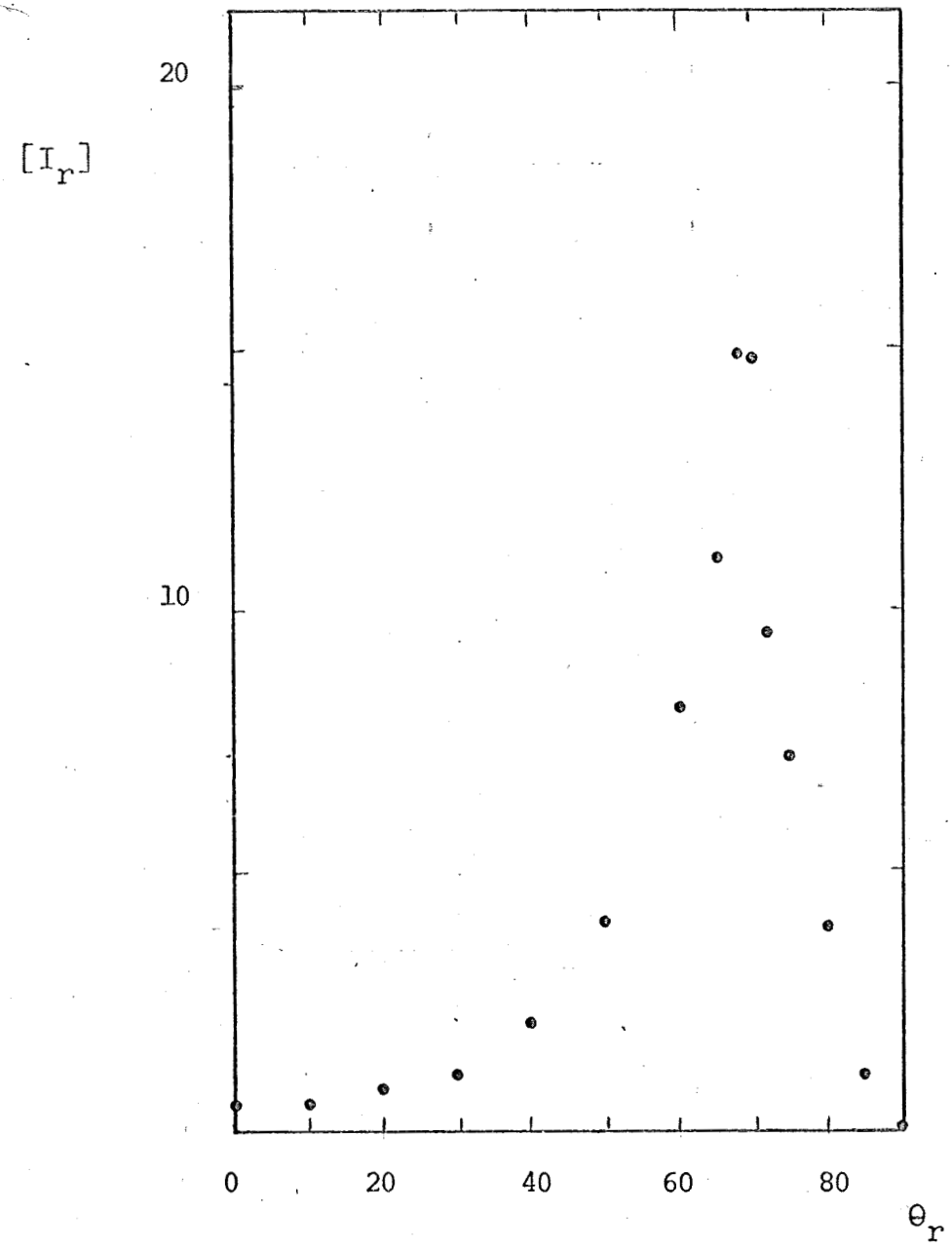

Figure 5.2.11 Helium(300)/Ag(600) II

θ_i	θ_r	τ	α	SF	ET
70		0	0	110	170.3-171.3

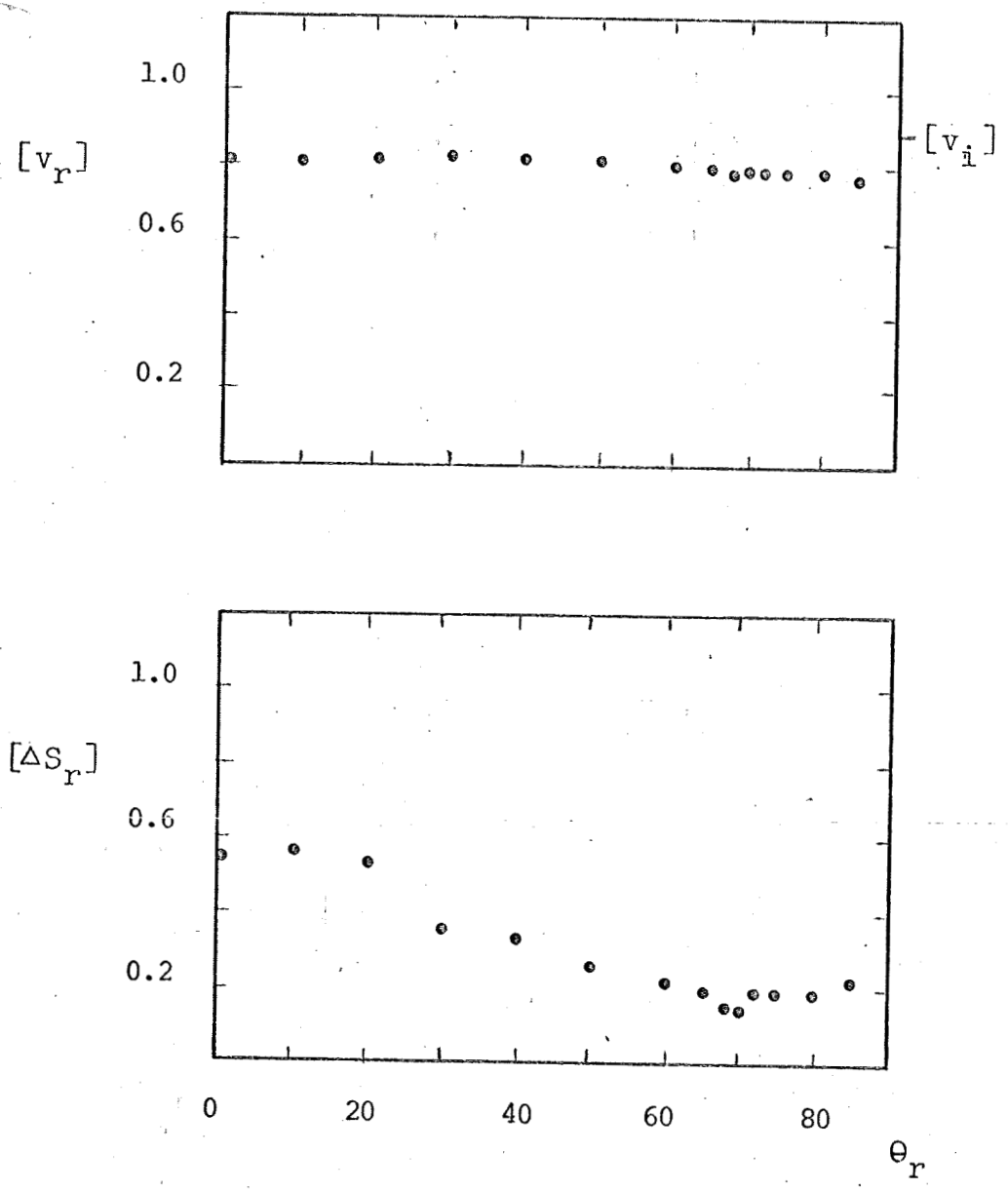

Figure 5.2.11

under similar conditions before aging (see Figure 5.2.8). The most noticeable changes in overall behavior are a reduction of the specular intensity to 60% of its previous value and a decline in SF from 210 to 110. This decline of SF to values near 110 signals the transition to Phase II of the surface.

Figure 5.2.12 presents data analagous to that of the previous figure except that now $T_s = 700^oK$. Inspection of both Figures 5.2.11 and 5.2.12 leads to the conclusion that over the temperature range $600^oK \leq T_s \leq 700^oK$ the variation of $[\Delta S_r]$ with θ_r for the Phase II surface displays the same trends previously noted for the Phase I surface, i.e., $[\Delta S_r]$ tends to exhibit a minimum at $\theta_r = \theta_i$, tends to level off for $\theta_r > \theta_i$, and rises between $\theta_r = \theta_i$ and $\theta_r \approx 20^o$. Although the maximum value of $[I_r]$ is somewhat diminished at the higher T_s, SF is, in fact, slightly increased. The increase in SF is sensible; the corresponding decrease in peak intensity is not and may be due to some unknown factor in the experiments. Regarding the mean speeds, note that the values of $[v_r]$ decrease slightly with increasing T_s over the range. Since $\langle v_s \rangle$ must increase by $(7/6)^{\frac{1}{2}}$ as T_s increases from 600^oK to 700^oK, the comparatively lesser decrease in $[v_r]$ could imply a small increase in the absolute value of the mean speed as T_s increases. Such behavior is somewhat surprising, however,

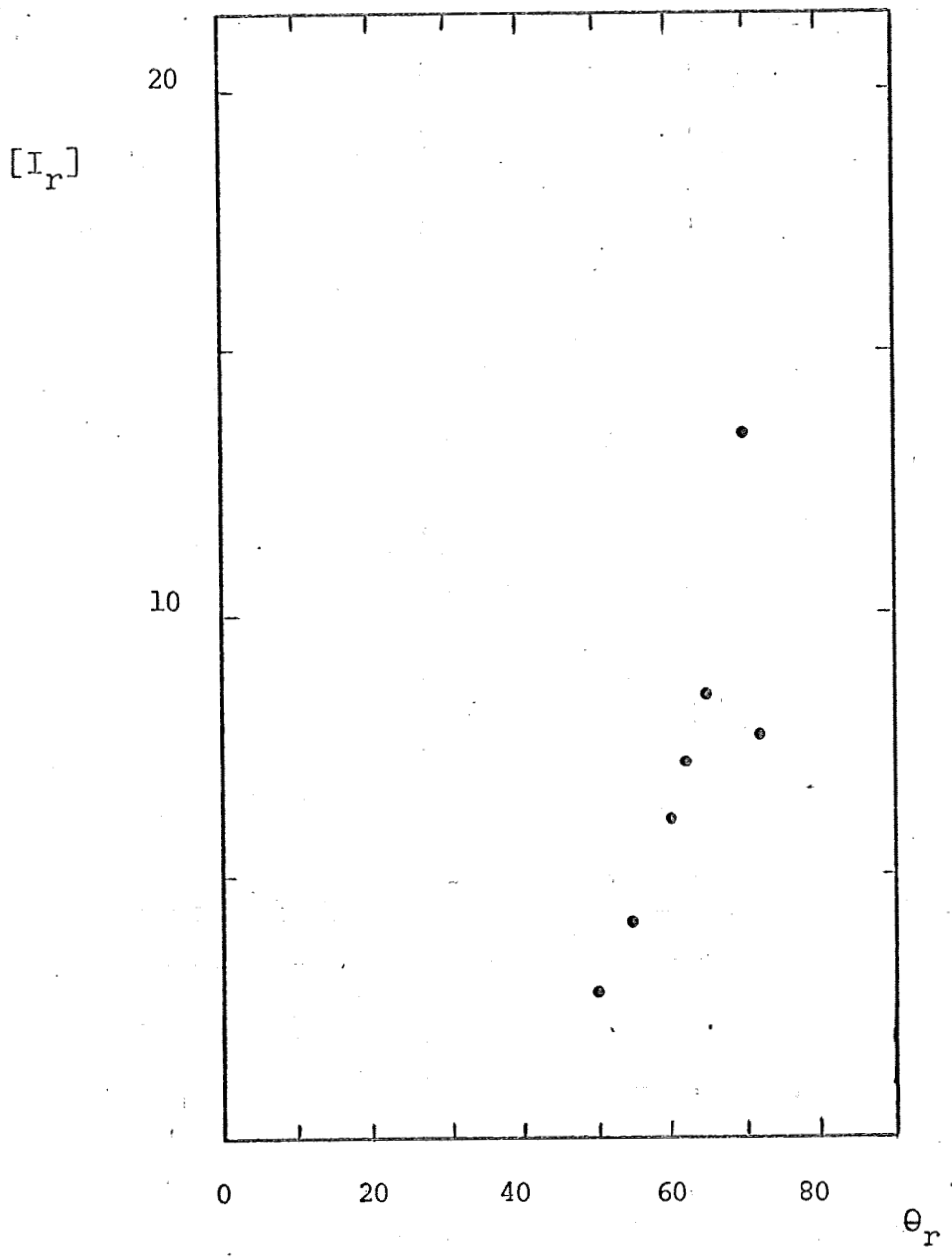

Figure 5.2.12 Helium(300)/Ag(700) II

θ_i	θ_r	τ	α	SF	ET
70		0	-40	120	299.3-299.5

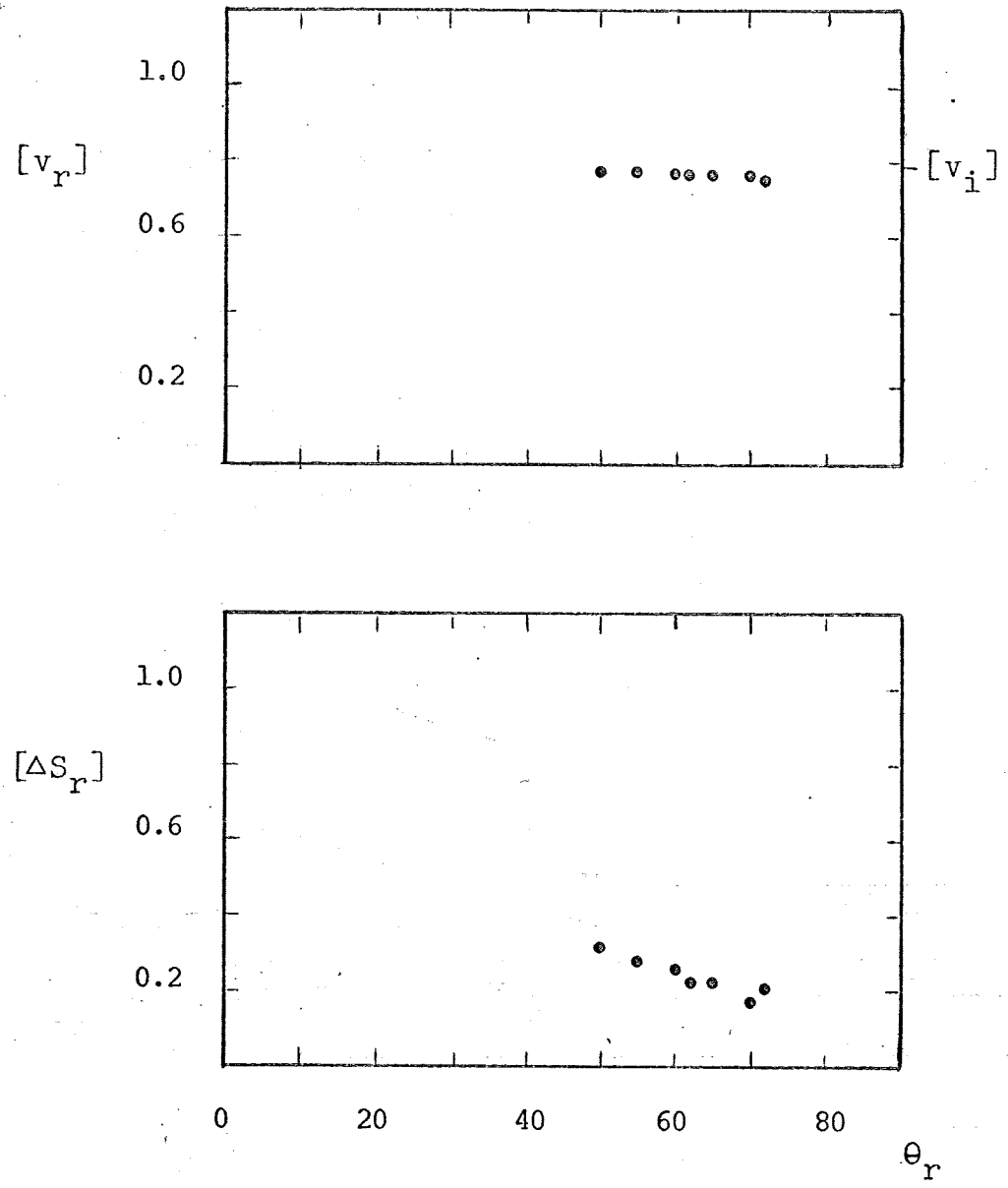

Figure 5.2.12

and it is well to recall that this apparent deviation from expectation is within the limits of experimental error.

As a final point in this sequence, the relative time stability of the Phase II surface may be seen by comparing the Figures 5.2.13 and 5.2.11 which present data taken three days apart under essentially identical test conditions. While there is approximately a 10% difference in peak intensity for the two data sets, SF is well preserved. Similarly, $[v_r]$ and $[\Delta S_r]$ are essentially unchanged, at least in the high $[I_r]$, high certainty range of $\theta_r \geq 30^\circ$. The small increase in $[v_r]$ and significant decrease in $[\Delta S_r]$ in the range $\theta_r < 30^\circ$ that occur in Figure 5.2.13 are not readily explained and may be spurious.

5.2.3 Phase III Data

Upon completion of exploration of the Phase II surface, the target was cooled to 300°K and then rapidly heated to 800°K in an attempt to identify the principal adsorbates. The technique employed was to face the target toward a continuously cycling mass spectrometer during this heating period in an effort to record the variation in partial pressure of the principal gases

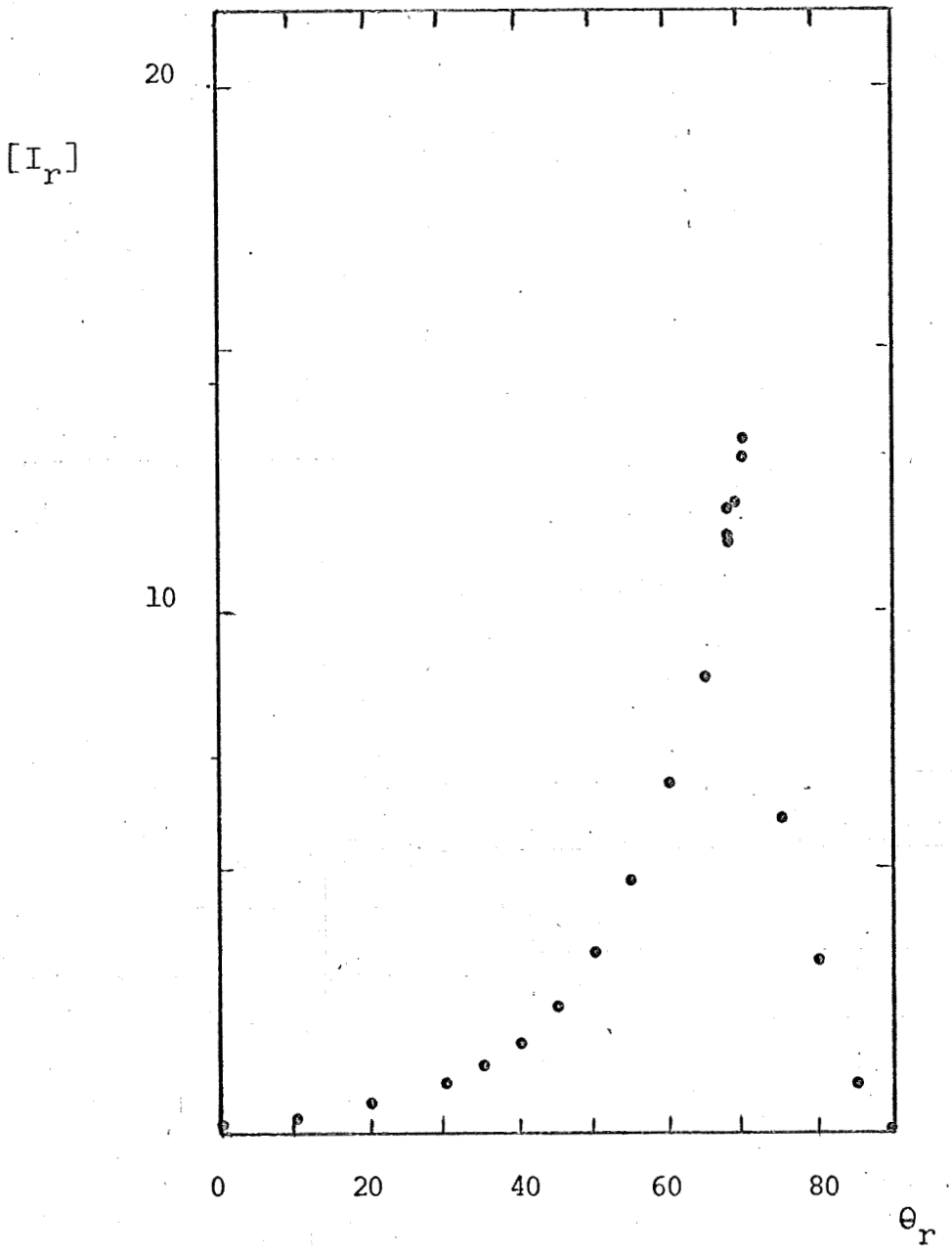

Figure 5.2.13 Helium(300)/Ag(600) II

θ_i	θ_r	τ	α	SF	ET
70		0	-14	110	241.2-243.2

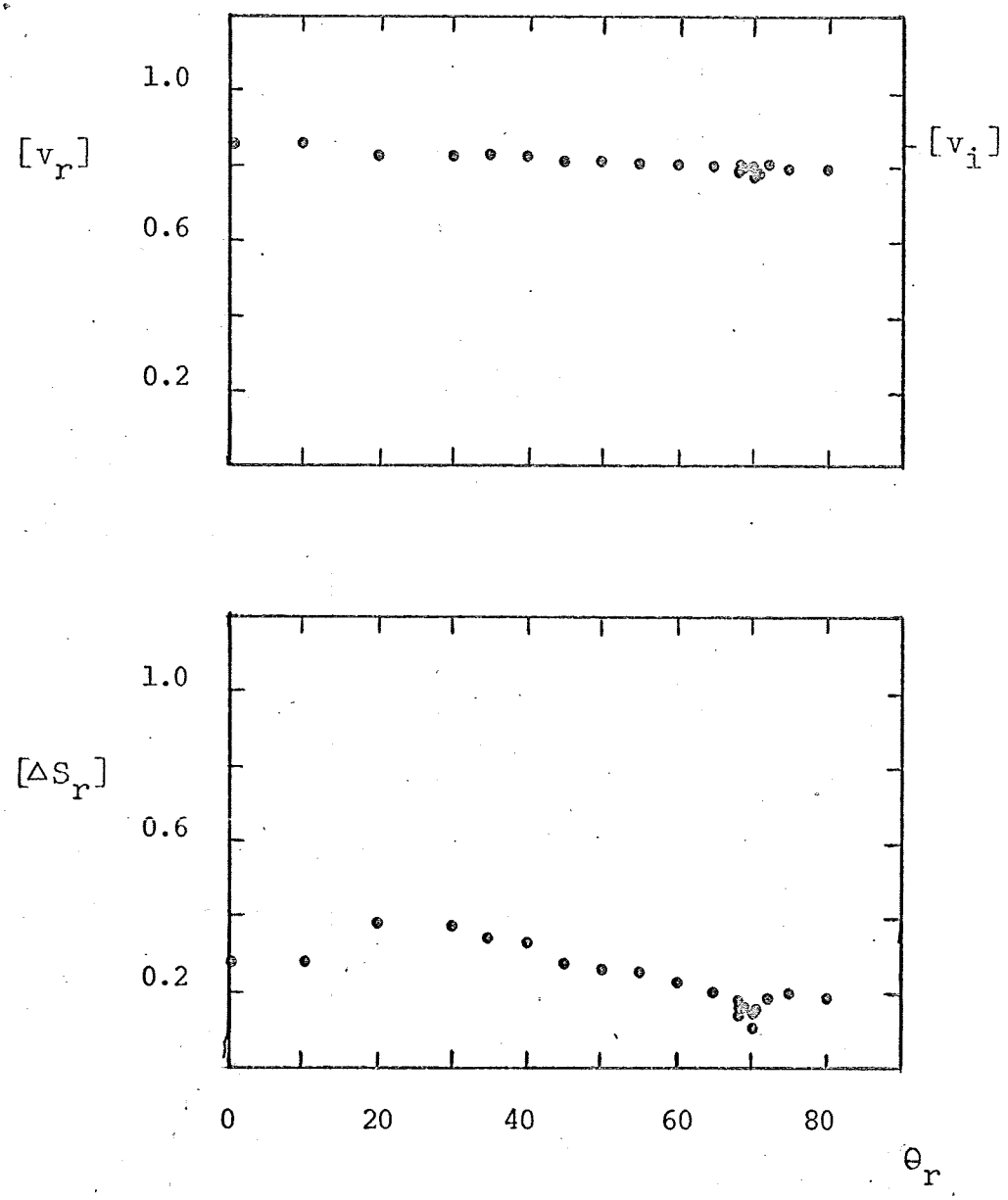

Figure 5.2.13

desorbed upon heating. The results obtained are discussed later on (Section 5.5).

Previous experimental work by Bishara [20] indicated that heating the target crystal to this range would result in thermal roughening of the surface. The surface as it existed at the end of this heat treatment will be referred to as the Phase III surface. The distributions of the scattered flux obtained from this surface in the principal plane at $T_s = 720^{\circ}K$ are displayed in Figures 5.2.14 (taken at $\theta_i = 65^{\circ}$) and 5.2.15 (taken at $\theta_i = 70^{\circ}$). Comparison of Figure 5.2.15 with Figure 5.2.12 indicates a nearly three-fold decrease in specular intensity and an even greater decline in the shape factor, SF. For the Phase III surface, there is also a more prominent increase in $[\Delta S_r]$ with decreasing θ_r in the range $\theta_r < \theta_i$. Aside from these changes, however, trends previously noted are substantially preserved.

Lowering the surface temperature to $600^{\circ}K$ (see Figure 5.2.16) effected a further decrease in specular intensity and a substantial decrease in the shape factor. It is plausible that roughening of the surface has resulted in an increase in the relative number of adsorption sites available per unit area (on the macroscopic scale) and thus has effectively increased the threshold temperature for significant adsorption. It has certainly contributed to rendering the interaction more diffuse and the correlation

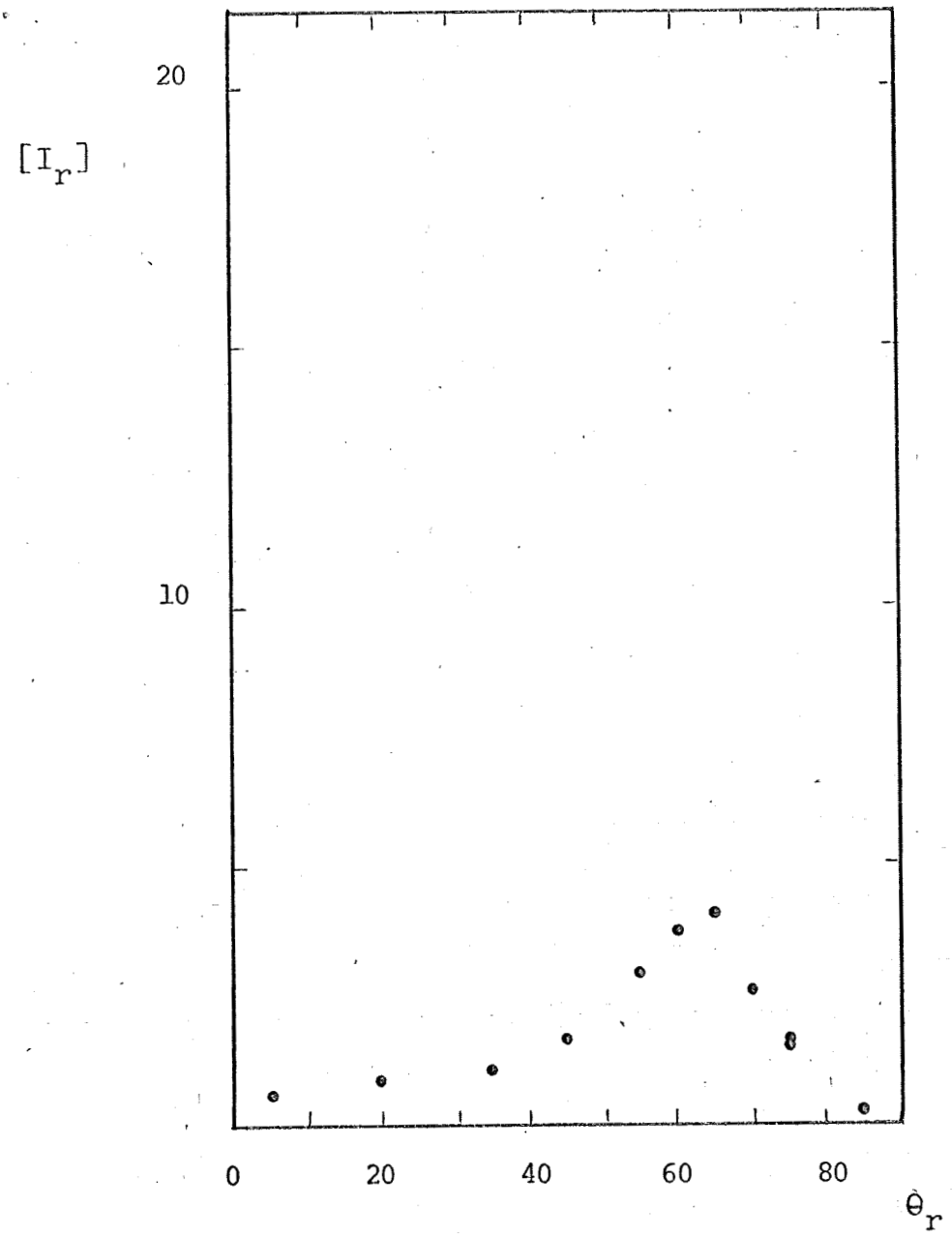

Figure 5.2.14 Helium(300)/Ag(720) III

θ_i	θ_r	τ	α	SF	ET
65.2		0	-12	20	318.7-319.3

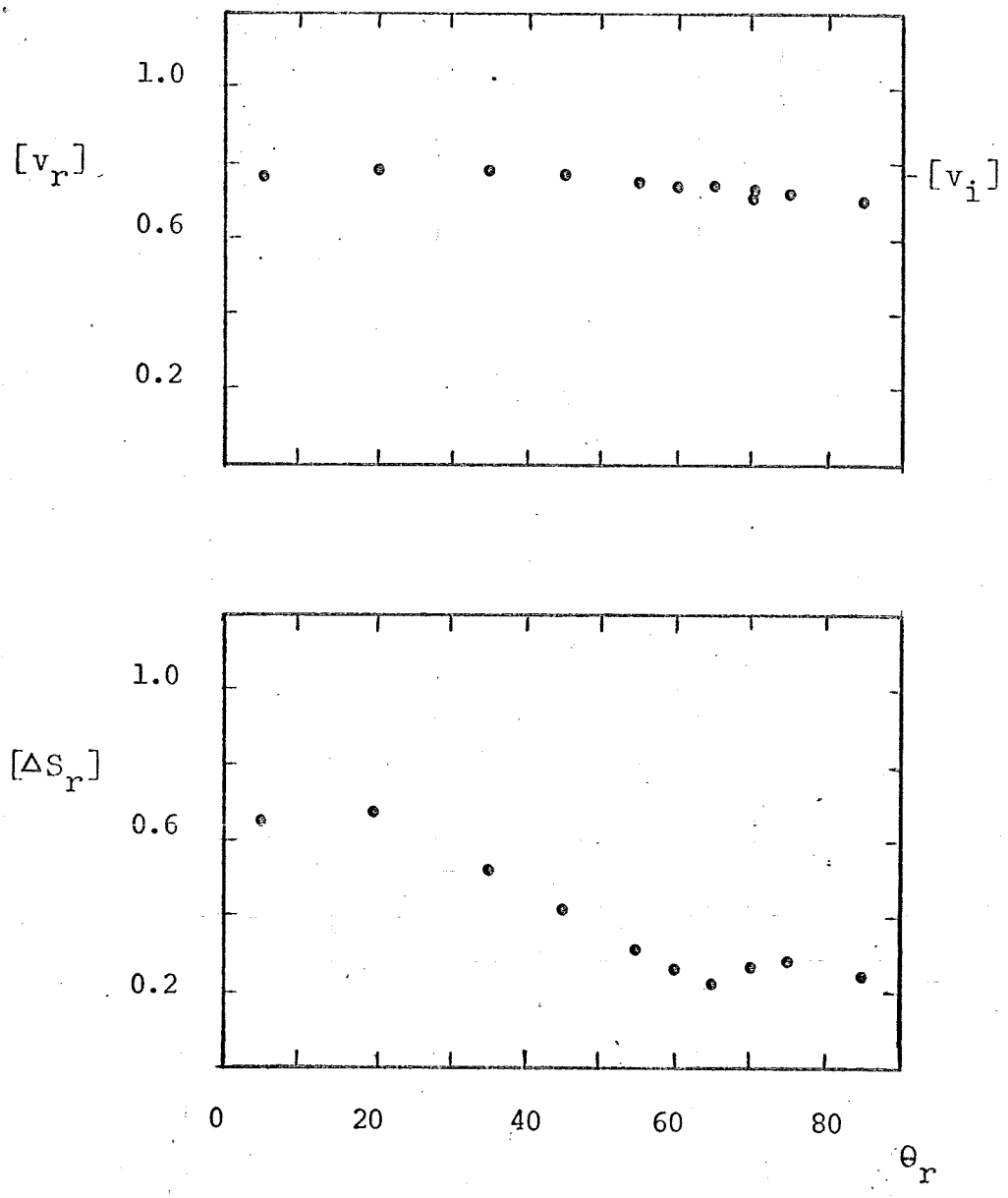

Figure 5.2.14

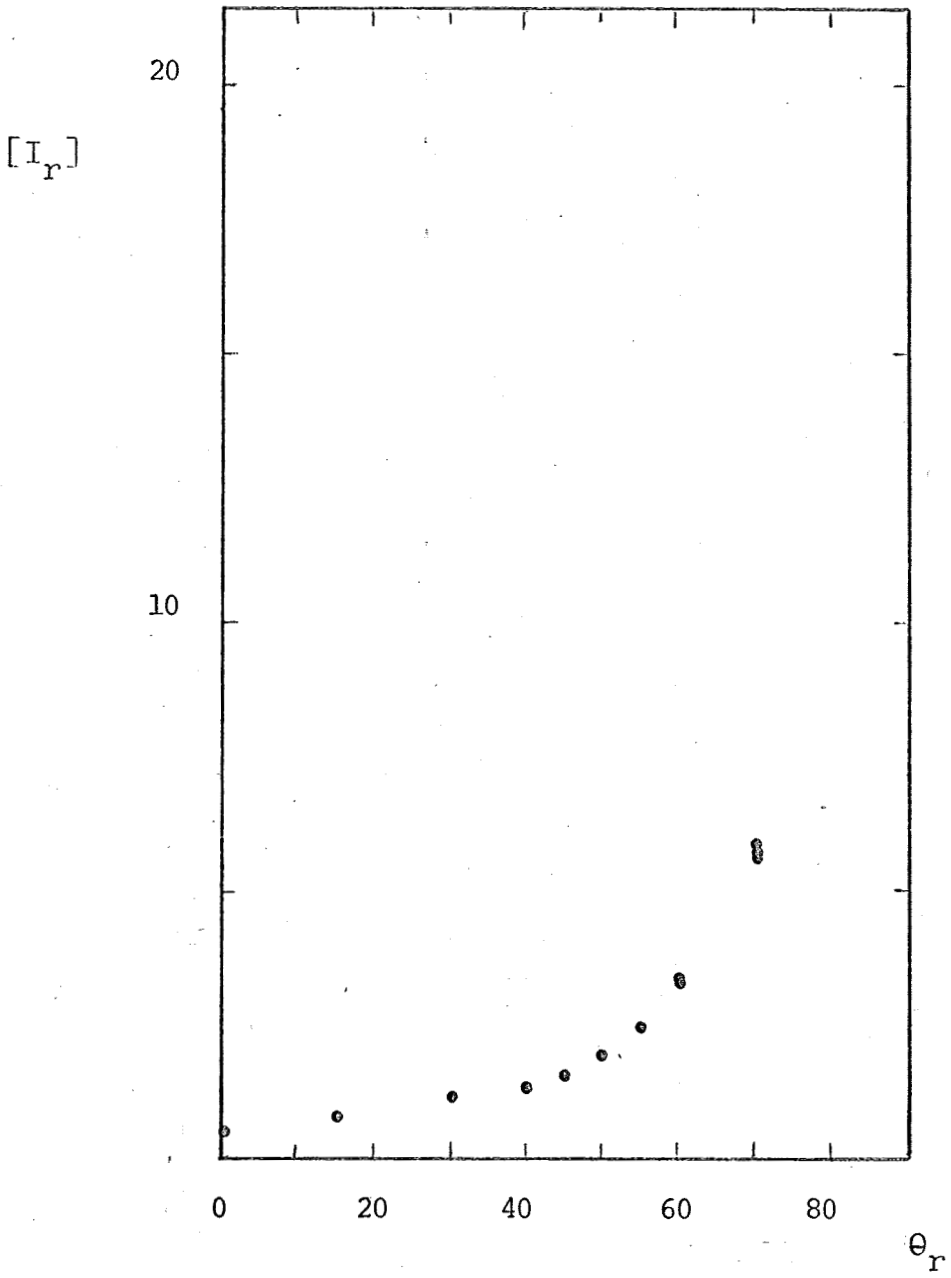

Figure 5.2.15 Helium(300)/Ag(720) III

θ_i	θ_r	τ	α	SF	ET
70		0	-12	30	319.5-320.8

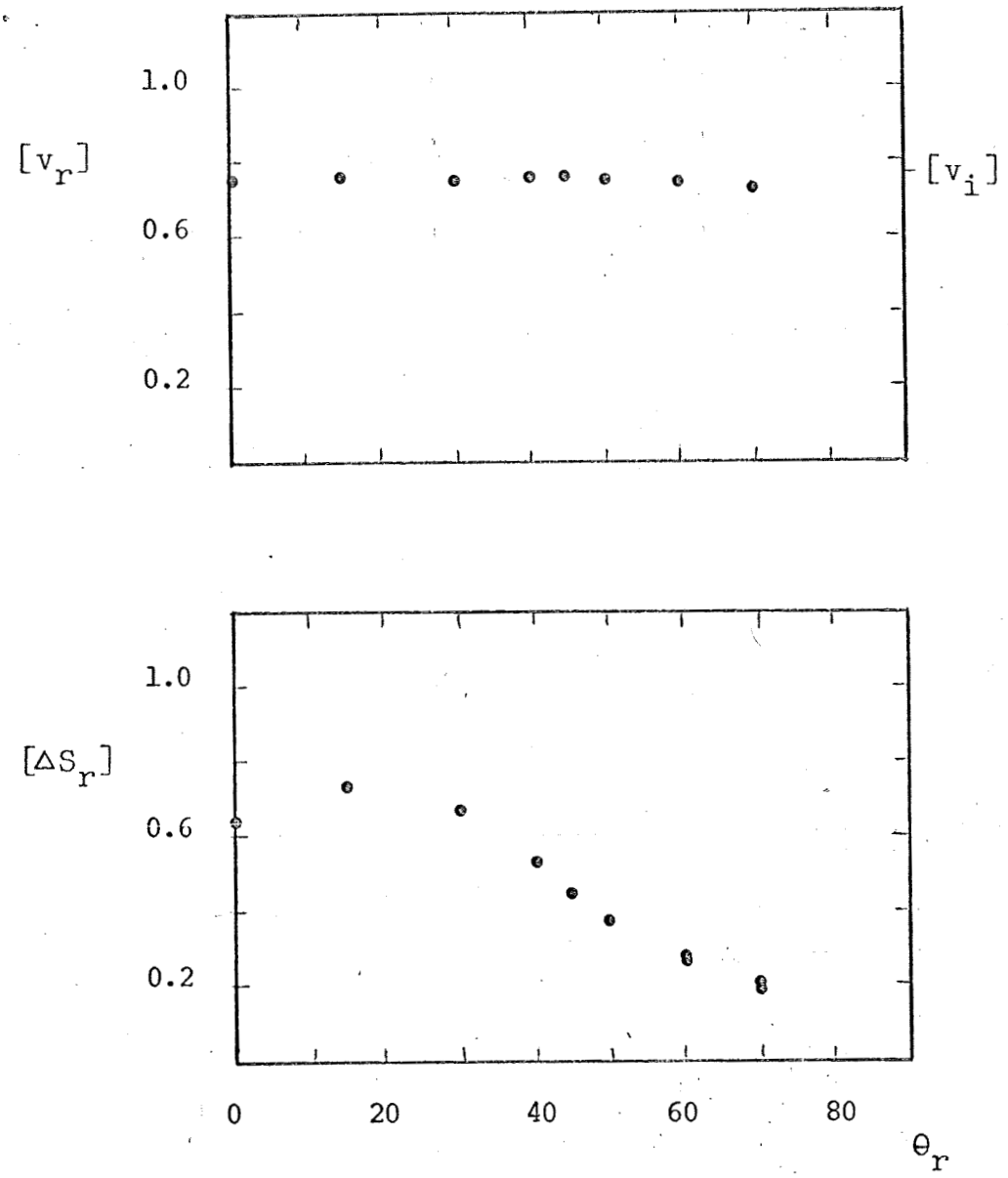

Figure 5.2.15

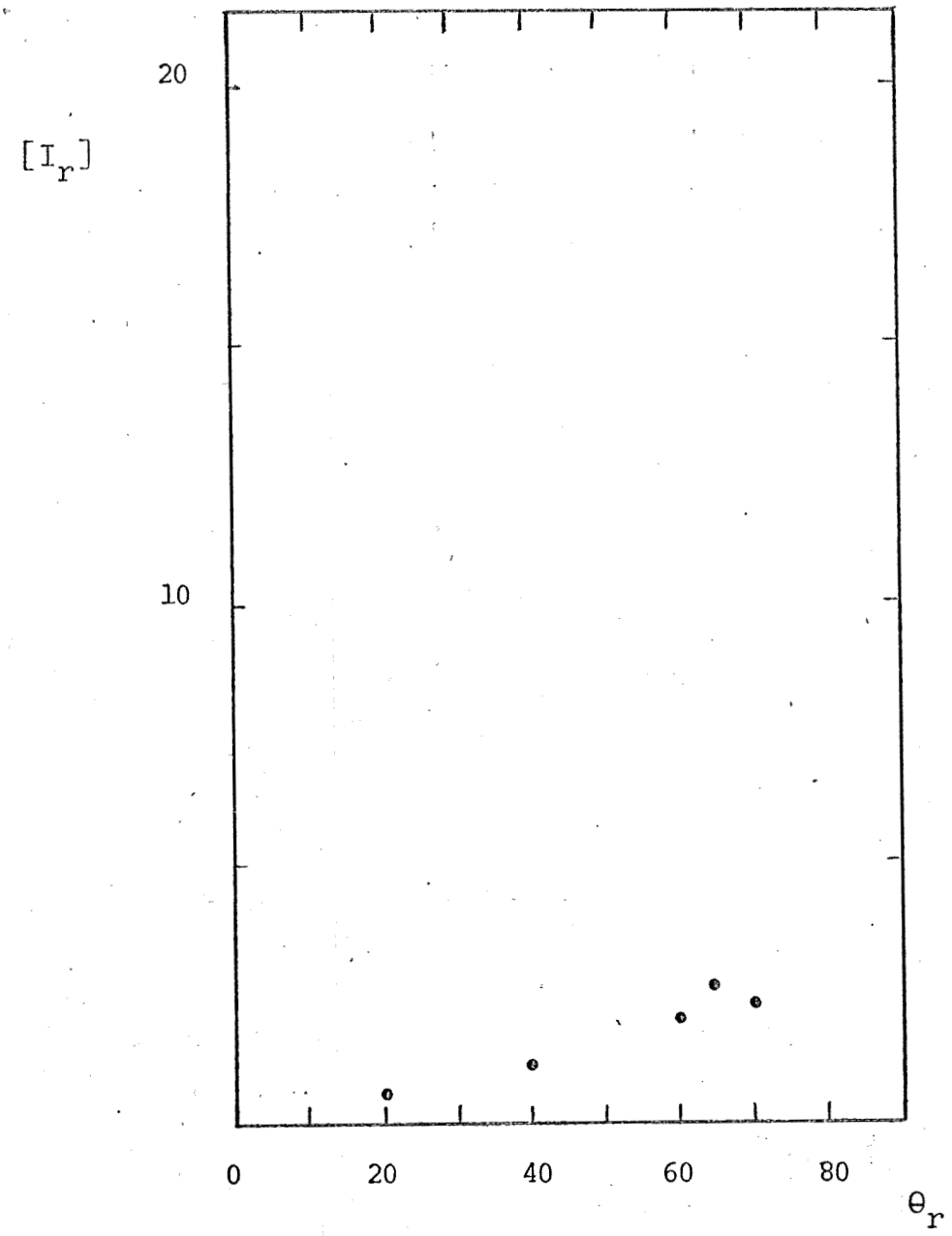

Figure 5.2.16 Helium(300)/Ag(600) III

θ_i	θ_r	τ	α	SF	ET
70		0	-12	9	321.0-321.3

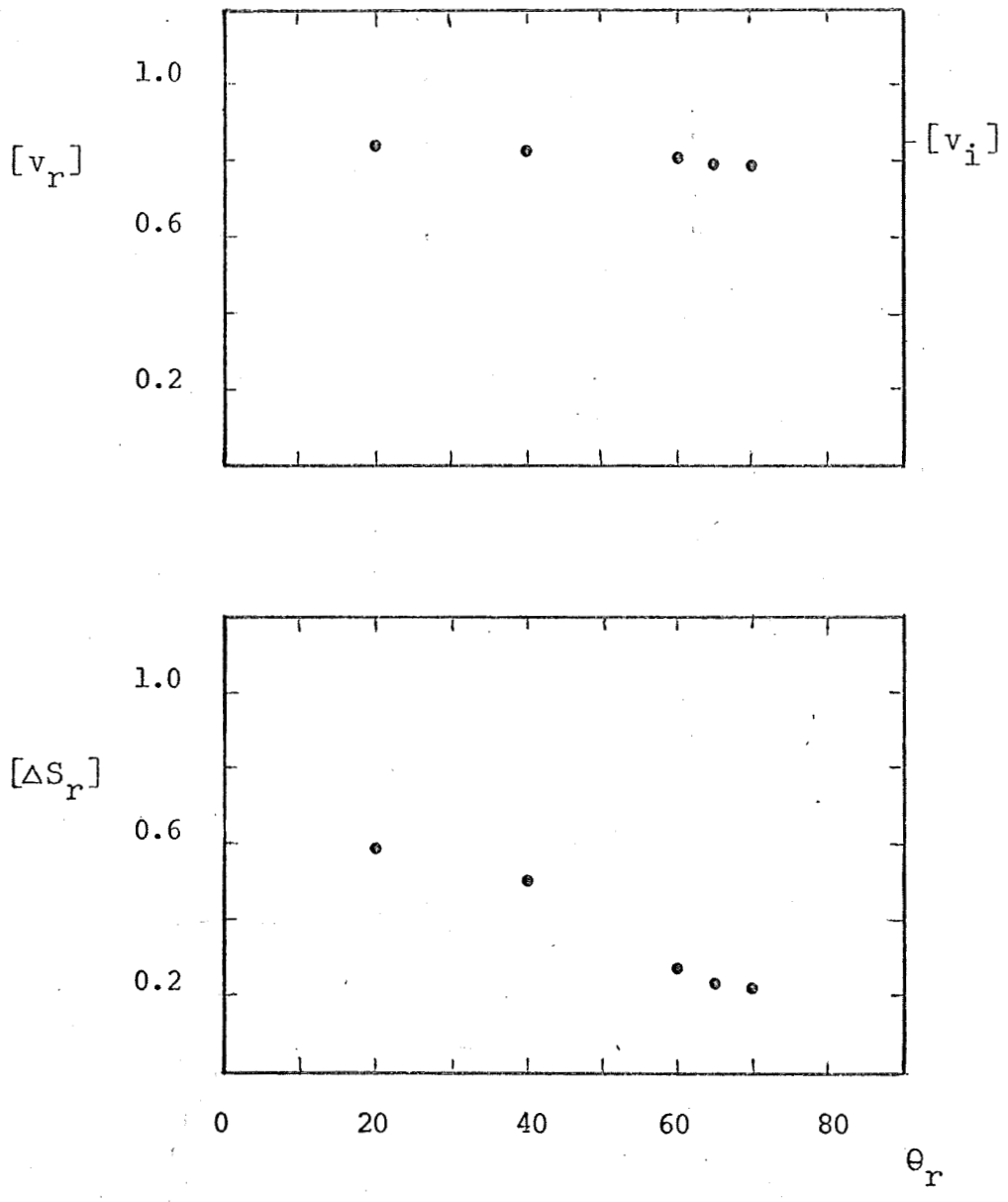

Figure 5.2.16

of increased diffuseness with lowering surface temperature serves as a generally reliable indicator of increased adsorption.

5.3 Argon Data

On the basis of Bishara's results [20] and the increased target-detector spacing in the present experiments, it was anticipated that the signal-to-noise ratio would be marginal for the argon experiments. This expectation proved correct and, consequently, data were recorded only for the Phase II target and only at the higher target temperatures previously employed, i.e., $600^{\circ}K \leq T_s \leq 700^{\circ}K$.

The three-dimensional scattering distributions for room temperature argon incident at $\theta_i = 50^{\circ}$ onto a $600^{\circ}K$ surface are presented in Figures 5.3.1 and 5.3.2. These figures depict principal and transverse plane distributions, respectively. The transverse planes chosen are those for $\theta_r = 40^{\circ}$, 50°, and 60°. Recall that the same region of scattering space was explored for helium on a Phase I surface in Figures 5.2.1 and 5.2.2. The preservation of all qualitative trends in helium scattering from the Phase I to the Phase II surface permits qualitative

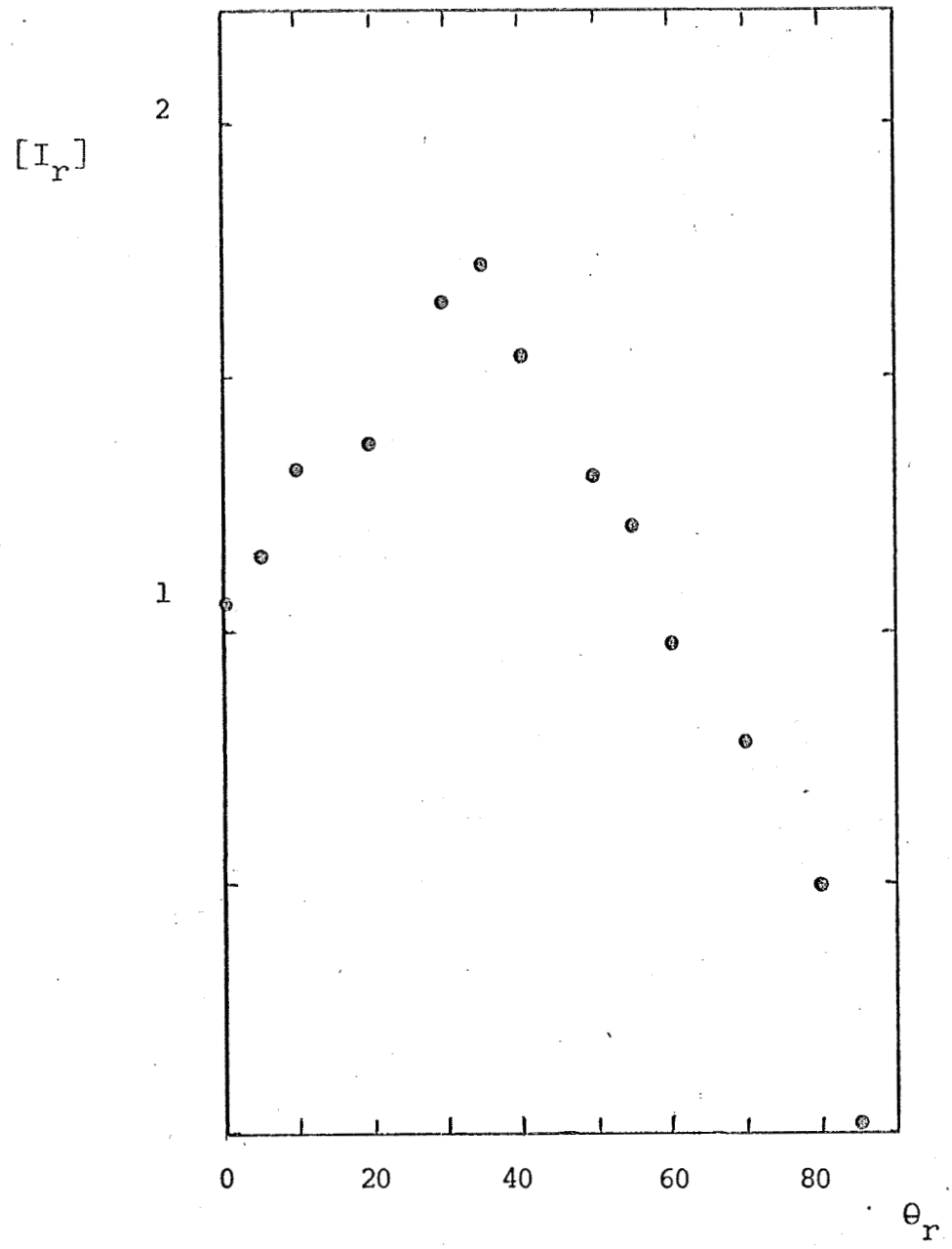

Figure 5.3.1 Argon(300)/Ag(600) II

θ_i	θ_r	τ	α	SF	ET
50		0	0		266.3-267.5

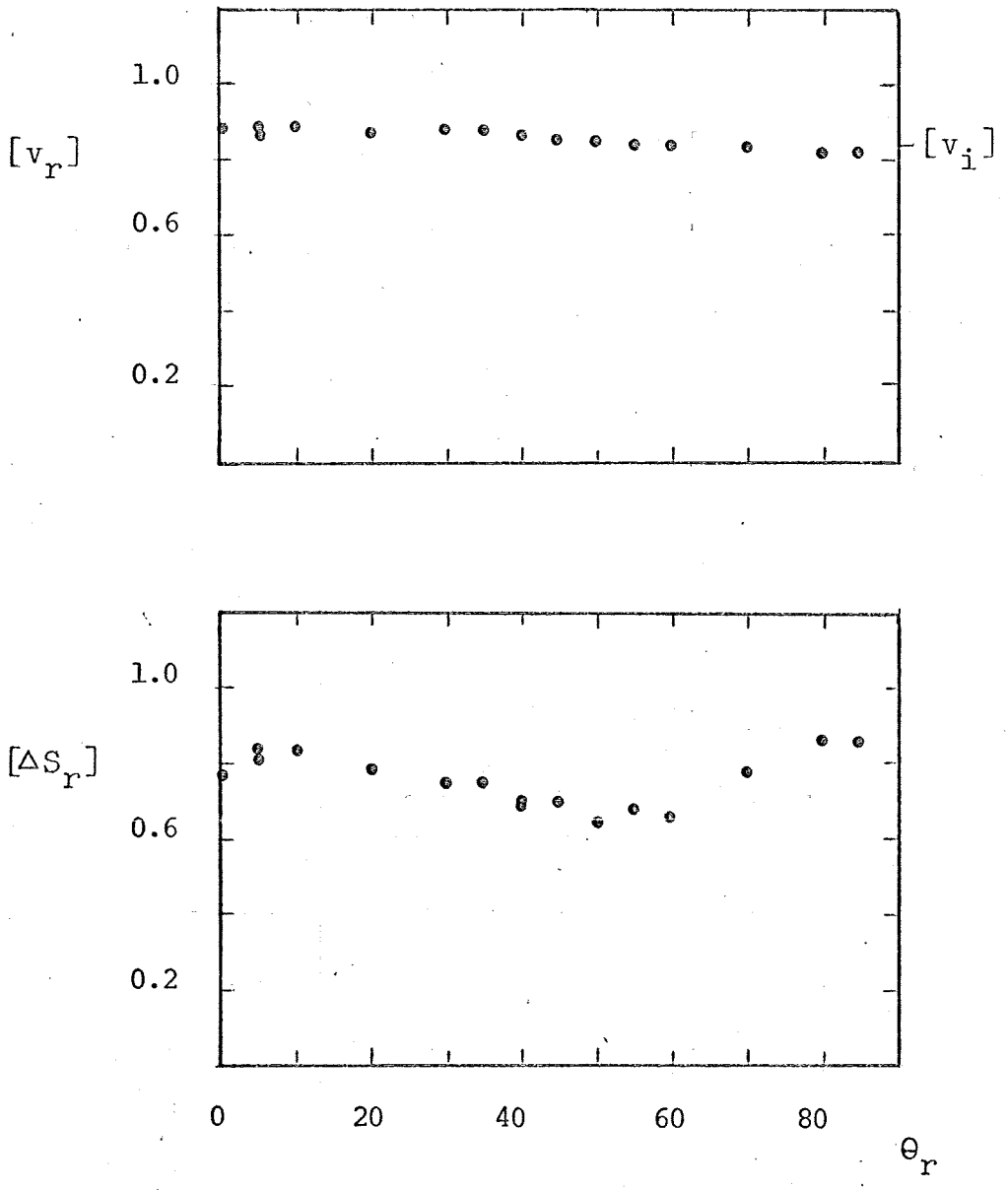

Figure 5.3.1

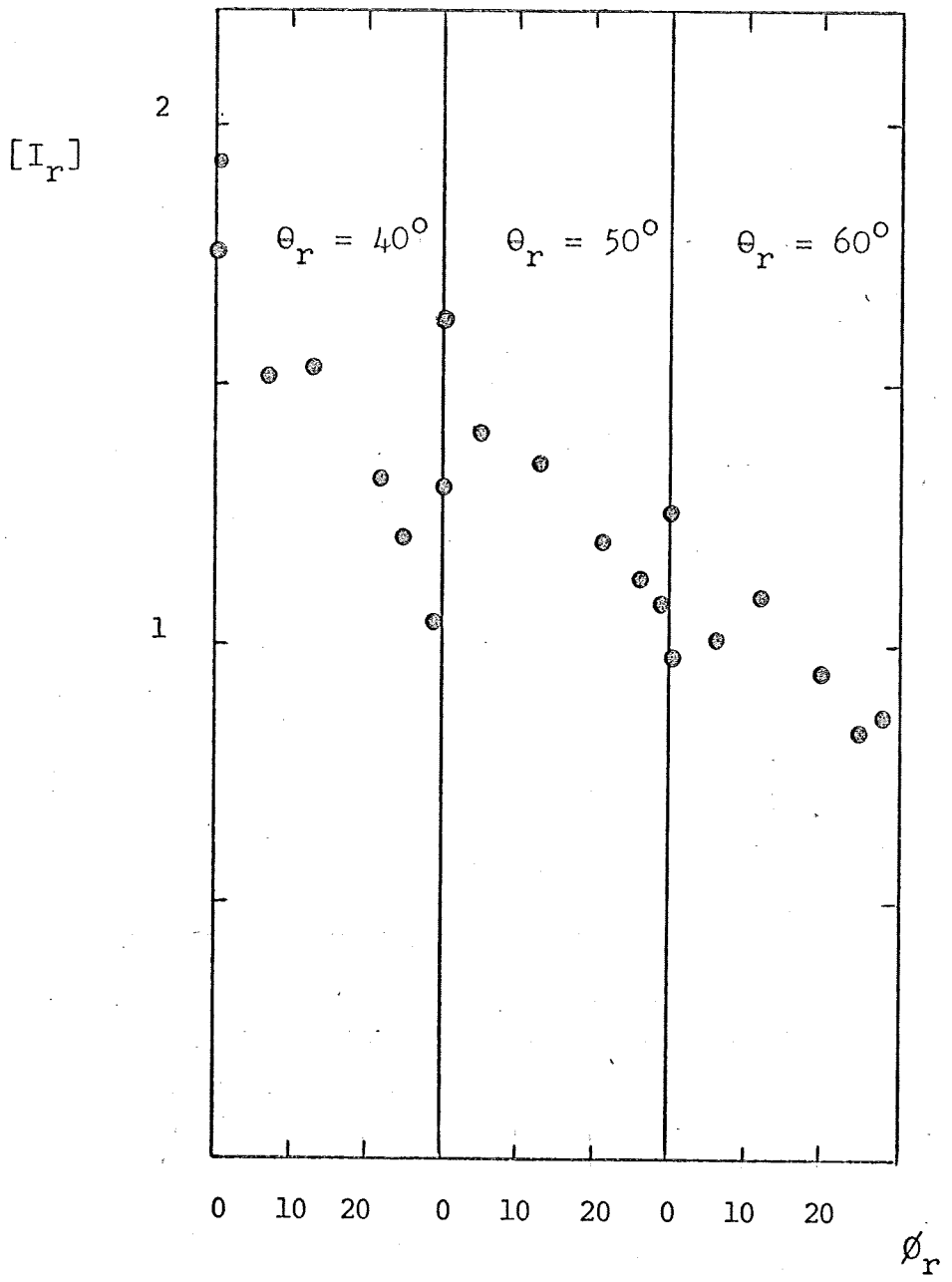

Figure 5.3.2 Argon(300)/Ag(600) II

θ_i	θ_r	τ	α	SF	ET
50					267.5-268.8

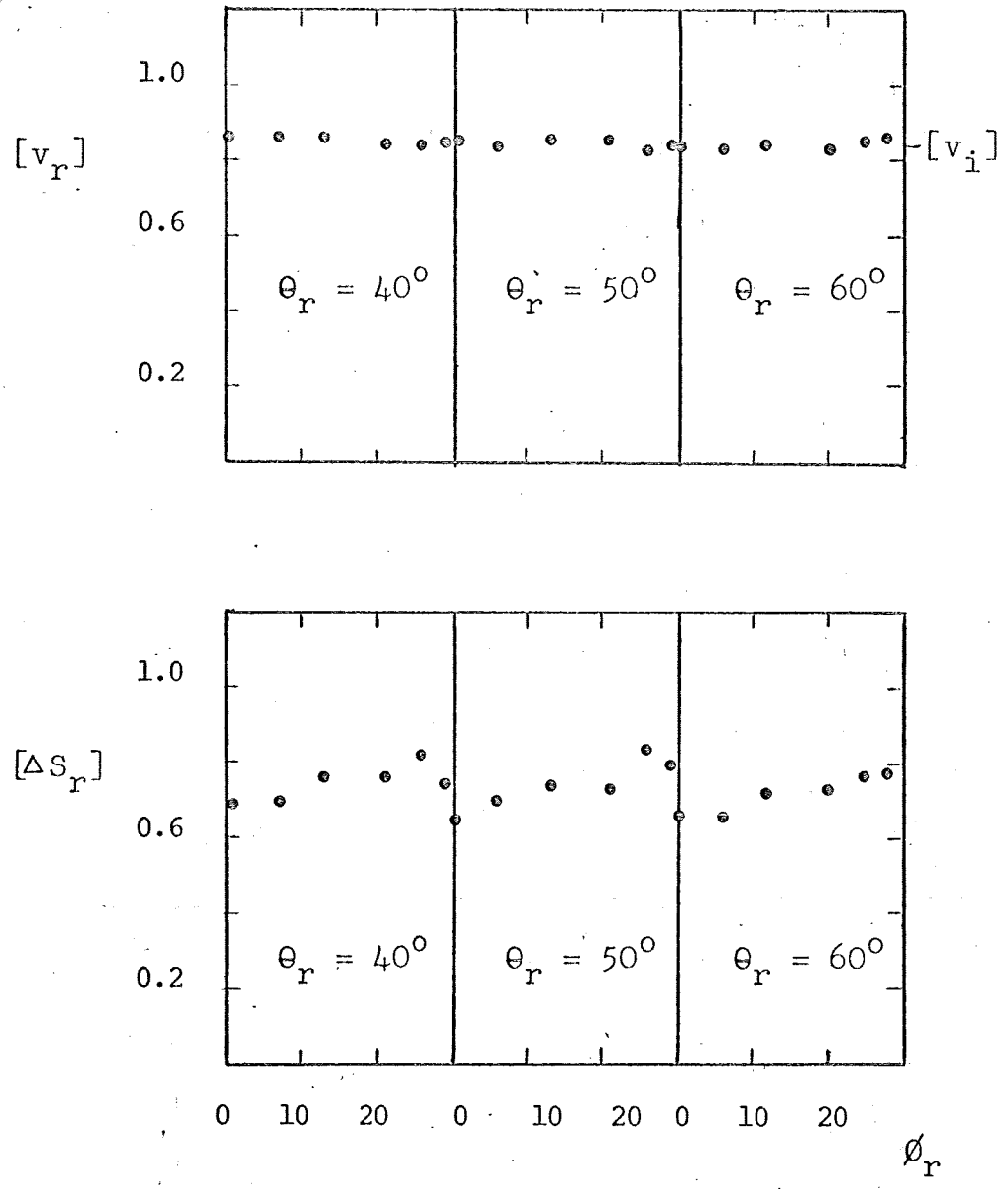
1.0
0.6
0.2
[v_r]
[v_i]
$\theta_r = 40^\circ$
$\theta_r = 50^\circ$
$\theta_r = 60^\circ$
1.0
0.6
0.2
[ΔS_r]
$\theta_r = 40^\circ$
$\theta_r = 50^\circ$
$\theta_r = 60^\circ$
0 10 20 0 10 20 0 10 20
ϕ_r

Figure 5.3.2

comparisons of behavior between Figures 5.3.1 - 5.3.2 and 5.2.1 - 5.2.2. The most obvious differences in the distributions of $[I_r]$ between the two gases are a) a pronounced subspecular shift of the intensity maximum in the principal plane for argon and b) an increased prominence of diffuse scattering for argon, the latter evidenced by the high intensity at the normal relative to that at the maximum. The subspecular (toward the normal) shift of the intensity maximum is on the order of 15°. As a result of the increased diffuseness of the scattering, the distributions of $[I_r]$ in both the principal and transverse planes are far broader than those for helium.

Principal plane values of the normalized mean speed, $[v_r]$, for argon display a more pronounced increase as $\Theta_r \rightarrow 0$. Again, it is estimated that the values of $[v_r]$ as plotted are systematically low, in the case of argon by about 4%. (see Reference [15].) On this assumption, the data indicate that $[v_r]$ is still closer to $[v_i]$ than to $[v_s] \equiv 1$, indicating only moderate energy accommodation of the argon atoms. Principal plane values of the speed spread, $[\Delta S_r]$, are nearly twice those observed for helium, indicating a proportionate decrease in speed-coherency in the argon-silver interaction. It is interesting to note in this regard that the behavior of the speed spread in the vicinity of the normal for argon scattering from

the Phase II surface is very similar to the behavior approached by helium scattering from the Phase III (rougher) surface. Significantly, however, the helium data, even in this state, consistently displayed noticeably smaller values for $[\Delta S_r]$.

In terms of trends, the speed spread for argon has a less sharply defined minimum which occurs not at the specular but in the range between $\Theta_r = \Theta_{rm}$ (the position of the intensity maximum) and the specular. Furthermore, $[\Delta S_r]$ tends to increase, by similar amounts, both for $\Theta_r < \Theta_{rm}$ and $\Theta_r > \Theta_i$. This contrasts with the behavior for helium where $[\Delta S_r]$ exhibited a minimum consistently at the specular direction and increased significantly only as Θ_r decreased. In the transverse planes, $[\Delta S_r]$ for argon is seen to decrease to a relative minimum at the intersection with the principal plane.

In summary, the interaction of argon with silver is much more diffuse than that of helium with silver and leads to a greater loss in speed-coherency between the incident and scattered atoms.

The dependence of the distributions of intensity, mean speed, and spread in the principal plane on the angle of incidence of the argon beam has been explored. This dependence is illustrated for $\Theta_i = 35^\circ$, 50°, and 70°, first for $T_s = 600^\circ K$, in Figures 5.3.3 - 5.3.5, and then for

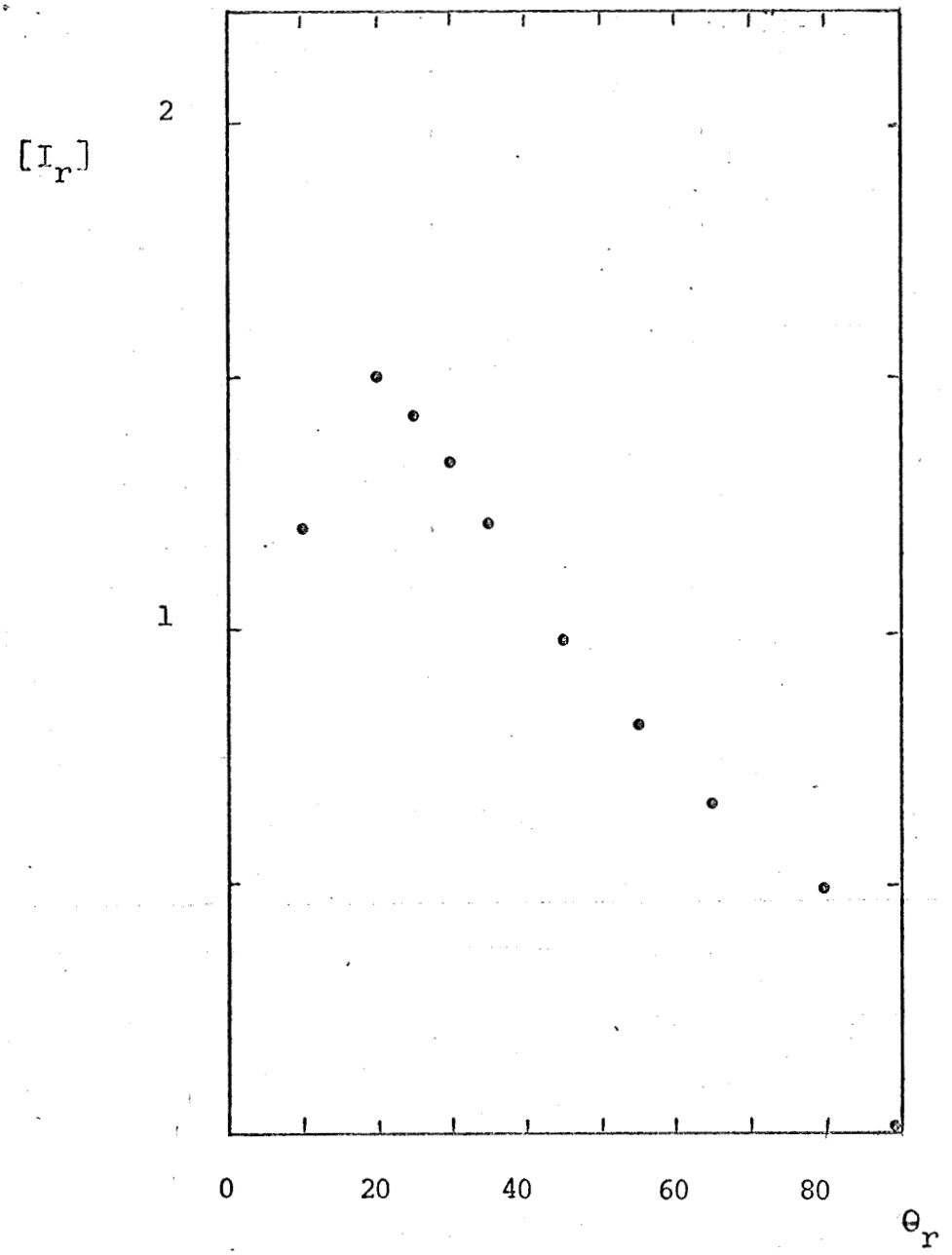

Figure 5.3.3 Argon(300)/Ag(600) II

θ_i	θ_r	τ	α	SF	ET
35		0	-12		287.7-288.5

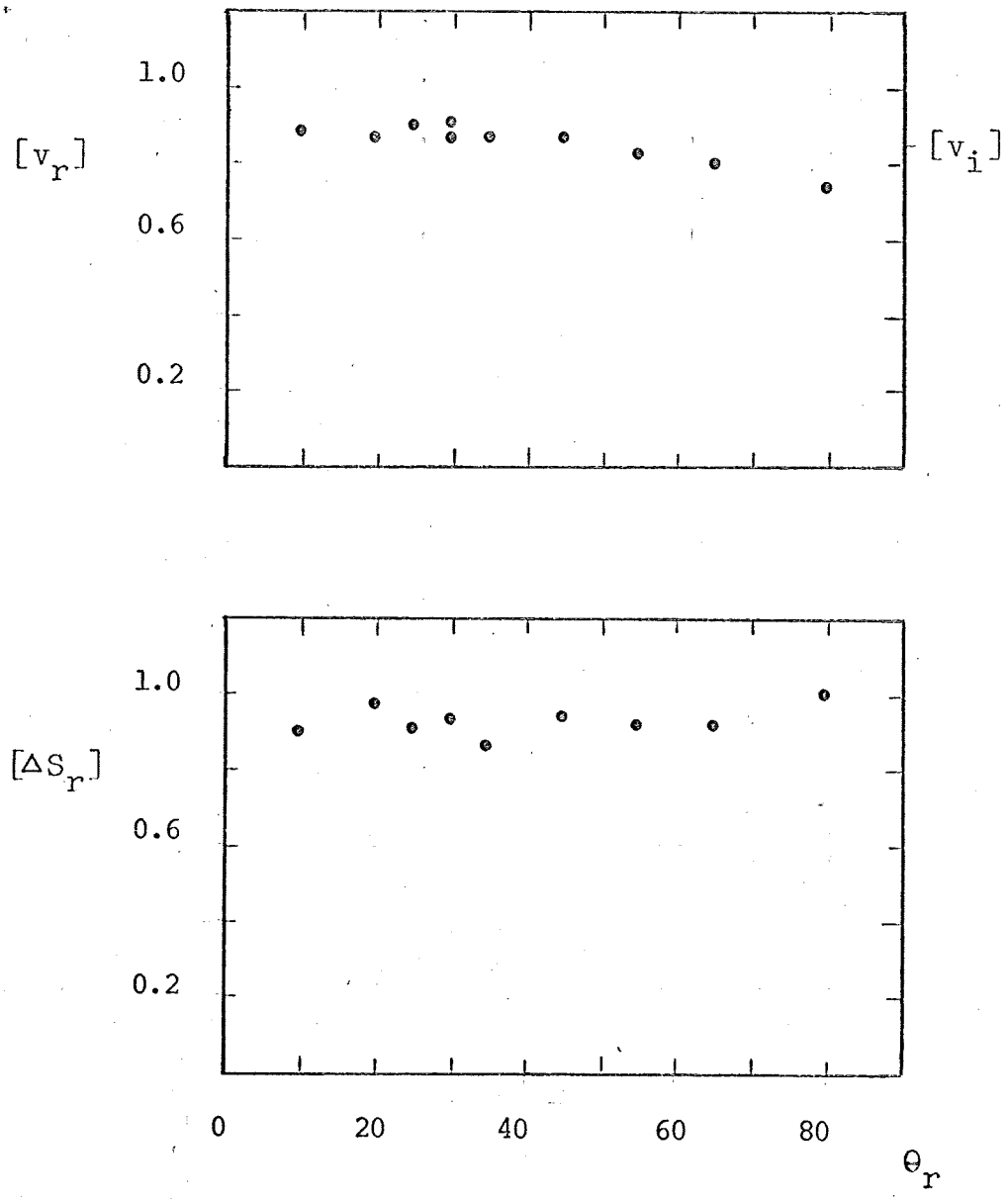

Figure 5.3.3

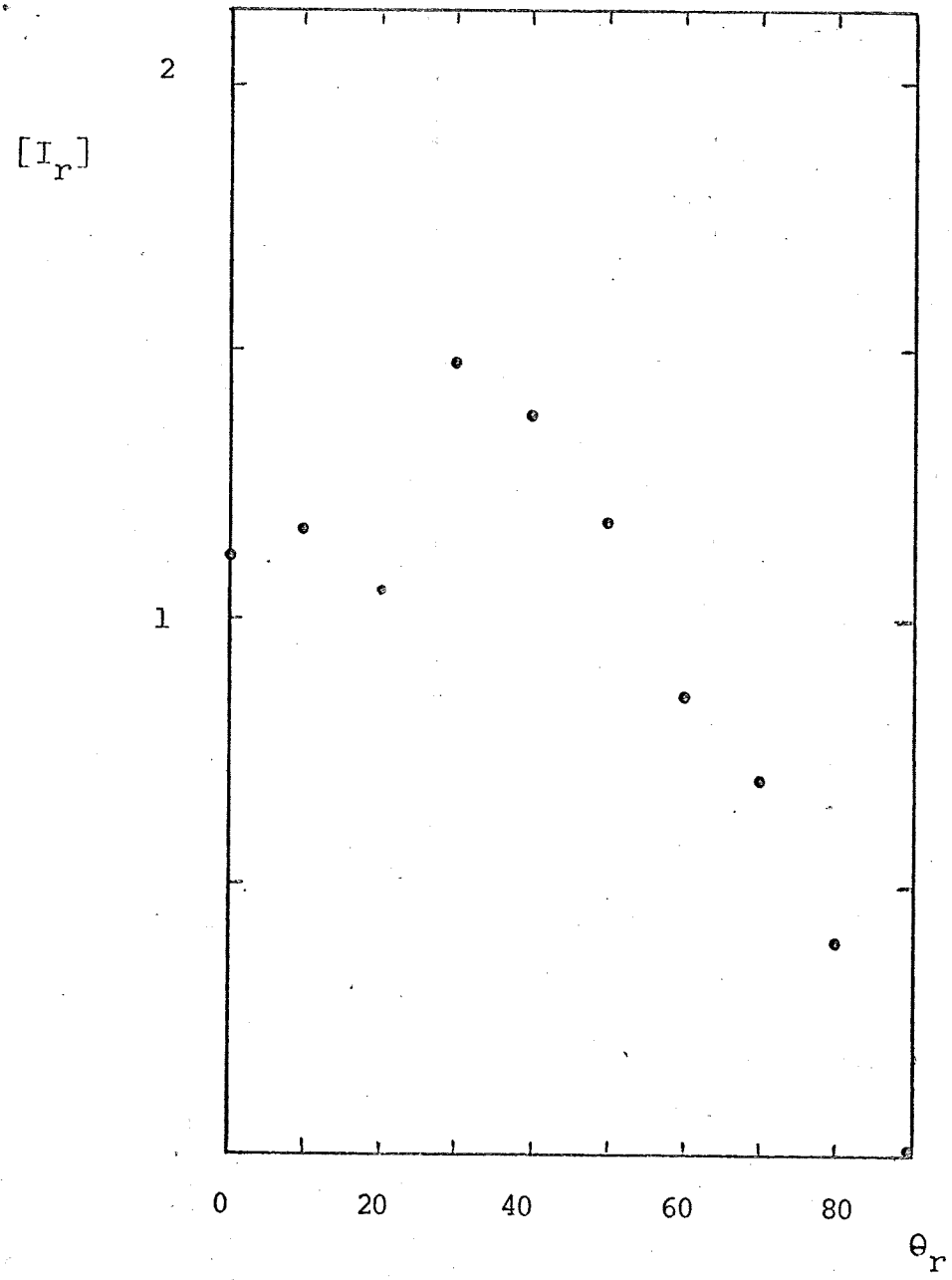

Figure 5.3.4 Argon(300)/Ag(600) II

θ_i	θ_r	τ	α	SF	ET
50		0	-12		284.5-285.2

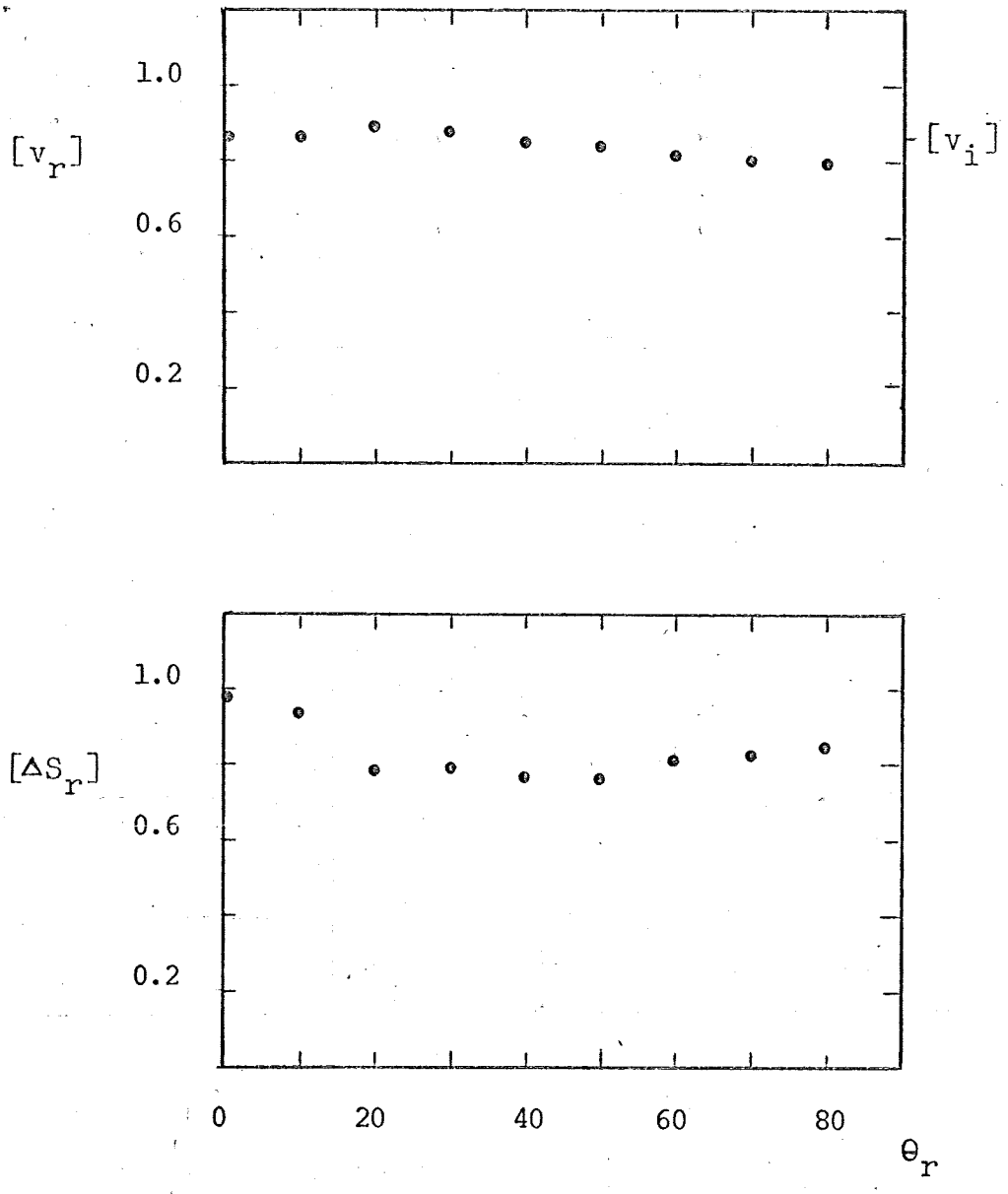

Figure 5.3.4

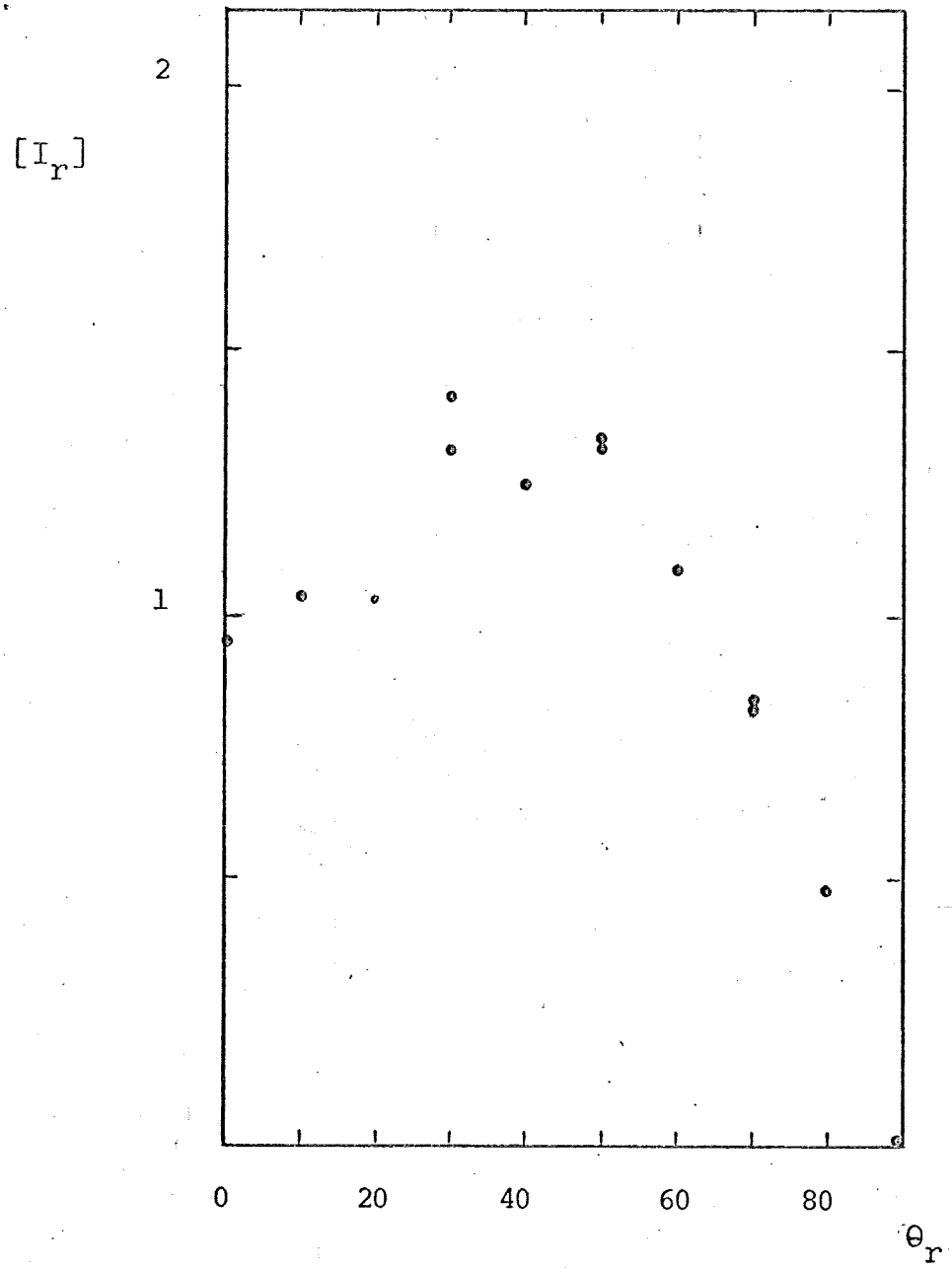

Figure 5.3.5 Argon(300)/Ag(600) II

θ_i	θ_r	τ	α	SF	ET
70		0	-12		285.3-287.7

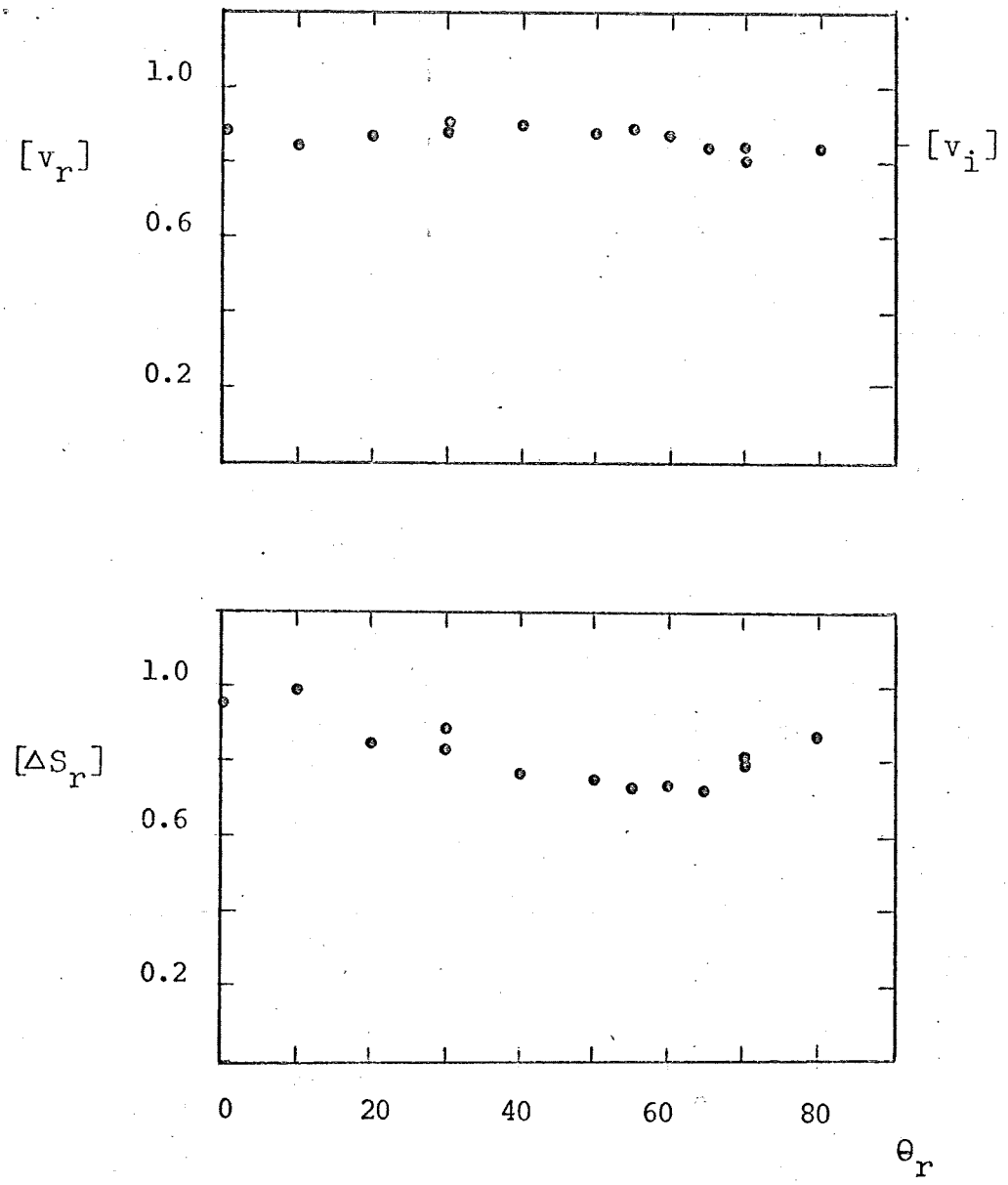

Figure 5.3.5

T_S = 700°K, in Figures 5.3.6 - 5.3.8. Upon inspection of these figures, it is observed that, at either T_S, the maximum values of the normalized intensities are clearly far less dependent upon θ_i than are their counterparts for helium. The variation of the maximum intensity with θ_i in the case of T_S = 700°K, which is the only case to show significant θ_i dependence, appears muted with a peak in the region between θ_i = 50° and θ_i = 70°. This behavior is markedly different from that observed by Saltsburg and Smith [3] for whom maximum intensity continually decreased with increasing θ_i over the same range, yet similar to that found by Bishara [20]. It is not immediately clear whether this difference in behavior is wholly attributable to the variance in surface quality between Saltsburg and Smith's "freshly deposited" surface and the relatively aged Phase II surface studied here. It is of interest, however, that as incident-beam temperature rises from 300°K to 1550°K in the data recorded in Saltsburg and Smith's [3] Figure 9, the θ_i-dependence of the maximum intensity gradually reverses its direction, apparently displaying a behavior similar to that seen here when their incident beam is in the vicinity of 1000°K. Little can be said here concerning how surface condition and beam temperature may be related in determining this θ_i-dependence.

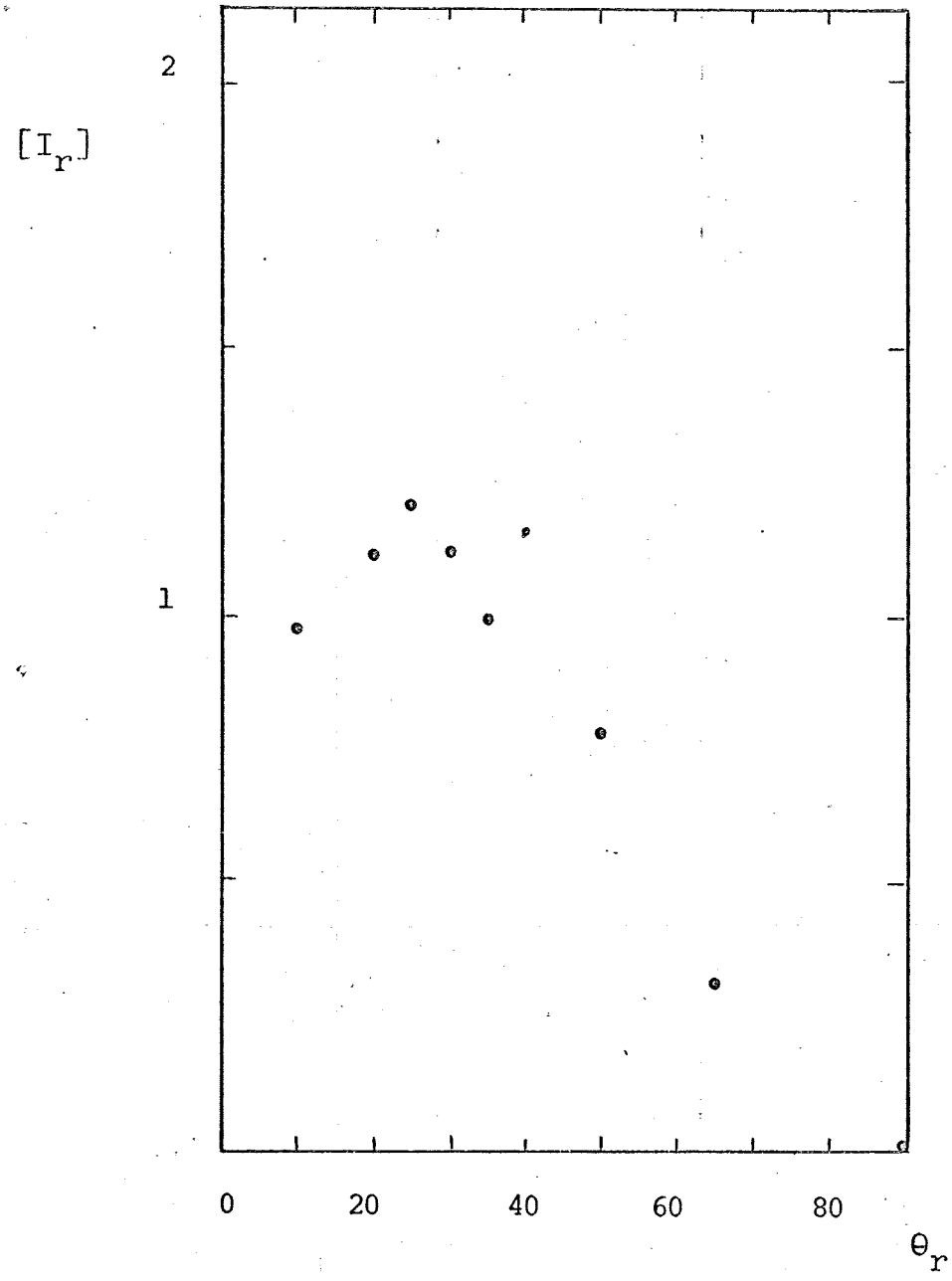

Figure 5.3.6 Argon(300)/Ag(700) II

θ_i	θ_r	τ	α	SF	ET
35		0	-12		290.5-291.3

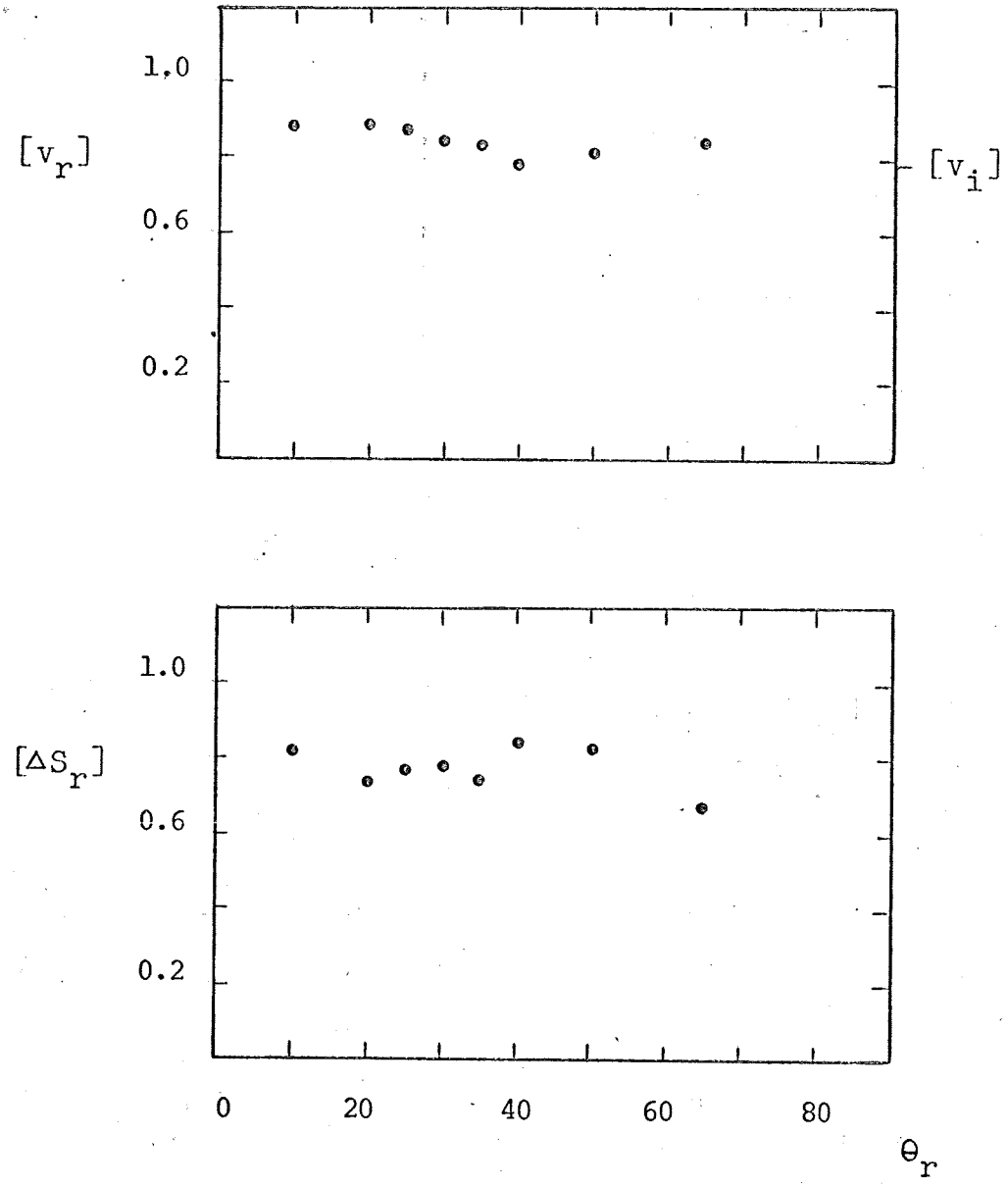

Figure 5.3.6

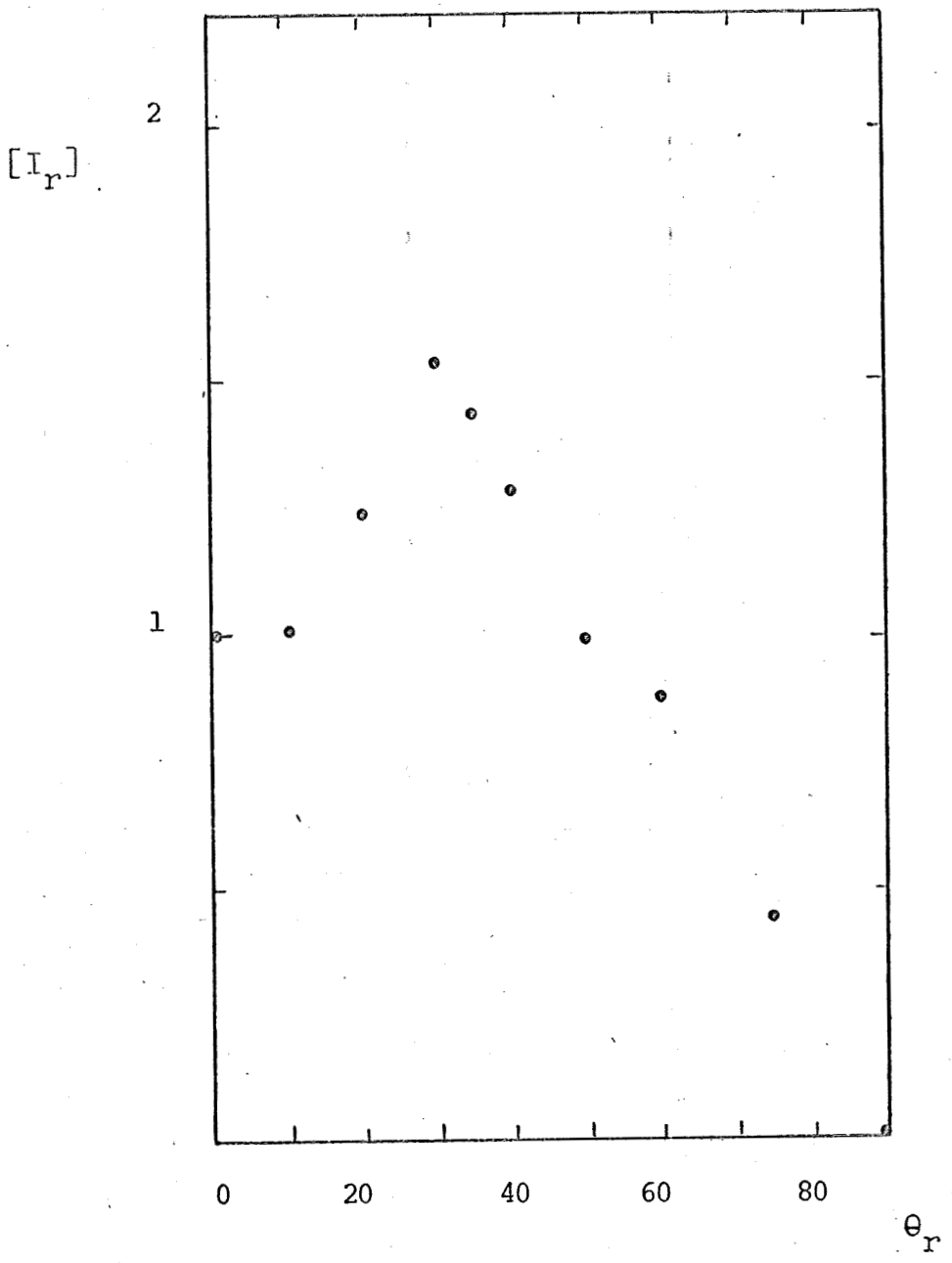

Figure 5.3.7 Argon(300)/Ag(700) II

θ_i	θ_r	τ	α	SF	ET
50		0	-12		289.3-289.8

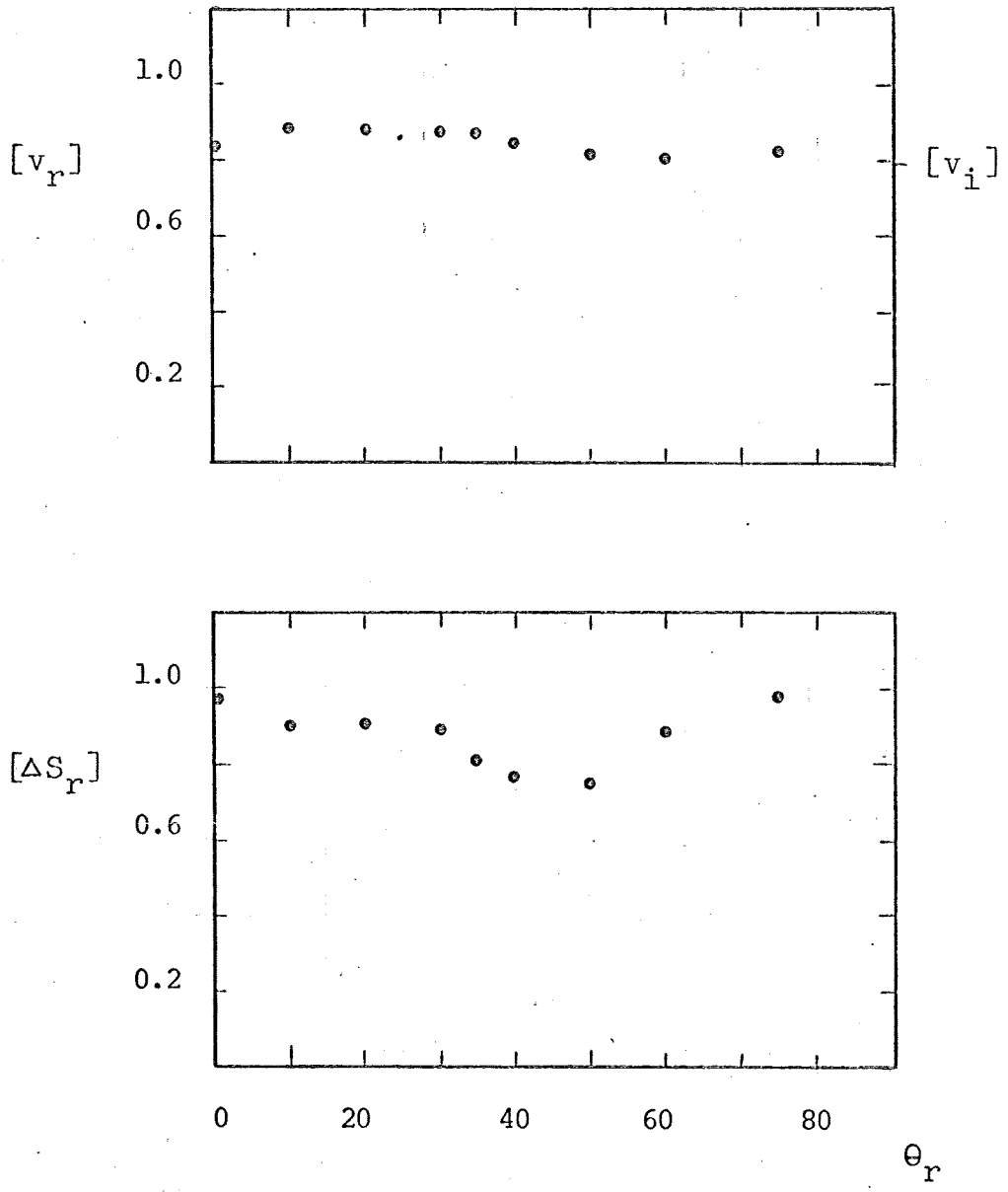

Figure 5.3.7

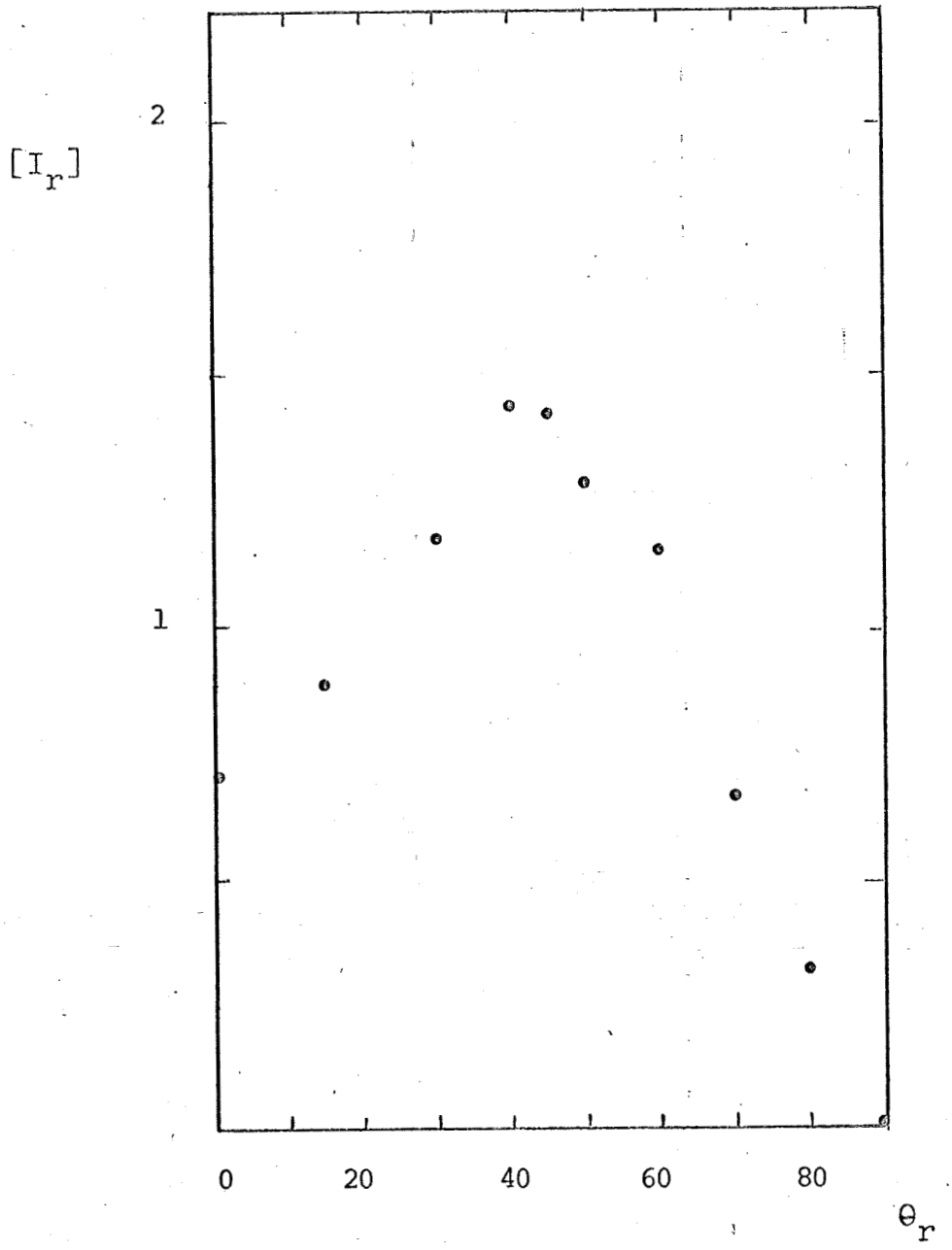

Figure 5.3.8 Argon(300)/Ag(700) II

θ_i	θ_r	τ	α	SF	ET
70		0	-12		290.0-290.5

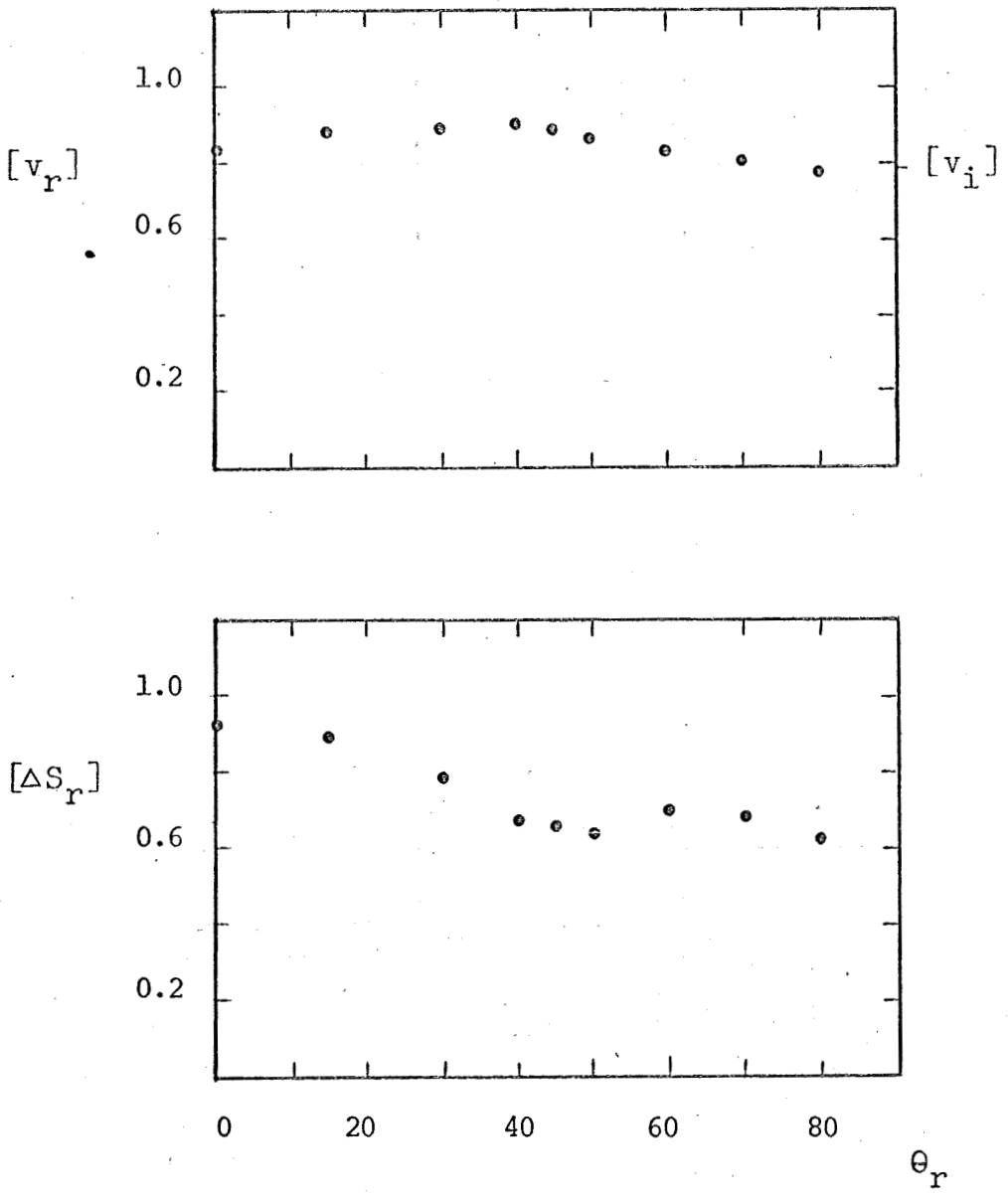

Figure 5.3.8

Equally interesting is the dependence of the subspecular shift upon θ_i. For both surface temperatures, the extent of the subspecular shift increases as θ_i increases, this effect being more pronounced at the lower surface temperature. Figure 5.3.9 presents the subspecular shifts of the intensity maxima for these data and also for data by Bishara [20] and by Saltsburg and Smith [3], all in the range $T_s \approx 600^\circ K$. It is noteworthy that, after this deterioration of its reflectivity, the vapor-deposited surface in its Phase II condition behaves comparably to the mechanically processed surface employed by Bishara. It should be emphasized in this discussion, however, that the obvious random scatter present in the intensity data limits the confidence in the trends shown for the present experiments.

5.4 Temperature Dependence for Helium

Attempts were made to more definitely characterize the effects of changing surface temperature upon the properties of the scattered beams. The data obtained vary in range and completeness due to limitations imposed by other aspects of the experiment. For example, during Phase I the upper temperature limit was set at $600^\circ K$ in

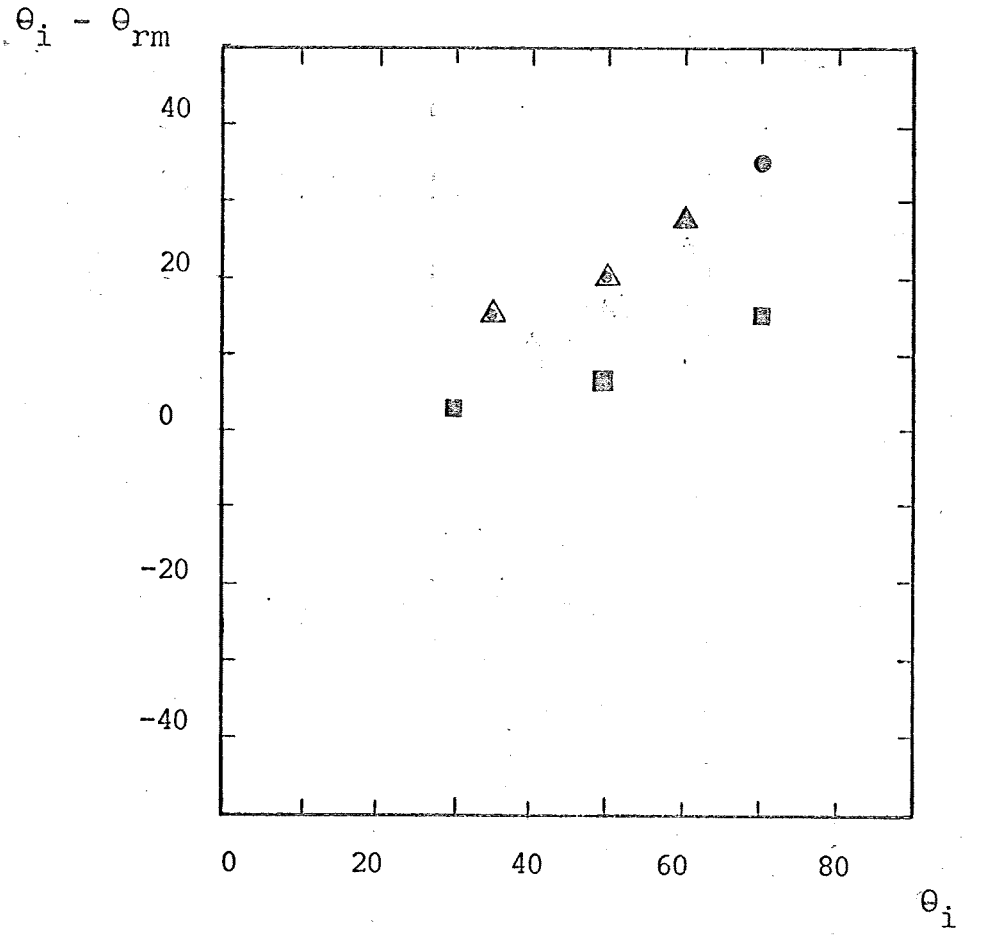

● This experiment, T_s = 600°K

▲ Bishara's data, T_s = 560°K

■ Saltsburg & Smith's data, T_s = 560°K

Figure 5.3.9 Argon(300)/Ag(600) II

θ_i	θ_r	τ	α	SF	ET
		0	-12		284.5-288.5

order to minimize the chance of thermal roughening. In all cases, temperature cycling was restricted to limits compatible with transition to the series of experiments scheduled to follow.

In these experiments, the variations of $[I_r]$, $[v_r]$, and $[\Delta S_r]$ with T_s were observed for helium incident at $\theta_i = 70^\circ$ and scattered in the specular direction by the surface in each of its three phases. It should be noted, in discussing the data, that due to the failure to fit a thermocouple directly to the silver surface, a hysteresis effect is present in the intensity - temperature curves and is observable where points were recorded during both heating and cooling. This hysteresis results from the necessity, due to time limitations, of recording the thermocouple measurements involved while the actual surface temperature was changing. Nevertheless, the data obtained display acceptable trends in a consistent fashion. The full hysteresis loop (displayed in Figure 5.4.2) has been employed in conjunction with previous calibration data to estimate the "true" temperature versus intensity curves accompanying the plotted data points.

Figure 5.4.1 records the dependence of $[I_r]$, $[v_r]$, and $[\Delta S_r]$ upon the surface temperature in the range $400^\circ K \leq T_s \leq 600^\circ K$ for the Phase I surface during one cooling sequence. Note that $[I_r]$ increases initially as

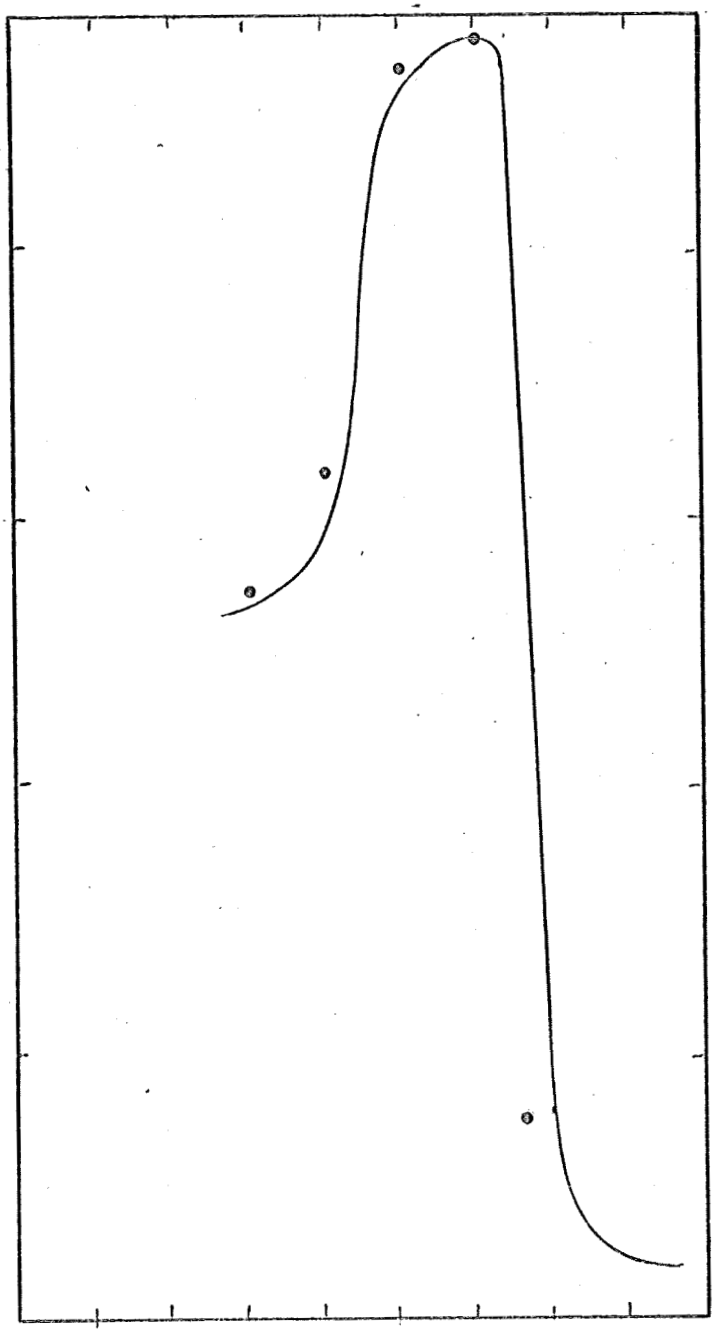

Figure 5.4.1 Helium(300)/Ag( ) I

θ_i	θ_r	τ	α	SF	ET
70	70	0	0		28.8-29.8

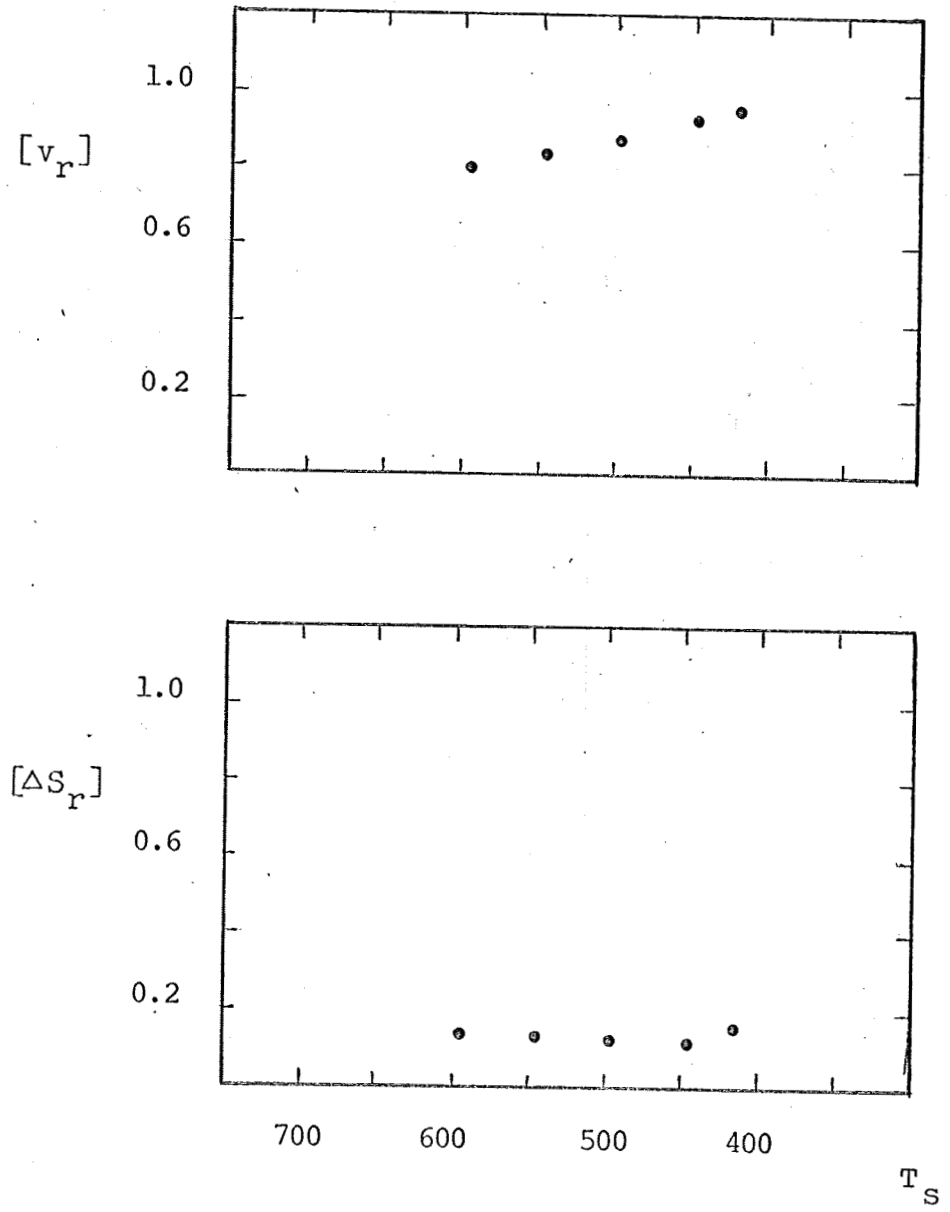

Figure 5.4.1

T_s decreases, then rapidly decreases as T_s drops below about 450°K. This marked decrease of specular intensity with decreasing surface temperature has also been observed by Saltsburg and Smith [3] in the range 470°K - 420°K. It is a reversible function of surface temperature (see Figure 5.4.2) prominent in the first two phases of the present surface. The intensity maximum observed here between 450°K and 480°K was apparently not present in the data of Saltsburg and Smith, however, as they imply that $[I_r]$ for helium scattering is relatively independent of T_s in the range 470°K - 680°K. This variance is likely a result of differences in surface quality or in related experimental conditions such as the aforementioned recording of data without awaiting thermal equilibrium.

It is of interest, however, that there exists a correlation between the intensity maxima observed and minimum values of the speed spread. (This trend is most pronounced in Figure 5.4.2.) The overall low values of the speed spread indicate a predominantly elastic energy exchange at the surface in this "smoothest" phase. The correlation between declining speed spreads and increasing intensities is consistent with expectations for increasingly elastic behavior. The regular increase of $[v_r]$ with decreasing T_s is due totally to the attendant decrease of $\langle v_s \rangle$; the actual magnitude of $\langle v_r \rangle$ remains unchanged and

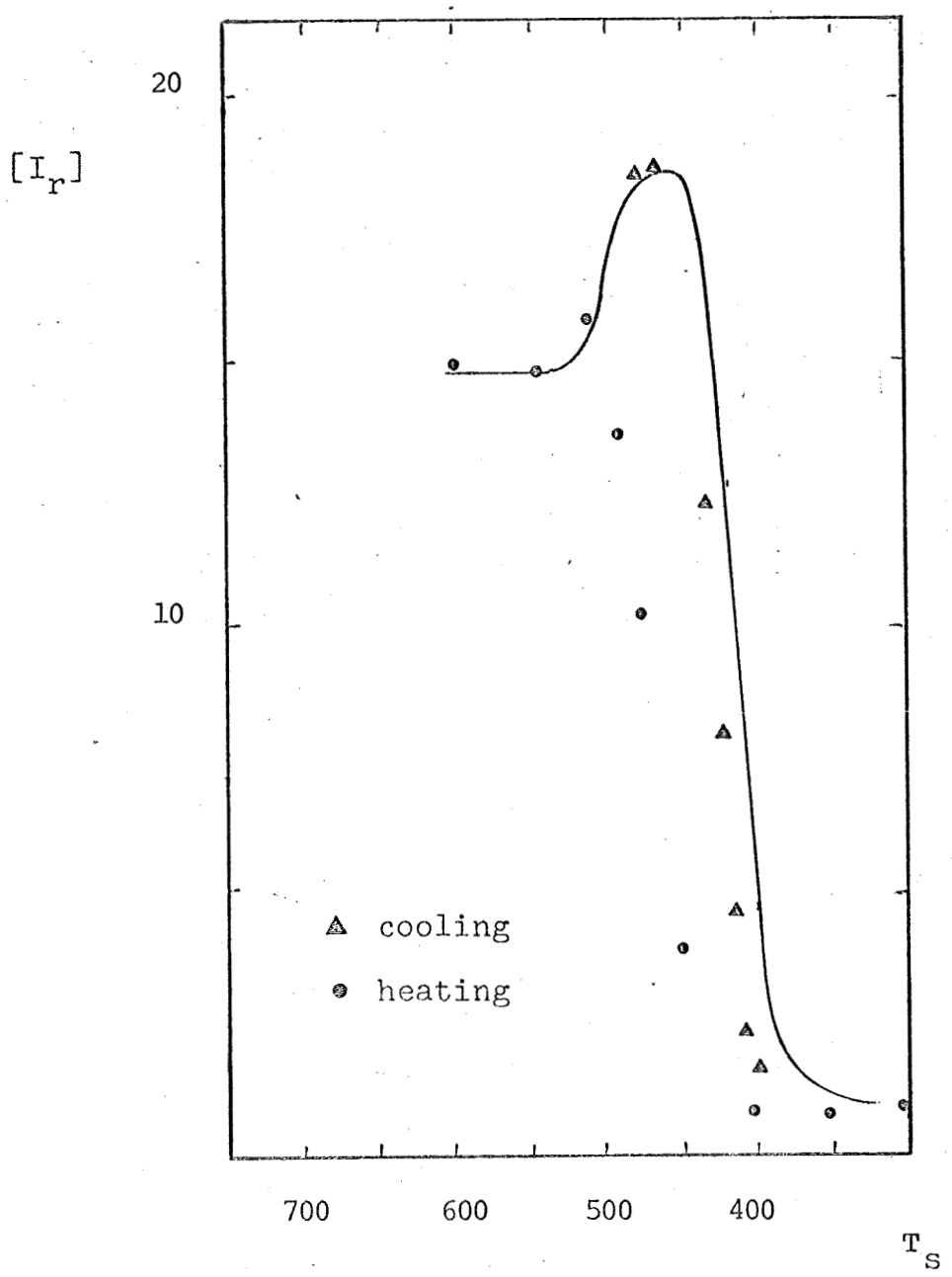

Figure 5.4.2 Helium(300)/Ag( ) II

Θ_i	Θ_r	τ	α	SF	ET
70	70	0	0		166.8-170.3

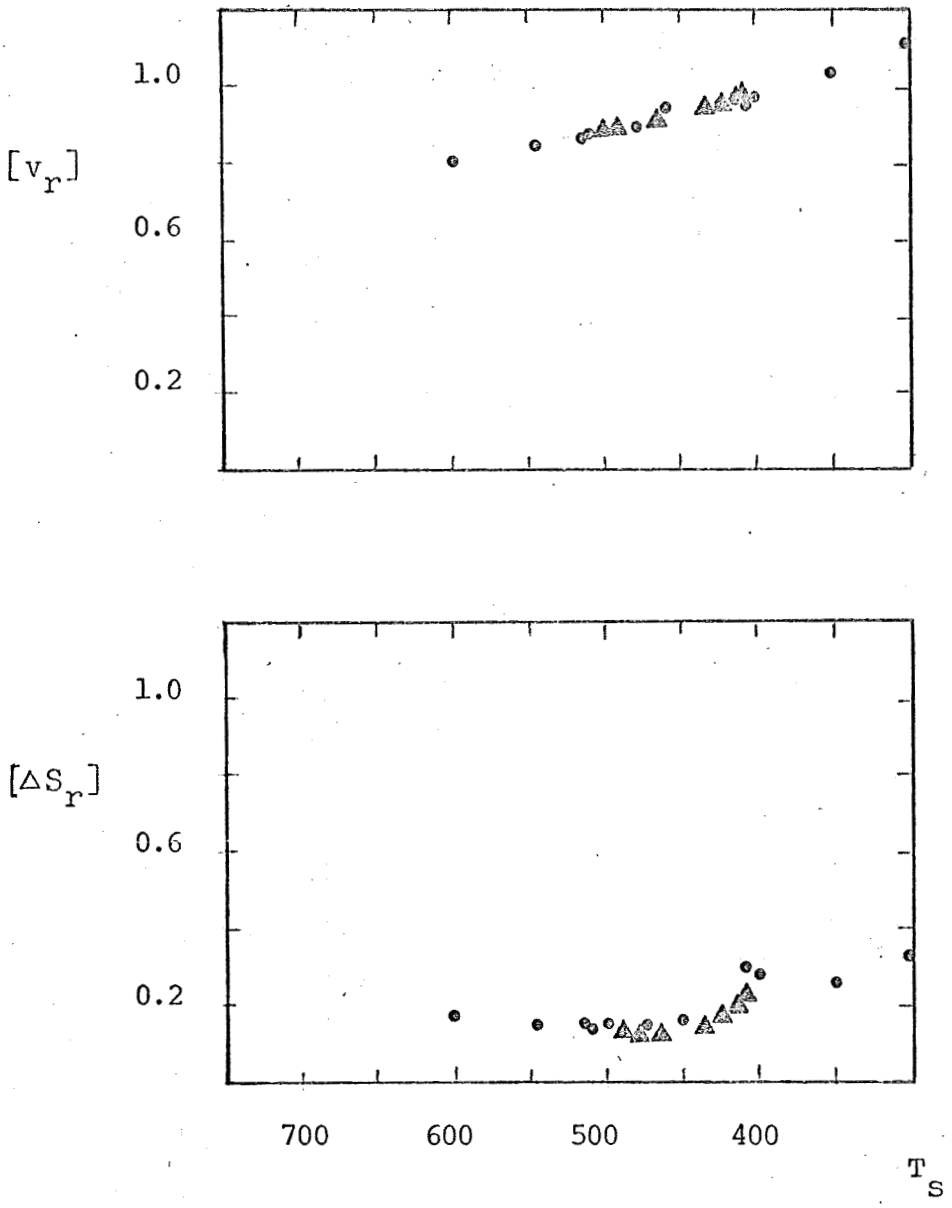

Figure 5.4.2

essentially equal to $\langle v_i \rangle$.

Figure 5.4.2 records a more extensive study performed at the initiation of Phase II. Data are differentiated according to whether they were recorded during the heating or cooling portion of the temperature cycle. As presented, the results clearly display the experimentally induced hysteresis in intensity mentioned previously. This effect is considerably less pronounced in the mean speed and speed spread data. Note the excellent correlation of the region of rapid intensity decline between the two phases and the very similar behavior of both $[v_r]$ and $[\Delta S_r]$. The "aging" process has clearly effected no significant qualitative changes in scattering as a function of surface temperature.

The transition to Phase III, on the contrary, resulted in markedly different behavior of the scattered flux as can be seen in Figure 5.4.3, showing data for the Phase III surface during cooling. The specular intensities recorded are significantly lower throughout the temperature range explored than those seen in either previous phase and the distinct transition "step" in intensity between 450°K and 400°K is absent. Concurrent with the overall decrease in specular intensity is an overall increase in the speed spread. Both intensity and speed spread are devoid of the "structure" previously displayed in the vicinity of the

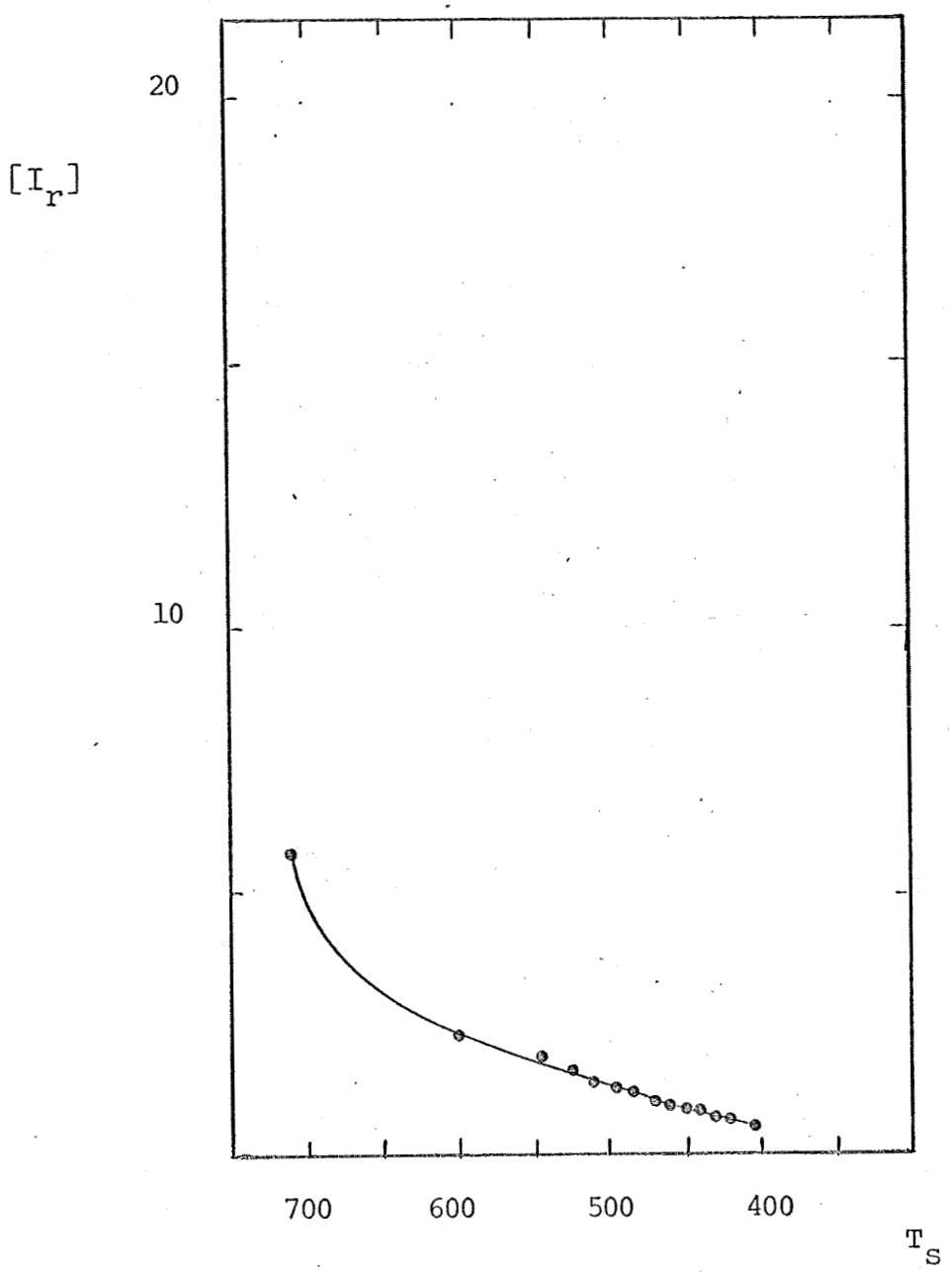

Figure 5.4.3 Helium(300)/Ag( ) III

Θ_i	Θ_r	τ	α	SF	ET
70	70	0	-12		321.3-322.2

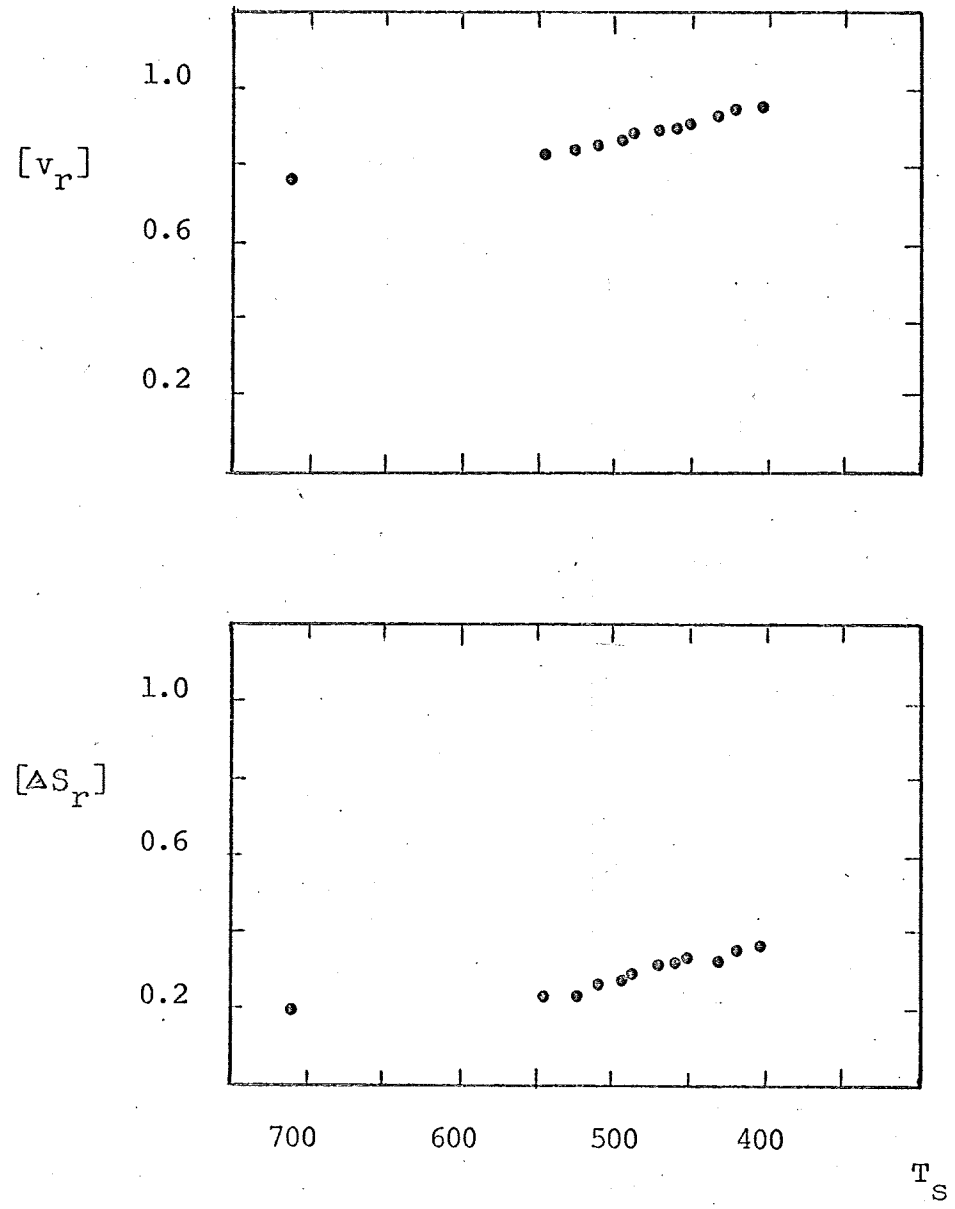

Figure 5.4.3

transition region. Only the normalized mean speed, $[v_r]$, remains virtually unaffected by the phase change, with $\langle v_r \rangle$ still essentially identical to $\langle v_i \rangle$.

In the foregoing data, variations in specular intensity and speed spread have been related to changes in surface temperature and in surface condition. The temperature dependence of these variations is observable in all three phases, but its prominence over a limited temperature range in the first two phases coupled with its reversibility imply that the mechanism involved here is the adsorption of one or more constituents of the background gas. The findings discussed in the following section lend support to this conclusion. On the other hand, the dependence of specular intensity and speed spread upon surface phase is irreversible implying that "aging" in vacuum and, more importantly, excessive heating of the surface effect a permanent change in its topography. This "roughening" of the surface leads to more diffuse and more accommodated scattering and significantly diminishes the extent to which surface temperature controls the respective magnitudes of the specular intensity and speed spread.

5.5 Adsorbed Contaminants

During the course of the experiments, mass spectrometer readings were taken at regular intervals to monitor the background constituents within the test chamber. The most prominent of these are presented in Table 5.5.1 together with their approximate partial pressures in a background of about 2.5×10^{-7} torr.

As mentioned earlier, an attempt was made to determine the principal constituents adsorbed onto the target surface at lower temperatures by cooling the target to $300^{\circ}K$, facing it toward a mass spectrometer[1] set to cycle continuously through the mass range 12-70 amu at a rate of one cycle every 30 seconds, and then heating it rapidly to about $800^{\circ}K$. The entire procedure took 16 minutes (32 cycles).

A necessary sacrifice for this rapid cycling, however, was an attendant loss of sensitivity by the spectrometer. As a result both of this sensitivity loss and of background noise levels, only four of the indicated constituents (H_2O, N_2 / CO, CO_2, and OH) could be profitably monitored. (The spectrometer was capable of a nominal sensitivity of 10^{-10} torr.) During the course of heating, peaks for each of the four observed constituents were

---

[1] Aerovac AVA - 1

Table 5.5.1

Principal Background Constituents in the Test Chamber

Gas	Partial Pressure ($\times 10^{-9}$ torr)
H_2O	3.8
N_2/CO	2.6
CO_2	2.3
OH	2.1
O_2	1.7

Note: Total Pressure $\approx 5 \times 10^{-7}$ torr. The partial pressures recorded are nominal values.

measured to determine when and to what extent desorption of any one of them might occur. Indications were that the N_2 / CO signal doubled its value at about 400°K and that H_2O increased its value by about 50% near 500°K. A smaller increase in the value of CO_2 seemed to occur between these two temperatures but the amount of the increase relative to the system's noise leaves some doubt as to the validity of this observation.

Due to the facts that a) the mass spectrometer tube sat some 60 cm. from the target and b) the two were separated by the relatively opaque spinning chopper wheel, the signals observed were probably representative of the average background constituents and not of those boiling directly off the target. Further, since the target heater block was hotter than the target and, together with its associated radiation shielding, presented a larger surface area for desorption, it is probable that some, if not most, of the desorbed gases came from this source. Nevertheless, the results are interesting and since CO and H_2O are known to be prevalent background constituents in any steel vacuum chamber, it would appear that adsorption/desorption of CO is the mechanism responsible for the reversible transition of intensity in the surface temperature range 400°K - 450°K.

CHAPTER 6

COMPARISON AND SUMMARY OF RESULTS

6.1 Comparison with Results of Previous Studies

The purpose of this section is to set the data presented in the preceding chapter in some perspective relative to data obtained by other experimenters. Of particular interest is an evaluation through these data of differences in the condition of test surfaces from laboratory to laboratory.

Data obtained by scattering helium from epitaxially grown (111) silver surfaces have been recorded by Saltsburg and Smith [3] and by Saltsburg, Smith and Palmer [23] of General Atomic; by Romney [5] of Princeton; and by the author. In order to compare the intensity distributions on a quantitative basis, an attempt has been made to plot these data on a common scale. Inspection of the available scattering data for helium incident at 50° onto targets in the vicinity of 580°K revealed that all of the principal plane intensity distributions recorded by any one laboratory displayed an essentially constant intensity at $\theta_r = 20^{\circ}$ regardless of changes in the shape factor of the distribution

due to aging or other considerations. Consequently, the desired common scale was achieved by matching the intensities at $\theta_r = 20^o$ for the four data sets presented. While this is a reasonable procedure on physical grounds, it is estimated that an error of as much as ± 50% is still possible in the relative magnitudes assigned the different data sets.

Figure 6.1.1 displays principal plane intensity distributions from four separate experiments for room-temperature helium incident at $\theta_i = 50^o$ onto epitaxially grown (111) silver surfaces with $550^oK \leq T_s \leq 600^oK$. The least lobular distribution shown is from Romney[1] [5] and was recorded some 117 minutes after deposition. Following in order of increasing lobularity are the distribution recorded in the present experiments some 240 minutes after deposition and, respectively, the low and high resolution distributions recorded by Saltsburg, Smith, and Palmer [23] on "freshly deposited" films (assumed less than an hour old). The differences in overall angular resolution due to the combined effects of finite incident beam divergence and finite angular resolution of the detector are listed in the figure. Clearly the differences in the distributions are partially attributable to differing resolutions. Nevertheless, it appears that the surfaces employed by the group at

---

[1]Romney used a density-sensitive detector; to the known extent that $\langle v_r \rangle$ is independent of scattering direction, it is appropriate to interpret his helium data as intensity distributions.

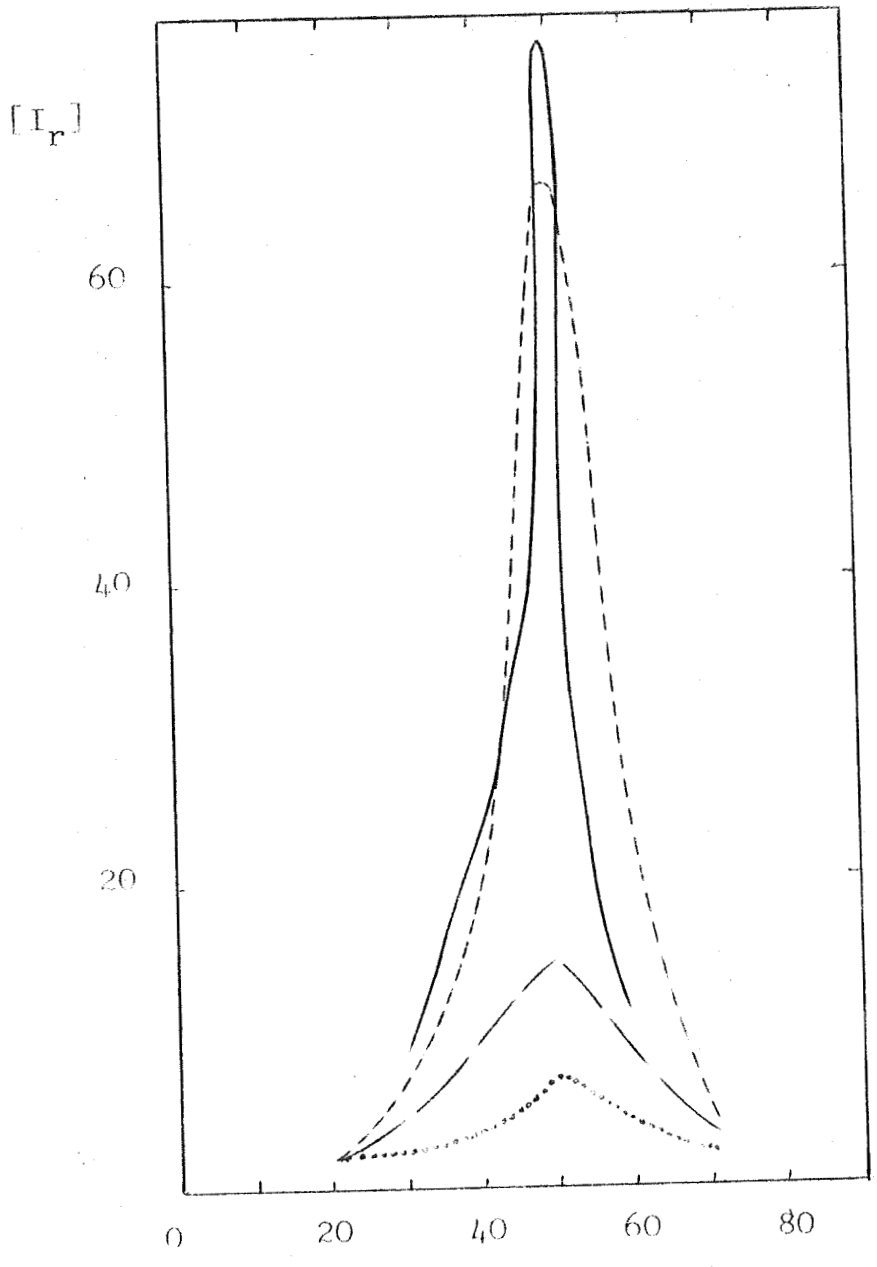

Source of Data	Angular Uncertainty
——— Saltsburg,et al.[23]	± 1°
- - - - - - Saltsburg,et al.[23]	± 4°
— — This experiment.	± 2°
..... Romney.[5]	±10°

Figure 6.1.1 Helium(~300)/ Ag(550-600°K), $\theta_i = 50^\circ$

General Atomic are significantly smoother than those employed either by Romney or by the author.

A partial comparison of data for the intensity distribution in the transverse specular plane corresponding to the data in Figure 6.1.1 is shown in Figure 6.1.2. The only data available were those from the high resolution work of the General Atomic group and the present study. Both transverse distributions display angular widths measured at half-maximum intensity that are narrower than those of the corresponding principal plane distributions in Figure 6.1.1. Their relative shapes likewise appear consistent with the corresponding principal plane data.

The decay of surface reflectivity as a function of time during the first several hours after deposition has been studied by Romney. One measure of this reflectivity is the intensity at the specular angle. These data have been extracted from Romney's results for the case of room-temperature helium incident at $\theta_i = 50^\circ$ upon a $573^\circ K$ silver surface over a period of several hours, and are presented in Figure 6.1.3. Also presented in this figure are reference points obtained under similar conditions for specularly directed helium beams observed by Saltsburg and Smith, [3], and by the author. The data presented are scaled relative to one another in the manner described for Figure 6.1.1. It should be noted that between the two points extracted from

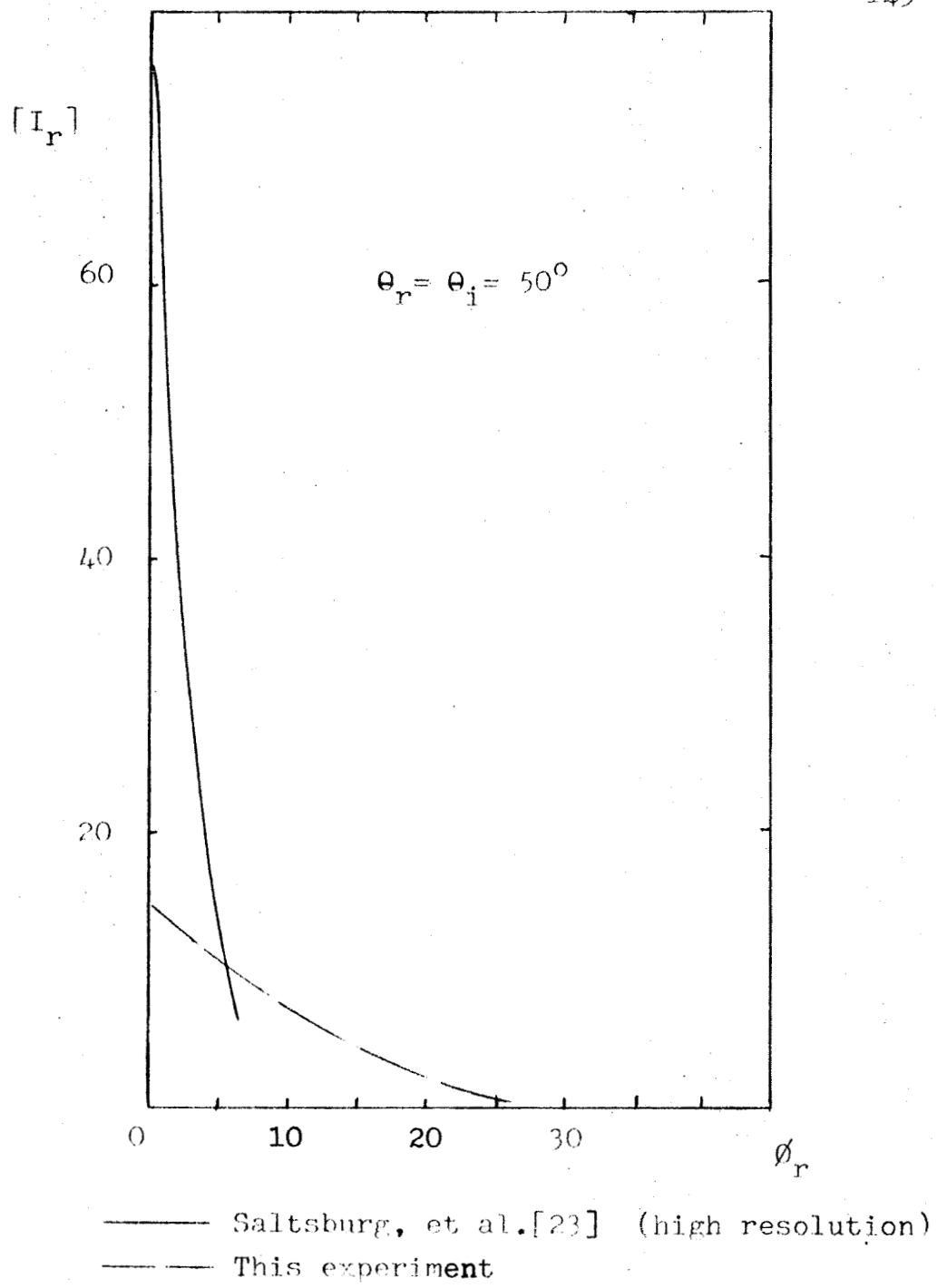

Figure 6.1.2 Helium(~300)/Ag(550-600°K)

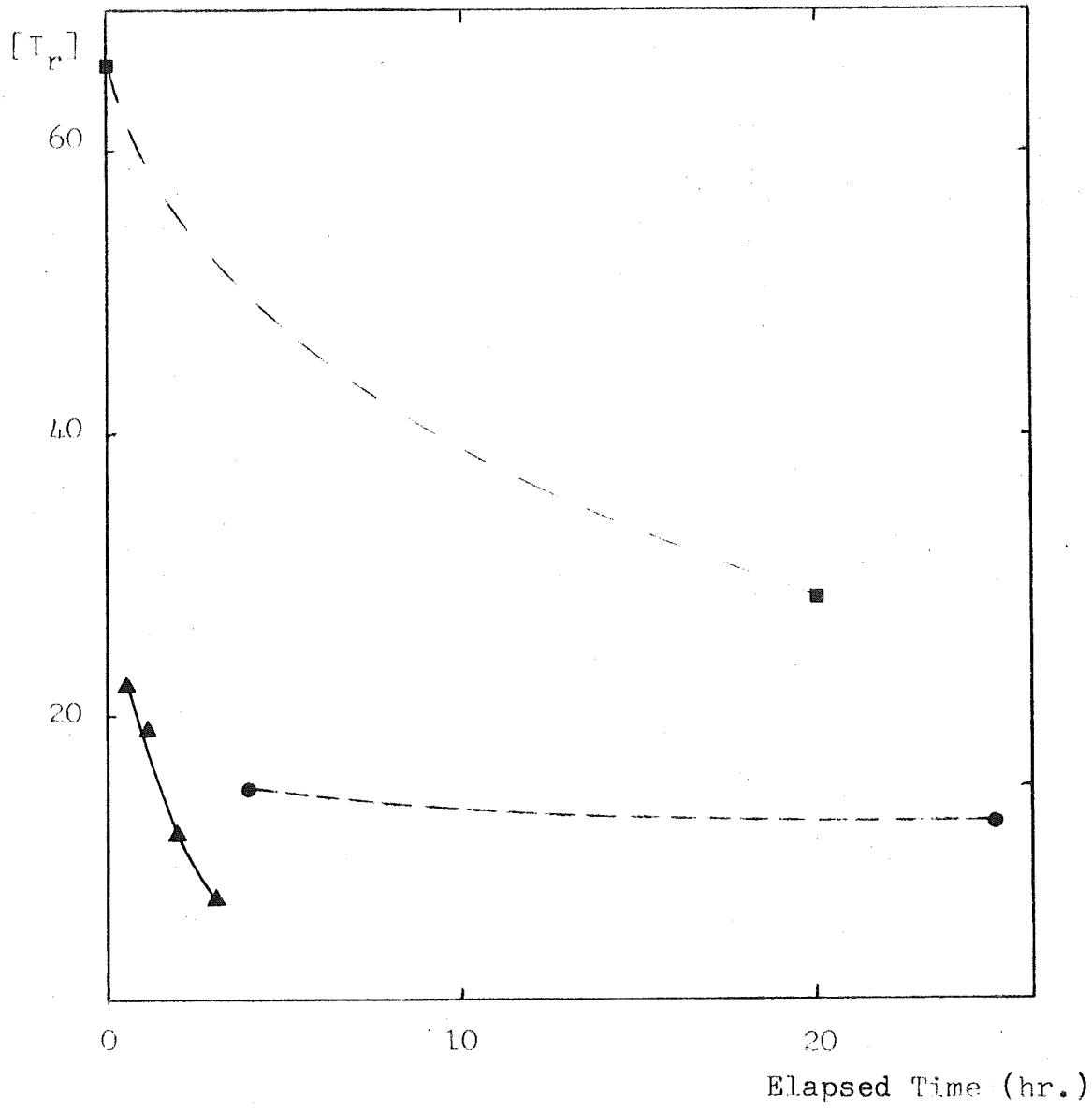

Figure 6.1.3 Helium(~300)/Ag(550-600°K)

Study of Decay in Specular Intensity as a Function of Time Elapsed Since Deposition. ($\theta_i = 50^\circ$)

Saltsburg and Smith's data, the target experienced some 15 hours at $T_s \approx 300^{\circ}K$ at a pressure of 100 μ followed by 5 hours at $T_s \approx 560^{\circ}K$ at a pressure of 5×10^{-7} torr. The relative intensities assigned these points rely explicitly upon the assumption that intensities can be safely matched at $\theta_r = 20^{\circ}$. The data recorded by both Romney and the author are for constant temperature surfaces continuously under vacuum at a pressure near 5×10^{-7} torr. These latter data suggest that the aging of the surface, by whatever process may be involved, is essentially complete after the first four hours following deposition. The statement by Saltsburg and Smith that: "Only after overnight exposure to the atmosphere was the subsequent scattering found to be seriously affected."[1] is not necessarily in contradiction with these results but may indicate that their system is freer of contaminants than systems yielding more "time-dependent" results.

The principal plane scattering distributions for argon incident at $\theta_i = 50^{\circ}$ onto epitaxially grown (111) silver surfaces in the range $T_s = 550^{\circ}K - 600^{\circ}K$ are shown in Figure 6.1.4 for data obtained by Saltsburg and Smith [3] with "fresh" surfaces and by the author with a Phase II surface at 285 hours elapsed time. Also included are comparable data obtained by Bishara [20] with a polished

---

[1] Saltsburg and Smith, "Molecular Beam Scattering from the (111) Plane of Silver," The Journal of Chemical Physics, p. 2176, Sept. 15, 1966.

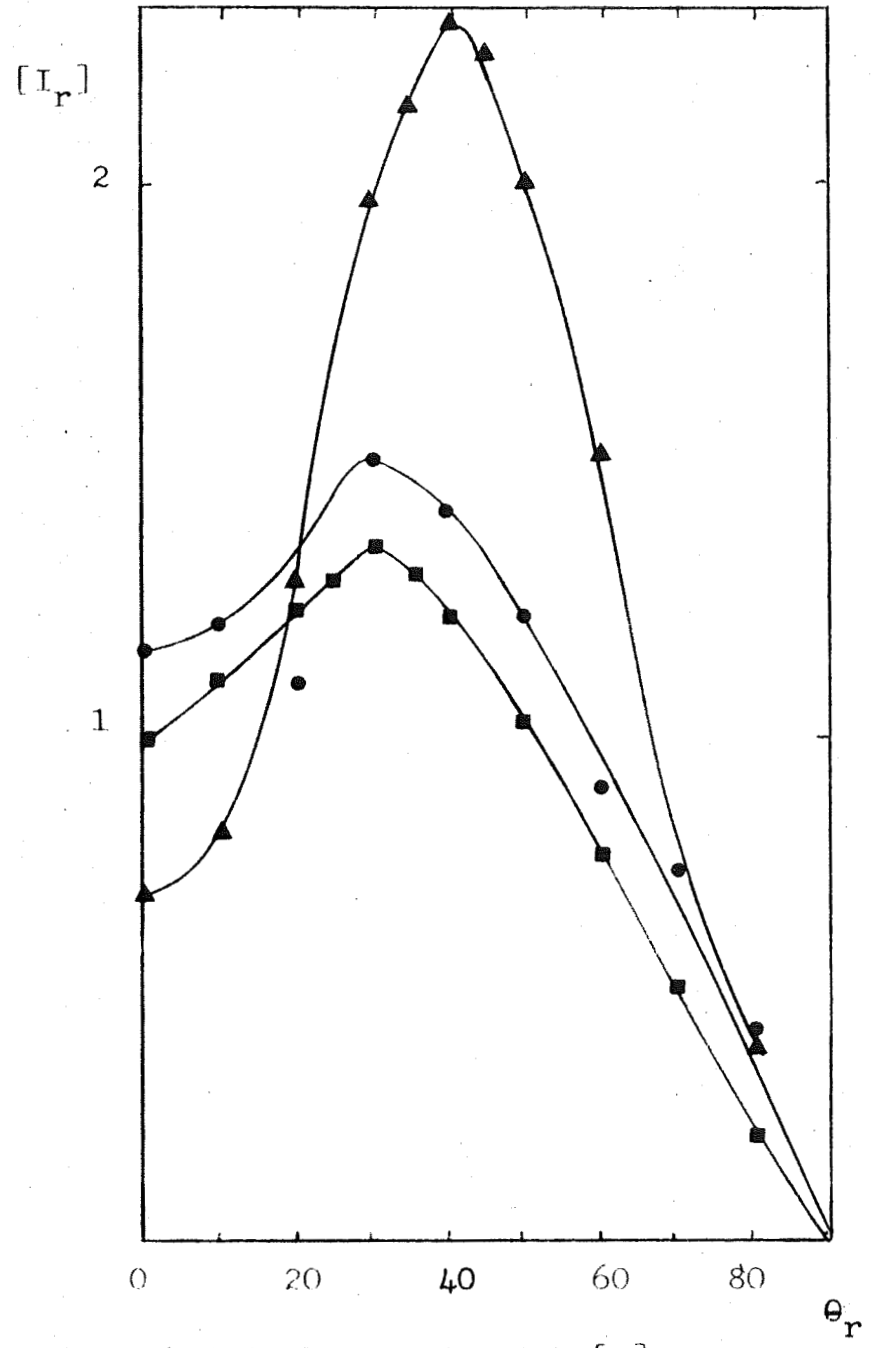

Figure 6.1.4 Argon(~300)/Ag(550-600°K)
Comparison of Principal Plane
Scattering for $\theta_i = 50^\circ$

(111) silver surface. As in previous figures, best-estimates of scale factors have been employed to enable some measure of comparison on a quantitative basis. It is obvious that the Saltsburg and Smith surfaces are considerably more reflective than that studied by the author for argon scattering just as they were for helium scattering. On the other hand, the Phase II surface appears very similar to the polished surfaces used by Bishara. Since it is known [20] that Bishara's surfaces had irregularities on the order of 0.1 μ in height, the data would indicate comparable roughness for the present surface. It is also observed that the less reflective a surface the more "subspecular" ($\theta_{rm} < \theta_i$) its scattered intensity distribution tends to be.

The comparison between the surface employed by Bishara and that studied here can be continued to include the speed spread, $[\Delta S_r]$, and the mean speed $[v_r]$. Figure 6.1.5 displays such a comparison. Note the very similar trends in behavior of both $[\Delta S_r]$ and $[v_r]$ between the two data sets. The consistently lower values of $[v_r]$ for the epitaxially grown surface appear to indicate a real difference in the thermal accommodation of the two surfaces. The relation of $[v_r]$ to $[v_i]$ for the present data implies lower thermal accommodation. This indication is supported by the consistently lower values of $[\Delta S_r]$ also observed for the epitaxial surface.

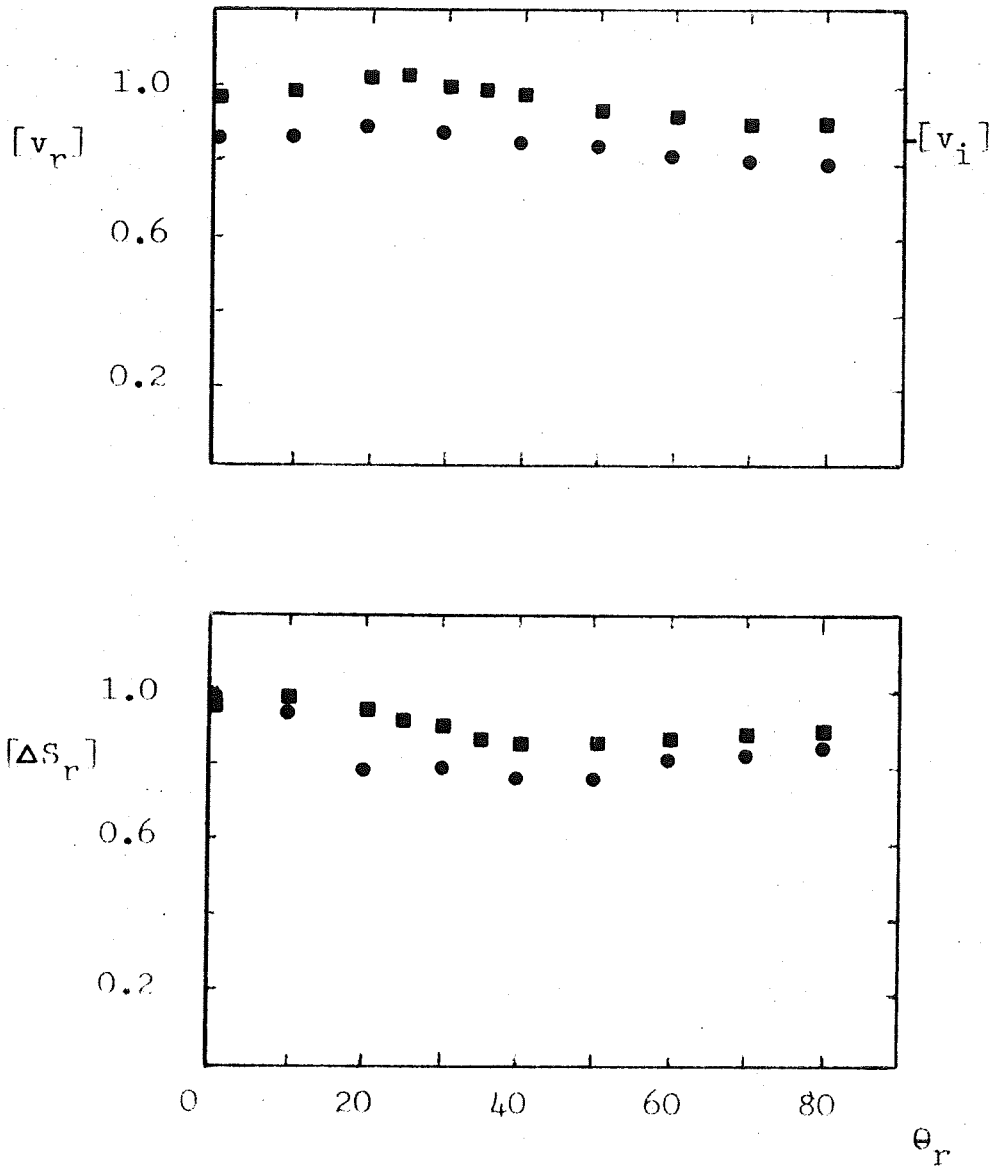

Figure 6.1.5 Argon(300)/Ag(550-600°K)
Comparison of Principal Plane
Scattering for $\theta_i = 50^\circ$

6.2 Summary of Findings

In view of the length of the preceding chapter, a brief summary of the more prominent characteristics and more consistently observed qualitative trends is advisable. Where possible, for compactness, these trends will be displayed in terms of the simple functional notation:

$$\frac{\partial(\text{Property})}{\partial(\text{Variable})} \gtrless 0$$

Room temperature helium scattered from the hot (500 - 700°K) silver target consistently displays its maximum intensity and minimum speed spread at the specular angle. Intensity decreases sharply upon leaving the specular direction in both principal and transverse planes (somewhat more so in the latter). The spread in speeds increases slightly on proceeding transversely away from the principal plane but its most noticeable increase occurs with decreasing θ_r in the principal plane over the range $0 \leq \theta_r \leq \theta_i$. For $\theta_r > \theta_i$, the speed spread rises slightly above its value at the specular, then levels off. The mean speed of the scattered helium atoms displays only slightly lower values within the principal plane than in the observed transverse planes. There is also a very slight decrease in mean speed with increasing θ_r in the principal plane.

Observations of helium atoms scattered in the specular direction for all of the data obtained reveal the following dependence upon the incident angle ($30^{\circ} \leq \theta_i \leq 70^{\circ}$):

$$\frac{\partial [I_r]}{\partial \theta_i} > 0$$

$$\frac{\partial SF}{\partial \theta_i} > 0$$

$$\frac{\partial [\Delta S_r]}{\partial \theta_i} < 0$$

$$\frac{\partial [v_r]}{\partial \theta_i} \approx 0 .$$

The trends listed above indicate that the scattering becomes increasingly "angle-coherent" and "speed-coherent" as θ_i increases. The mean energy exchange, because it is essentially zero, appears independent of θ_i.

The quantities $[I_r]$, $\langle v_r \rangle$, and $[\Delta S_r]$, as measured for helium with $\theta_r = \theta_i = 70^{\circ}$, display the following dependance upon the surface temperature:

Phases I & II:

$$\frac{\partial [I_r]}{\partial T_s} - \frac{\partial [\Delta S_r]}{\partial T_s} \begin{cases} > 0 & 415^\circ \leq T_s \leq 460^\circ K \\ \approx 0 & 300^\circ \leq T_s < 415^\circ K \\ \approx 0 & 460 < T_s \leq 720^\circ K \end{cases}$$

$$\frac{\partial \langle v_r \rangle}{\partial T_s} \approx 0 \left(\begin{array}{l} \langle v_s \rangle \sim T_s^{\frac{1}{2}} \text{ and, therefore,} \\ \dfrac{\partial [v_r]}{\partial T_s} < 0 \text{ is observed.} \end{array} \right)$$

Phase III:

$$\frac{\partial [I_r]}{\partial T_s} > 0$$

$$\frac{\partial [\Delta S_r]}{\partial T_s} < 0$$

$$\frac{\partial \langle v_r \rangle}{\partial T_s} \approx 0$$

For $T_s < 460^\circ K$ (approximately), increasing adsorption of background gases on the target surface with decreasing surface temperature is the apparent cause of a transition

from highly lobular to quite diffuse scattered-intensity distributions. Still, the small values of $[\Delta S_r]$ compared to unity and the fact that $[v_r]$ is at all times essentially equal to $[v_i]$ indicates conclusively that this diffuse-like scattering is far from that attributable to the adsorption and reemission of helium atom.

With increasing surface roughness (i.e. with higher phase number) it is found that the maximum observed intensity, $[I_{rm}]$, for helium decreases as does the shape factor, SF, while the speed spread, $[\Delta S_r]$, increases at essentially all scattering directions and the absolute mean speed, $\langle v_r \rangle$, again remains essentially constant and equal to $\langle v_i \rangle$, the mean speed of the incident atoms.

The scattered intensity distributions for room temperature argon, when compared to those for helium at the same incident energy, the same surface conditions, and similar angles of incidence are far less lobular. The intensity maxima for argon, furthermore, are shifted toward the normal by an amount dependent upon the incident angle such that

$$\frac{\partial (\theta_i - \theta_{rm})}{\partial \theta_i} > 0$$

where θ_{rm} is the direction of the intensity maximum.

The magnitudes of the intensity maxima for argon were observed in the present experiment to be virtually independent of the incident angle in the range $35^{\circ} \leq \theta_i \leq 70^{\circ}$. This observation agrees substantially with the findings of Bishara [20] (see his Figure 5.2.1) but is in conflict with the distinct decrease of maximum scattered intensity with increasing incident angle observed by Saltsburg and Smith [3] (see their Figure 9). It appears likely, in light of previous discussions comparing the reflectivity of the various surfaces involved, that this difference in behavior is related in a fundamental way to the differences in cleanness and topography between the surfaces used by Saltsburg and Smith, on the one hand, and those used by both Bishara and the author, on the other.

The normalized mean speed of the scattered argon atoms displays a more pronounced variation with θ_r than is observed with helium. It rises to a maximum value in the principal plane between the surface normal and the direction of the intensity maximum, then decreases nearly monotonically with increasing θ_r. Variation of the surface temperature in the range $600^{\circ}K \leq T_s \leq 700^{\circ}K$ effects no qualitative change in this behavior.

Due to the presence of significant amounts of noise in the detector electronics, the speed spread for argon presents a less regular dependence on θ_r than does either $[I_r]$

or $[v_r]$. The only consistent behavior noted is a tendency toward a minimum value occurring in the range $\theta_{rm} \leq \theta_r \leq \theta_i$. As the incident angle increases, this minimum value decreases while the value near the normal remains approximately the same. Increasing surface temperature generally effects a decrease in this minimum value for all incident angles. Finally, by way of comparison, the intensity-weighted average of $[\Delta S_r]$ over the exit hemisphere for argon is about twice that observed for helium.

The scattered argon beams consistently exhibit a significant diffuse (cosine) intensity component (see, for example, Figure 5.2.1a). The mean speeds measured near the surface normal, where diffuse scattering dominates, exhibit only moderate thermal accommodation with the surface, however. This fact implies that the argon atoms, like the helium atoms, do not undergo adsorption followed by reemission in any large fraction of their encounters with the surface.

6.3 Concluding Remarks

In Section 6.1 an effort was made to compare the (111) silver surfaces employed respectively by the General Atomic group, by Romney, by Bishara, and by the author in terms of their relative scattering behaviors. The crystal-

lographic orientation of each of these surfaces was carefully established upon removal from vacuum by means of Laue and, in some cases, electron diffraction techniques. To the extent that can be determined from the data available, all of these surfaces do display qualitatively similar scattering properties, as would be expected. It is equally evident, however, that their quantitative behaviors, as measured by such criteria as intensity ratios between selected scattering angles or the shape factors previously discussed, differ considerably. Certainly part of this difference is attributable to the adsorption of various amounts and kinds of background contaminants both during and after the deposition process. This problem is primarily a function of the individual experimental apparatus. In addition, however, such factors as substrate temperature during deposition and the rate of deposition itself appear to be more critical than initially anticipated in determining the scattering properties of a given surface. The condition of the substrate itself is, of course, of primary importance. All of the above are details that the individual investigator must carefully monitor in order to optimize the scattering properties of his surface.

It is clear from the results obtained by the group at General Atomic that once techniques are perfected a given laboratory can consistently generate surfaces of uniform

quality. It is also evident that the simple criterion of having achieved epitaxy in the desired orientation is insufficient to assure that the surface thus obtained is necessarily "identical"(or even comparable) to other epitaxial surfaces of the same orientation grown on the same substrate material. To enhance the ability of the experimenter to determine which surfaces employed by other laboratories are sufficiently similar in scattering properties to his own to justify comparison or extension of his observations, therefore, it would be heloful to establish a simple set of "standard" scattering distributions selected so as to serve as virtual "fingerprints" of an individual surface. With the aid of such a device, the comparison of data from different sources would be simultaneously simplified and made more reliable. In addition, it would enable the experimenter interested in confirming previously obtained results to determine from the beginning the suitability of a given deposit for this purpose. Since no means of examining surface topography prior to experimentation is available for vapor-deposited surfaces analagous to the shadow or microscopy techniques applicable to surfaces processed mechanically from bulk samples, the gauging of surface smoothness directly in terms of selected scattering properties could provide an alternative means of obtaining similar information in situ.

Initially, vapor-deposited single-crystal surfaces

were selected as offering the greatest promise for observing diffraction from silver by virtue of their relative freedom from adsorbates and anticipated superior smoothness. When diffraction effects were not observed in this experiment, the surface was examined for azimuthal misalignment of the crystallites, since a sufficiently large defect of this type would effectively eliminate the probability of observing diffraction. It was determined, however, that this misalignment was on the order of $\pm 1^{o}$ at most. Consequently, the absence of observed diffraction effects indicates either that such effects are indeed absent from the interaction or else that they are simply too weak to be detected with the present apparatus and techniques.

As regards surface smoothness, the expected results were more fully realized. By way of comparison, photomicrographic and shadow casting techniques indicated that the target face employed by Bishara, which was cut and polished from a bulk crystal, displayed a surface topography characterized by hillocks typically 0.5 μ apart and 0.1 - 0.2 μ high prior to the start of the experiments. By the completion of the experiments thermal faceting had effected an increase in these dimensions to 20 - 40 μ and 10 - 20 μ respectively. In sharp contrast, the deposited surface studied herein, when examined at the termination of experiments (i.e. in its roughest state), displayed as its most prominent surface irregularities cleavage steps averaging less than 0.1 μ high.

Irregularities in the various step planes were proportionately smaller over most of the surface. Since the majority of tractable analyses performed on gas-surface interactions are predicated upon the existence of a scattering plane, the enhanced smoothness of deposited surfaces makes their use preferable in experiments intended to test theoretical predictions.

In addition to this significant superiority in terms of surface smoothness, epitaxially grown surfaces provide an opportunity for future research of a type that would be difficult at best to duplicate with target surfaces of any other type. For example, one can, in principle, deposit and scatter from one surface (say, silver) then deposit a second surface over the first (for example, gold) and scatter from it, thus obtaining a comparison of the scattering properties of two different single-crystal metals whose surface topographies are assured to be virtually identical. Indeed, with the present apparatus, it is possible, assuming a combination of surfaces that may serve interchangeably as substrates for each other, to then grow the initial crystal over the second as a means of establishing the reproducibility of the data. Finally, the adaptation of a LEED system to the test chamber so as to enable continuous, in situ monitoring of the scattering surface will provide the opportunity for detailed study of surface crystallography

both during deposition and throughout subsequent scattering experiments. In this manner, some explanation of such phenomena as the development of the polycrystalline region on the present surface may be forthcoming.

BIBLIOGRAPHY

1. Smith, J. N., Jr., "Interactions Between Hydrogen and Oxygen Atoms and Surfaces," General Atomic Report GA - 7467, San Diego, California (October 1966).

2. Smith, J. N. and H. Saltsburg, "Atomic-Beam Scattering from Epitaxially Grown Gold Films," J. Chem. Phys. 40, 3585 (1964).

3. Saltsburg, H. and J. N. Smith, Jr., "Molecular-Beam Scattering from the (111) Plane of Silver," J. Chem. Phys. 45, 2175 (1966).

4. Alcalay, J. A. and E. L. Knuth," Experimental Study of Scattering in Particle-Surface Collisions with Particle Energies on the Order of 1 ev," Rarefied Gas Dynamics, N. Y., Academic Press, supplement 4, volume 1, 253 (1967).

5. Romney, M. J., "Molecular Beam Scattering of Argon from the (111) Plane of Silver at Hyperthermal Energies," Ph.D. Dissertation, Princeton University (1969).

6. Smith, J. N., Jr., and H. Saltsburg, Molecular Beam Scattering from Solid Surfaces, "Fundamentals of Gas Surface Interactions, N. Y., Academic Press, 370 (1967).

7. Hurlbut, F. C., "Current Developments in the Study of Gas-Surface Interactions," Rarefied Gas Dynamics, N. Y., Academic Press, supplement 4, volume 1, 1 (1967).

8. Stickney, R. E., "Atomic and Molecular Scattering from Solid Surfaces," Advances in Atomic and Molecular Physics, D. R. Bates and I. Estermann, eds., N. Y., Academic Press (1967).

9. Knuth, E. L., "Supersonic Molecular Beams," Appl. Mech. Rev. 17, 751 (1964).

BIBLIOGRAPHY (Continued)

10. Scott, P. B., P. H. Bauer, H. Y. Wachman and L. Trilling, "Velocity Distribution Measurements by a Sensitive Time of Flight Method," Rarefied Gas Dynamics, N. Y., Academic Press, supplement 4, volume 2, 1353 (1967).

11. Hagena, O. F., "Velocity Distribution Measurements of Molecular Beams Scattered from Solid Surfaces," Appl. Phys. Letters 9, 385 (1966).

12. Pashley, D. W., "The Observation of Dislocations in Thin Single Crystal Films of Gold Prepared by Evaporation," Phil. Mag. 4, 324 (1959).

13. Pashley, D. W., "The Study of Epitaxy in Thin Surface Films," Advan. Phys. 5, 173 (1956).

14. Jaeger, H., P. D. Mercer and R. G. Sherwood, "The Structure of Silver Films Deposited on Mica Substrates in Ultra-High Vacuum," Surface Science 6, 309 (1967).

15, Jaeger, H., P. D. Mercer and R. G. Sherwood, "Nucleation and Growth of Silver Films Deposited on Mica Substrates in Ultra-High Vacuum," Surface Science 11, 265 (1968).

16. Brenner, S. S., "Metals," The Art and Science of Growing Crystals, J. J. Gilman, ed., N. Y., John Wiley and Sons, Inc., 30 (1963).

17. Fisher, S. S., O. F. Hagena and R. G. Wilmoth, "Flux and Speed Distributions of Molecular Beams after Scattering by Metal Surfaces," J. Chem. Phys. 49, 1562 (1968).

18. Hagena, O. F., J. E. Scott, Jr., and A. K. Varma, "Design and Performance of an Aerodynamic Molecular Beam and Beam Detection System," U.Va., RLES Report AST-4038-103-67U (June 1967).

19. Hagena, O. F. and A. K. Varma, "Time-of-Flight Velocity Analysis of Atomic and Molecular Beams," Rev. Sci. Instr. 39, 47 (1968).

BIBLIOGRAPHY (Continued)

20. Bishara, M. N., "An Experimental Investigation of Intensity and Velocity Distributions of Thermal-Energy Argon Atoms Scattered by a Monocrystalline Silver Surface," U.Va., RLES Report AEEP-4038-109-69U (March 1969).

21. Bishara, M. N., S. S. Fisher, A. R. Kuhlthau, and J. E. Scott, Jr., "Measured Flux and Speed Distributions of Atmospheric Gases Scattered from Polycrystalline Copper and Aluminum Surfaces," paper presented at the Fourth International Materials Symposium, Berkeley, Calif. June 19-21, 1968.

22. Fisher, S. S., M. N. Bishara, A. R. Kuhlthau, and J. E. Scott, Jr., "Scattering of Helium and Argon Nozzle-type Molecular Beams from Lithium Fluoride Surfaces," to be published in Rarefied Gas Dynamics, N. Y., Academic Press (1968).

23. Saltsburg, H., J. N. Smith, Jr., and R. L. Palmer, "Scattering of Molecular Beams of He, D_2, and H_2 From the (111) Plane of Ag, " Rarefied Gas Dynamics, N. Y., Academic Press, supplement 4, volume I, 223 (1967).

APPENDIX 1

DETERMINATION OF THE INTENSITY, MEAN SPEED, AND SPEED SPREAD FROM THE RECORDED TIME-OF-FLIGHT DENSITY DISTRIBUTIONS

As explained in Section 3.2 of the text, the detector signal, $S_d(t)$, is a voltage-versus-time distribution, where the voltage is proportional to the mean atomic density within the detector and time is measured from the mean time for passage of the atoms through the chopper. As outlined in Section 3.4, the method for extracting the desired parameters or "moments", as they are often called, from the measured time-of-flight (TOF) distributions is based upon a curve-fitting technique. This technique constitutes a short-cut, approximate method enabling the experimenter to by-pass the totally impractical task of exactly determining these moments directly from the measured signals.

The three principal moments sought in the present study are a beam intensity (I_r), an intensity-weighted mean speed ($\langle v_r \rangle$), and an intensity-weighted mean-square thermal speed ($\langle c_r^2 \rangle$). If the TOF resolution, R, were effectively infinite (see Section 3.4), then an ideal TOF detector signal, call it $S_d^o(t)$, would be recorded. Furthermore, if the quantity $g(v)$ is defined as the actual differential intensity distribution for the measured beam, i.e.

$$g(v_r) = \frac{\partial I_r}{\partial v_r} \quad , \tag{A1.1}$$

then it follows that

$$I_r = \int_o^\infty g(v_r)\, dv_r \tag{A1.2}$$

$$\langle v_r \rangle = (I_r)^{-1} \int_o^\infty v_r\, g(v_r)\, dv_r \tag{A1.3}$$

$$\langle c_r^2 \rangle = (I_r)^{-1} \int_o^\infty (v_r - \langle v_r \rangle)^2 g(v_r)\, dv_r. \tag{A1.4}$$

It is straightforward to show (see, for example, Reference 19), that

$$S_d^o(t) = \frac{t_{so}}{K} \left(\frac{L}{t}\right) g \left(\frac{L}{t}\right) \tag{A1.5}$$

where t_{so} as used here is the time - halfwidth of the initial beam pulse as it passes through the chopper, L is the flight-path length, and K is a calibration constant depending only upon the target-detector-chopper geometry and the particular gas being detected. The three moments of interest may then be redefined in terms of $S_d^o(t)$ such that

$$I_r = \frac{K}{t_{so}} \int_o^\infty t^{-1}\, S_d^o(t)\, dt \tag{A1.6}$$

$$\langle v_r \rangle = \frac{KL}{t_{so} I_r} \int_o^\infty t^{-2} \; S_d^o(t)\, dt \qquad (A1.7)$$

$$\langle c_r^2 \rangle = \frac{K}{t_{so} I_r} \int_o^\infty t^{-1} \left(\frac{L}{t} - \langle v_r \rangle \right)^2 S_d^o(t)\, dt. \qquad (A1.8)$$

Now, if $S_d^o(t)$ and the parameters K, t_{so}, and L are known, the integrations listed above can be performed immediately on a computer with the aid of numerical summation methods. If, on the other hand, $S_d(t)$ is known but $S_d(t) \neq S_d^o(t)$ due to low TOF resolution, i.e. low R, then methods are available which (in principle) enable the determination of $S_d^o(t)$ from $S_d(t)$ by means of complex convolution-inversion techniques.

In the present case, not only is $S_d(t) \neq S_d^o(t)$, but performing the integrations in Eqs. (A1.6) - (A1.8) is simply too time-consuming to justify the effort. Instead, use has been made of the analysis outlined in Reference 17 showing that, for practical purposes, $S_d(t) = S_d^o(t)$ whenever $R \geq 5$ and, further, that $S_d(t)$ can be fitted with surprising accuracy to a function of the form

$$S_d(t) = t^{-4} \exp\left[-\beta^2 \left(1 - \frac{t_o}{t} \right)^2 \right] \qquad (A1.9)$$

where β and t_o are free constants which, for $\beta \gg 1$, reduce

to

$$\mathcal{S} \approx \frac{C_1 \langle v_r \rangle}{\langle c_r^2 \rangle^{1/2}} \qquad \text{(A1.10)}$$

and

$$t_o \approx \frac{L}{\langle v_r \rangle} \qquad \text{(A1.11)}$$

with C_1 a constant of order unity. Then, it is straightforward to carry through the integration of Eq. (A1.6) to determine I_r in terms of the quantities K/t_{so}, $\mathcal{S}$ and t_o, and also, as it happens, to integrate Eqs. (A1.7) and (A1.8) to obtain, respectively, $(\langle v_r \rangle\ t_o/L)$ and $(\langle c_r^2 \rangle\ t_o^2/L^2)$ as functions of $\mathcal{S}$ alone. It is much simpler, however, to express these parameters in terms of quantities measured directly from the recorded TOF traces. Eq. (A1.9) may be fitted to the recorded traces with respect to time at the two half-maximum points, t_1 and t_2 (see Figure 3.4.1). Then, through the use of numerical tabular methods, $\langle v_r \rangle$ and $\langle c_r^2 \rangle$ can be readily expressed in terms of t_1, t_2, and L by using Eq. (A1.9) as a basis. The tabulated results for $\langle v_r \rangle$ may subsequently be least-squares fitted to a third-order polynomial in the ratio t_2 / t_1 to within 1%, yielding, as taken from Reference 20,

$$\frac{\langle v_r \rangle t_r}{L} = 0.0465 \left(\frac{t_2}{t_1}\right)^3 - 0.2577 \left(\frac{t_2}{t_1}\right)^2$$

(cont.)

$$+ 0.8379 \left(\frac{t_2}{t_1}\right) + 0.3809 \quad . \qquad \text{(A1.12)}$$

A fourth-order polynomial for $\langle c_r^2 \rangle$ may be similarly generated, as has been done in the present computations, to obtain

$$\frac{\langle c_r^2 \rangle \, t_2^2}{L^2} = - 0.0038 \left(\frac{t_2}{t_1}\right)^4 + 0.0003 \left(\frac{t_2}{t_1}\right)^3$$

$$+ 0.2230 \left(\frac{t_2}{t_1}\right)^2 - 0.4362 \left(\frac{t_2}{t_1}\right)$$

$$+ 0.2167 \qquad \text{(A1.13)}$$

which is accurate within 1% for

$$\langle d_r^2 \rangle \; t_2^2 \; / \; L^2 > 0.023 \; .$$

In addition, the fits

$$\frac{\langle v_r^2 \rangle \; t_2^2}{L^2} = 0.1067 \left(\frac{t_2}{t_1}\right)^3 - 0.3126 \left(\frac{t_2}{t_1}\right)^2$$

$$+ 1.3263 \left(\frac{t_2}{t_1}\right) - 0.1256 \qquad \text{(A1.14)}$$

accurate to within 1% and

$$\$ = -0.00177 \left(\frac{t_1}{\Delta t}\right)^4 + 0.0496 \left(\frac{t_1}{\Delta t}\right)^3 - 0.486 \left(\frac{t_1}{\Delta t}\right)^2 + 3.66 \left(\frac{t_1}{\Delta t}\right) - 2.30 \qquad \text{(A1.15)}$$

accurate to within 8% for $\$ > 2$ and 1% for $\$ > 5$ may also be generated.

Finally, the intensity, I_r, is expressible as (see References 17 and 19)

$$I_r = \frac{K}{K_1 L} S_d (t_m) [(t_2 - t_1)/ t_{so}] \langle \hat{v}_r \rangle \qquad \text{(A1.16)}$$

where

$$\langle \hat{v}_r \rangle = \frac{1}{n_{od} X_d^2} \int_o^\infty g (v_r) \, dv_r \qquad \text{(A1.17)}$$

and

$$n_{od} X_d^2 = \int_o^\infty \frac{g(v_r)}{v_r} \, dv_r \; . \qquad \text{(A1.18)}$$

The quantity n_{od} is the density at the detector if the beam is not chopped, i.e., if the detected beam is continuous, and X_d is the target-detector separation. Thus, $\langle \hat{v}_r \rangle$ is

a density-weighted mean speed in contrast to $\langle v_r \rangle$ which is an intensity-weighted mean speed. The parameter $S_d\ (t_m)$ is the maximum detector signal amplitude and the parameter K_1 is a factor near unity which is only a weak function of the TOF resolution, R, and the shape of the speed distribution, $g(v_r)$. To the extent that $g(v_r)$ is that for a Maxwellian oven beam at temperature T [i.e., that yielded by Eq. (A1.9) for $\hat{S} = 0$, but with the term $(\hat{S}t_o)^2 = (M_g L^2 / 2kT)$, where M_g is the gas-atom mass and k is the Boltzmann gas constant], then K_1 is tabulated versus R in Figure 4 of Reference 19. Also, if $\hat{S} > 5$ in Eq. (A1.9), then K_1 is tabulated versus R in the same figure. (For this latter tabulation, the exponent "-3" was used in place of "-4" in Eq. (A1.9); nevertheless, the plotted data is almost equally applicable to either exponent, since the effect of this change in exponent is vanishingly small for $\hat{S} > 5$).

As with the other parameters, a polynomial of the form

$$\frac{\langle \hat{v}_r \rangle\ t_2}{L} = \text{function of} \left(\frac{t_2}{t_1}\right) \qquad \text{(A1.19)}$$

can be generated for use in evaluating Eq. (A1.16). Through error, this has been neglected in the present data and the intensity-weighted mean speed, $\langle v_r \rangle$, has been substituted for its density-weighted counterpart in the intensity

computations. For all of the helium data, where the fitted values of S are large, this introduces negligible error; the two mean speeds are essentially equal for helium beams. For argon, on the other hand, this error causes I_r to be from 5% to 10% too high; that is, $\langle v_r \rangle$ is from 5% to 10% greater than $\langle \hat{v}_r \rangle$ for the argon beams where the fitted values of S are of order unity or less. However, due to the fact that the computed values of I_r are normalized with respect to a set of intensities deduced by the same method for the case where $S \to 0$, the net effect of this error in the plotted data is to cause the peak normalized intensities, for which S is greatest, to be at most some 5% low for argon.

Lack of sufficient TOF resolution also has an effect on the computed values of the moments $\langle v_r \rangle$, $\langle c_r^2 \rangle$, etc. In an effort to compensate for this effect, use has been made of the analysis documented in Figure 3 of Reference 19. There, the factor $(\Delta t - \Delta t_o) / \Delta t_o$ has been plotted versus (R-1) for the two previously discussed cases of a) an oven beam and b) a beam for which $S > 5$. (In reference to that figure, note that for the present experiments the "shutter function" is essentially triangular.) In the present calculations, $\Delta t = t_2 - t_1$, as measured from the recorded TOF traces, and Δt_o is the analogous width for a perfectly resolved ($R \to \omega$) TOF signal. Using the information contained

in Figure 3, the values of t_1 and t_2 measured for a given $R(=\Delta t/t_{so})$ are adjusted, assuming symmetric broadening of the perfectly resolved signal, by increasing t_1 by half of the indicated broadening and decreasing t_2 by the same amount. The adjusted time-values are then used to compute $\langle v_r \rangle$, $\langle v_r^2 \rangle$, $\langle c_r^2 \rangle$, and ζ. These operations are all performed by computer. The two possible corrections are rather arbitrarily applied according to the criterion that all data for which $\zeta < 2.5$ be subjected to the oven beam correction while all data for which $\zeta \geq 2.5$ be treated as if $\zeta > 5$. The actual polynomial fits employed in this process are:

$$\frac{\Delta t - \Delta t_o}{\Delta t_o} = 0.225\ (R-1)^{-1.55}, \quad \zeta < 2.5$$

$$= 0.145\ (R-1)^{-1.46}, \quad \zeta \geq 2.5 \qquad \text{(A1.20)}$$

For $R > 2$, these provide excellent fits to the plots in Figure 3 of Reference 19. Since ζ is itself dependent upon this correction, an iterative scheme is employed by the computer in applying Eq. (A1.20). Convergence in ζ is normally observed by the second iteration. Final corrections to the computed intensity, I_r, are effected in a similar manner by fitting polynomials to the factor K_1 $(= \frac{R\ U_m}{U_o}$ in

Figure 4 of Reference 19) as a means of compensating for the dependence of the measured value of the signal height upon the resolution, R. The polynomials employed are:

$$
\begin{aligned}
K_1 &= -0.0675 \ln (R-1) + 0.800, && S < 2.5,\ R < 2 \\
&= -0.0282 \ln (R-1) + 0.935, && S \geq 2.5,\ R < 2 \\
&= 0.800, && S < 2.5,\ R \geq 2 \\
&= 0.935 && S \geq 2.5,\ R \geq 2 \ .
\end{aligned}
\tag{A1.21}
$$